TRACKING AND DIVERSITY FOR A MOBILE COMMUNICATIONS BASE STATION ARRAY ANTENNA

by

Xavier Carbó

B.A.Sc., Universitat Politècnica de Catalunya, 1993

THESIS SUBMITTED IN PARTIAL FULFILLMENT
OF THE REQUIREMENTS FOR THE DEGREE OF
MASTER OF APPLIED SCIENCE
in the school of Engineering Science

© Xavier Carbó 1995

SIMON FRASER UNIVERSITY

September 1995

All rights reserved. This work may not be
reproduced in whole or in part, by photocopy
or other means, without permission of the author.

APPROVAL

NAME: Xavier Carbó

DEGREE: Master of Applied Science (Engineering Science)

TITLE OF THESIS: Tracking and Diversity for a Mobile Communications Base Station Array Antenna

EXAMINING COMMITTEE:

Chairman:

Dr. Jacques Vaisey
Assistant Professor
School of Engineering Science, SFU

Senior Supervisor:

Dr. Shawn P. Stapleton
Associate Professor
School of Engineering Science, SFU

Senior Supervisor:

Dr. Steve Hardy
Professor
School of Engineering Science, SFU

Supervisor:

Dr. M. Parameswaran
Associate Professor
School of Engineering Science, SFU

Examiner:

Dr. J.K. Cavers
Professor
School of Engineering Science, SFU

DATE APPROVED: Oct. 1/95

PARTIAL COPYRIGHT LICENSE

I hereby grant to Simon Fraser University the right to lend my thesis, project or extended essay (the title of which is shown below) to users of the Simon Fraser University Library, and to make partial or single copies only for such users or in response to a request from the library of any other university, or other educational institution, on its own behalf or for one of its usrs. I further agree that permission for multiple copying of this work for scholarly purposes may be granted by me or the Dean of Graduate Studies. It is understood that copying or publication of this work for financial gain shall not be allowed without my written permission.

Title of Thesis/Project/Extended Essay

"Tracking and Diversity for A Mobile Communications Base Station Array Antenna"

Author:

(signature)

Xavier Carbo
(name)

September 18, 1995
(date)

ABSTRACT

A theoretical model is developed for simulating fast Rayleigh fading while maintaining the two dimensional coordinates of the mobile transmitter relative to the base station. Analytical expressions are derived and simulation results presented.

The model is slightly modified for use in conjunction with a base station array antenna. Since the signals received by neighboring antenna elements are expected to be strongly correlated, directional beams can be formed by introducing a linear phase shift across the array front. The benefits of utilizing such a configuration are decreased transmitter power, reduced co-channel interference and, as a consequence, higher system capacity. One system requirement is that the vehicle must be tracked as it traverses the cell. An algorithm is developed that performs the tracking based on differential beams.

Next, angle diversity is investigated. By altering the linear phase shift of the array the directional beam illuminates the scatterers surrounding the mobile asymmetrically, providing a unique form of angle diversity. It is shown that the percentage of time that the envelope is below a certain level can significantly be reduced by appropriately combining the diversity signals, thereby improving the BER (Bit Error Rate). Similar results are also demonstrated for a digital communications system using QDPSK (Quadrature Differential Phase Shift Keying) modulation.

Finally, field tests were performed and algorithms tested on the data collected from the real environment. The tracking performance proves to be very accurate and the diversity results agree quite closely with those predicted by the model.

ACKNOWLEDGEMENTS

I would like to thank Dr. Shawn Stapleton for his guidance and support throughout this thesis. His assistance and generosity over the past few years has helped me in many ways.

Thanks also to Sirooj Rambaran, Trent Mckeen and Sarkis Tegharárian for making the successful completion of the project possible. Working with them was not only an invaluable experience but also a very pleasant one.

I would like to extend my gratitude to Dr. Jim Cavers for giving me the opportunity to be a part of the RF/Communications group at SFU.

And finally, a very special and well deserved thank you to Maureen for her unconditional support and much appreciated encouragement.

TABLE OF CONTENTS

LIST OF TABLES

LIST OF FIGURES

LIST OF SYMBOLS

f_c	carrier frequency
N	number of scatterers
β	wave number
V	velocity of the mobile
$\tilde{a}_i$	ith path transmission attenuation
α	direction of travel
θ_i	angular position of the ith scatterer
f_d	doppler frequency
AF	array factor
ψ	generalized angle
HP	half power beamwidth
BWFN	beamwidth between first nulls
w_n	set of complex weights
r	radius of scatterers
$\vec{p}_o$	initial position of the car
$\vec{p}$	position of the car
$\vec{p}_{iro}$	initial position of the ith scatterer
$\vec{p}_{ir}$	position of the ith scatterer
$\lvert\rho_i\rvert$	modulus of the reflection coefficient of the ith scatterer
ϕ_i	phase of the reflection coefficient of the ith scatterer
Δ	delay spread
$\dot{\theta}$	angular velocity of the scatterers
β_i	angle from boresight
$\Delta\beta$	tracking beams offset
θ	diversity beam offset
D	distance between mobile and base station

Γ_1	signal to noise ratio of branch 1
Γ_2	signal to noise ratio of branch 2
γ	signal to noise ratio of the combined signal
ρ	correlation coefficient
P_1	signal power of branch 1
P_2	signal power of branch 2

1. INTRODUCTION

The rapid growth and popularity of mobile telephone services has been hampered by the insufficient number of frequencies allocated for that purpose. The challenge for the industry is to achieve a higher user capacity with more reliable communications while making use of the resources and infrastructure currently available. Many new system approaches are being sought as companies worldwide compete to devise and commercialize an efficient technology for this potentially immense market.

Phased array base station antennas have been proposed by several authors as a means of achieving higher spectral efficiency. Dr. Shawn Stapleton has developed a new system architecture whereby each antenna element is capable of simultaneously transmitting or receiving at any given channel, as baseband processing replaces the need for RF tuning diodes to implement the weights. The antenna array combines the received signals to enhance reception from a particular direction or alternatively to better focus transmission. See [1] for a more detailed description of his proposed system. The benefits of a directive beam at the base station are widely known and have been extensively documented in the past [2,3]. However, the technology has not been utilized at large because of the extensive costs and complexity of such a system. The increase in speed and sophistication, as well as the decrease in cost, of the new generation of DSP processors has made the idea of a base station array antenna, with all the processing done at baseband, an attractive alternative. Some of the main advantages include greater efficiency in radiated power, a reduction of signal degradation introduced by cochannel interference, in both forward and reverse channels, as well as flexibility to adjust the beamwidth depending on traffic volume.

This thesis work will focus on the reverse channel, that is, the instance where the transmission originates at the mobile unit. In particular, the potential tracking capability of the antenna array will be investigated, so that continuously updated information

regarding the location of the mobile unit can be sent to the base station making it possible to steer a beam towards it. As well, angular diversity will be used in order to reduce the deep fades in the received signal. Diversity combining techniques prove to be a very effective way to combat fading in a mobile communications environment. These techniques are based on the assumption that two uncorrelated multipath signals are unlikely to simultaneously experience a deep fade. The question is: how to procure a diversity signal? The solution presented in this thesis is to operate the antenna in a dual beam configuration so as to differentiate the angular components of the received signal. A model for a spatial channel simulator will be developed in order to assess the capability of the antenna array to track a mobile unit and provide angle diversity. This new model is based on Jakes' widely accepted assumption of a ring of scatterers surrounding the transmitter [2]. The additions to the model accommodate the introduction of the antenna array and allow it to be used for long term analyses.

The thesis is organized into five distinct chapters. Chapter 2 provides some theoretical insight into the mobile radio communication medium, array theory and background on $\frac{\pi}{4}$ – QDPSK (Quaternary Differential Phase Shift Keying) modulation.

Chapter 3 focuses on the development of the model and provides the verification that it operates according to theory. The spatial channel simulator model in itself is a very significant part of the thesis as it provides a major advantage. The proposed systems can be extensively tested through simulation in a laboratory which saves researchers from having to perform the costly and time consuming field tests otherwise necessary to obtain the measurements. As well, repeatability of the tests is ensured.

In Chapter 4 this model is used to investigate the various performance capabilities of the antenna array. The first part of the chapter considers the issue of tracking the mobile unit. Two beams are used to monitor the location of the vehicle; one monitors the right of the current position, the other the left. The strength of the signal received from the two beams identifies if the mobile is moving to the left or to the right. This way the new position can be retrieved and updated periodically. The second part of the chapter

focuses on the method of achieving angle diversity. By altering the linear phase shift of the array, the directional beams illuminate the scatterers surrounding the mobile asymmetrically, providing a unique form of diversity. An unmodulated carrier is used as the transmitted signal in both cases as it allows the use of a very low sampling frequency. The final section of Chapter 4 describes the simulation of a digital system that employs QDPSK. The adoption of this signaling scheme has gained popularity recently because a much narrower bandwidth can be achieved than with digital FM. It serves the purpose of mapping an improvement in quality of the fading envelope to a reduction in the bit error rate (BER). The results show that, in addition to being able to successfully track the mobile, the throughput of the system can be significantly increased through the use of angle diversity.

Chapter 5 documents the field trials that were conducted in order to assess the performance of the phased array antenna. This was a very important part of the thesis because by comparing the results predicted by the theoretical model to those of the actual field measurements, the robustness of the simulator could be confirmed. It was also crucial that the performance of the antenna array system be determined in a real urban mobile environment rather than solely in theory.

Chapter 6 presents several conclusions that can be drawn from this thesis work. First, the developed spatial channel simulator proves to be robust and can be used to effectively recreate the conditions encountered in the real mobile environment. Second, the array antenna was able to track the mobile unit and retrieve its angular position within an error of ± 0.5 degrees. Third, through the use of angle diversity, a significant reduction in the BER of the QDPSK system under study was attained.

2. THEORETICAL BACKGROUND

This section contains a review of some of the most relevant principles of mobile communications, as well as an introduction to linear array theory. A particularly useful modulation scheme for use in a mobile environment is also presented.

2.1 Mobile-Radio Communication Medium

The mobile radio channel is characterized, in general, by the absence of a direct line of sight between the mobile user and the base station. Multiple propagation paths arise from buildings, structures and other mobile scattering objects surrounding the mobile unit. Consequently, the received signals are formed by the vectorial addition of numerous reflected waves that form a standing wave pattern with nulls occurring at half-wavelengths of the carrier frequency. This phenomenon is known as multipath fading. Furthermore, the signals arrive at the receiver with relative time delays depending on the difference in propagation path lengths. In digital communication systems, intersymbol interference is introduced if the transmission rate is sufficiently high. This is a particular case known as frequency selective fading.

Path loss and terrestrial propagation effects such as diffraction and terrain attenuation tend to cause long term variations of the received signal strength leading to what is known as long-term fading. This thesis focuses on the short-term or multipath fading, since it imposes the most severe limitations on the quality of radio transmissions.

2.1.1 Received Signal Characteristics. Rayleigh Fading Model

The short term fading model assumes that the mobile unit is receiving a narrowband signal, $s_o(t)$, at a carrier frequency, ϖ_c, in a uniformly scattered area, as shown in Figure 2.1. Under these assumptions, the fading process presents a flat response

over the signal bandwidth and can be modeled as a multiplicative process.

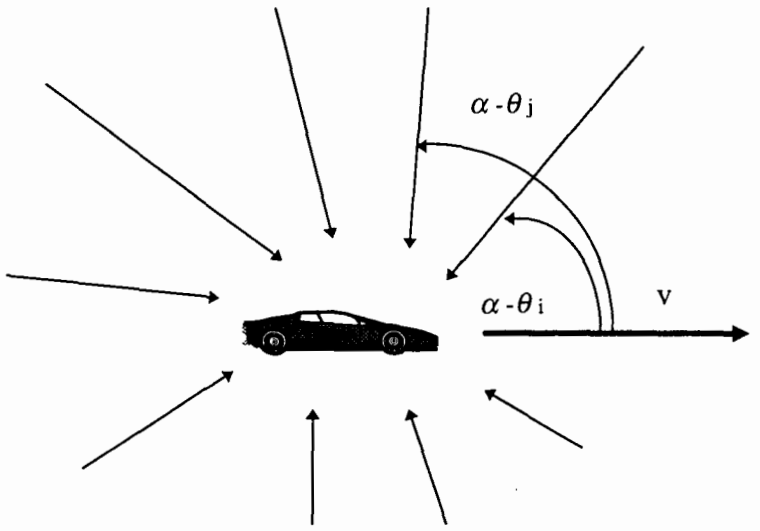

Figure 2.1 Short-Term Fading Model

Complex notation will be used hereafter to represent all the signals involved, since it is easier to manipulate than its equivalent trigonometric form. The transmitted signal can be written as:

$$s_c(t) = a_o(t)\, e^{j(\varpi_c t + \phi_o(t))} \quad ; \quad s_o(t) = a_o(t)\, e^{j\phi_o(t)} \tag{2.1}$$

Assuming there are N scatterers surrounding the vehicle, the received signal, $s_r(t)$ is composed of the sum of all N reflected waves:

$$\begin{aligned} s_r(t) &= \sum_{i=1}^{N} a_o(t)\, \tilde{a}_i e^{j(\varpi_c t + \phi_o(t) - \beta\, vt\cos(\theta_i - \alpha))} \\ &= s_c(t) \sum_{i=1}^{N} \tilde{a}_i e^{-j\,\beta\, vt\cos(\theta_i - \alpha)} = s_c(t)\, s(t) \end{aligned} \tag{2.2}$$

where

$\tilde{a}_i$ is a complex variable that represents the ith path transmission attenuation factor.

β is the wave number.

v is the velocity of the vehicle.

θ_i is the angular position of the ith scatterer.

α is the direction of travel.

$\beta\, v t \cos(\theta_i - \alpha)$ is the contribution of the ith scatterer to the Doppler effect.

$\frac{\beta\, v}{2\pi}\cos(\theta_i - \alpha)$ is the Doppler frequency.

$f_d = \frac{\beta\, v}{2\pi} = \frac{v}{\lambda}$ is the maximum Doppler frequency, typically between 0 and 100 Hz.

Figure 2.2 illustrates a typical fading signal received while the mobile unit is in motion.

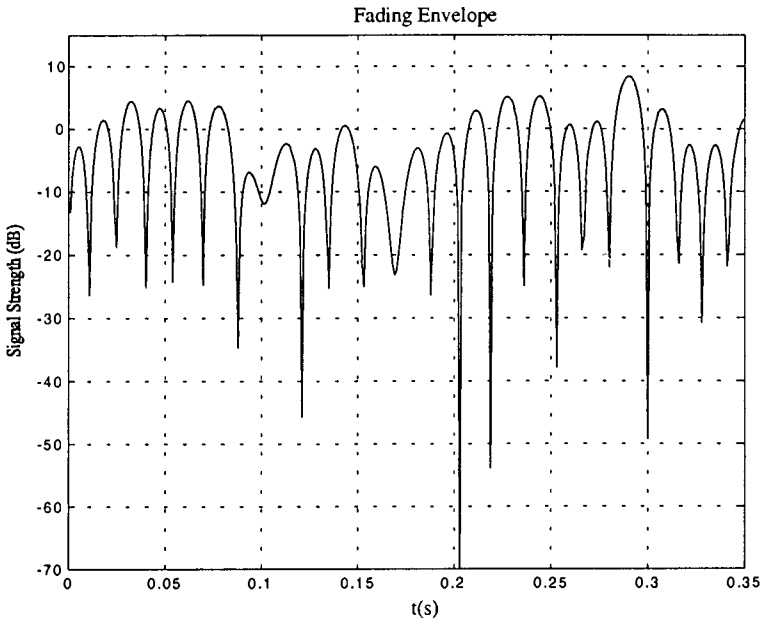

Figure 2.2 Typical Fading Envelope

Equation (2.2) can be further developed by separating its real and complex parts. Let

$$\tilde{a}_i = R_i + j\,S_i \tag{2.3}$$

then the multiplicative fading process component, s(t), can be written as:

$$\begin{aligned} s(t) &= \sum_{i=1}^{N} (R_i + j\cdot S_i)\,(\cos(\xi_i(t)) - j\cdot \sin(\xi_i(t))) \\ &= \sum_{i=1}^{N} (R_i \cos(\xi_i(t)) + S_i \sin(\xi_i(t))) - j\cdot(\sum_{i=1}^{N} (R_i \sin(\xi_i(t)) - S_i \cos(\xi_i(t)))) \\ &= X(t) + j\cdot Y(t) \end{aligned} \tag{2.4}$$

where

$$\xi_i(t) = \beta\, vt \cos(\theta_i - \alpha)$$

$$X(t) = \sum_{i=1}^{N} (R_i \cos(\xi_i(t)) + S_i \sin(\xi_i(t))) \tag{2.5}$$

$$Y(t) = -(\sum_{i=1}^{N} (R_i \sin(\xi_i(t)) - S_i \cos(\xi_i(t))))$$

From the central limit theorem it follows that, for large values of N, X and Y are Gaussian distributed, independent random variables. The received signal, s(t), can be written in an alternate form as:

$$s(t) = r(t)\, e^{j\psi(t)} \quad ; \quad r(t) = \sqrt{X^2(t) + Y^2(t)} \quad ; \quad \psi(t) = \tan^{-1}(\frac{Y(t)}{X(t)}) \tag{2.6}$$

The joint distribution of r and ψ can be found to be [3]:

$$p_{r\psi}(r,\psi) = \frac{r}{2\pi\sigma^2} e^{-\frac{r^2}{2\sigma^2}} \tag{2.7}$$

Therefore

$$p_r(r) = \frac{r}{\sigma^2} e^{-\frac{r^2}{2\sigma^2}} \quad ; \quad 0 \le r \le \infty \quad ; \quad p_\psi(\psi) = \frac{1}{2\pi} \quad ; \quad 0 \le \psi \le 2\pi \tag{2.8}$$

Equation (2.8) summarizes the two most important statistical aspects of the short-term fast fading: its phase is uniformly distributed and its envelope follows a Rayleigh distribution. On that account, it is also known as Rayleigh fading. The cumulative probability distribution (CPD) of the envelope can easily be derived by integrating the probability density function (PDF), $p_r(r)$:

$$P_r(r) = \int_0^r p_r(r)\, dr = 1 - e^{-\frac{r^2}{2\sigma^2}} \quad ; \quad 0 \le r \le \infty \tag{2.9}$$

Figure 2.3 illustrates both the PDF and the CPD of the fading envelope.

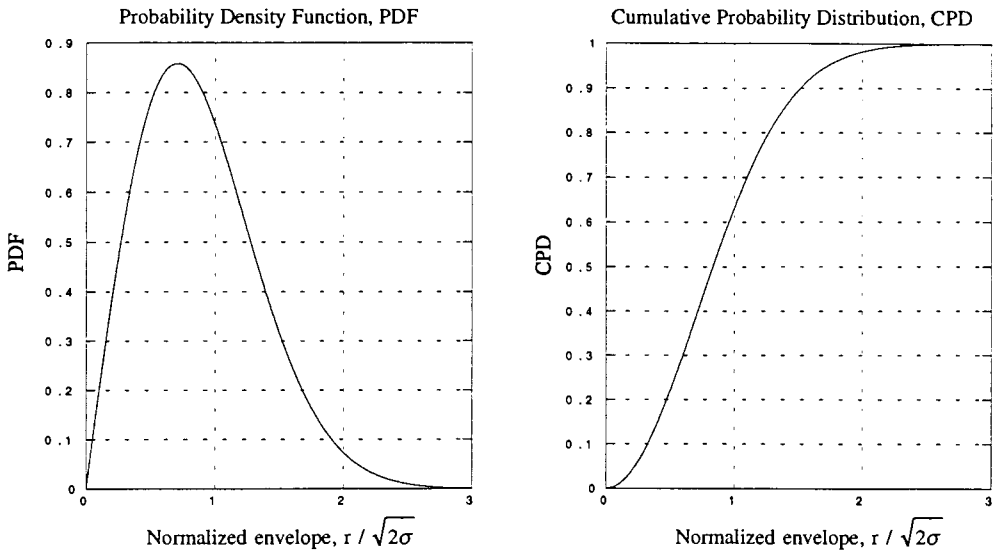

Figure 2.3 PDF and CPD of the Fading Envelope

2.1.2 Power Spectral Density of the Fading Signal

Once again, the angle of arrival of the incident waves is assumed to be uniformly distributed between 0 and 2π. In this case, the power contributed to the received signal by waves arriving within the differential angle, $d\theta$, is equal to the amount of power arriving in that particular angular interval that would be received by an isotropic antenna [3]

$$S(\theta)\, d\theta = G \cdot p(\theta) d\theta \tag{2.10}$$

where G is the gain of the receiving antenna, and $S(\theta)$ is related to S(f) by:

$$S(f) = S(\theta)\left|\frac{d\theta}{df}\right| \tag{2.11}$$

From Equation (2.2):

$$f = f_c + f_d \cos(\theta) \tag{2.12}$$

and, developing the above expressions:

$$\frac{d\theta}{df} = -\frac{1}{f_d\sqrt{1-\left(\frac{f-f_c}{f_d}\right)^2}} \tag{2.13}$$

$$S(f) = \frac{G}{2\pi\sqrt{f_d^2 - (f - f_c)^2}} \tag{2.14}$$

Figure 2.4 illustrates the above result for an omnidirectional antenna with no gain, G=1, and a maximum Doppler frequency of 37 Hz, which would result from a traveling speed of 50 Km/h and a carrier frequency of 815 MHz.

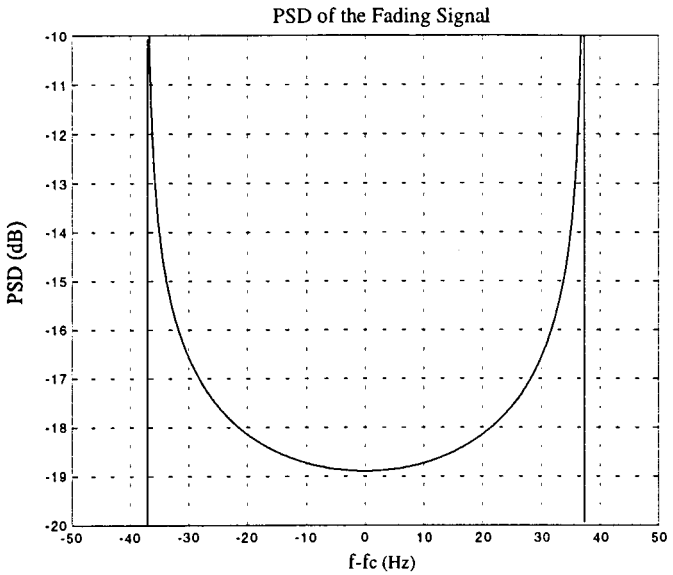

Figure 2.4 Power Spectral Density of the Fading Process

2.1.3 Reverse Channel

The results obtained in previous sections assumed the mobile to be operating as the receiver. Although still applicable here, the situation is slightly modified for the case in which the transmission originates at the mobile. Since the transmission medium is linear, one would expect that the reciprocity theorem would hold, thus replicating the exact same conditions. However, in a scattering environment there are some fundamental differences between the geographical locations in which the mobile units and the base stations operate. While the mobile units will be at ground level, close to the scattering objects and immersed in a rapidly changing environment, the base station is more likely

to be located at some high elevation, either on a nearby hill or at the top of a high-rise, with an unobstructed line of sight with its area of coverage.

The main difference between the two cases lies in the envelope correlation based on space separation. In the previous case, with the mobile acting as a receiver, small changes in its position have a significant effect on the phase with which the individual waves add up to form the combined signal. Distances of the order of half a wavelength are typically enough to provide fairly uncorrelated signals [2]. On the other hand, signals transmitted by a mobile unit arrive at the base station within a very narrow angular sector, commonly anywhere from 0.1° to 5°. Changes in the position of the base station antenna are less likely to decorrelate the signals. In fact, it has been empirically shown that in order to obtain correlation coefficients of the order of less than 0.7, separations of more than ten times the wavelength are needed [4].

A mathematical model that describes the reverse channel is outlined in [4]. The scatterers are assumed to be located in a circle around the transmitting mobile unit, with no scatterers present in the base station surroundings, as seen in Figure 2.5.

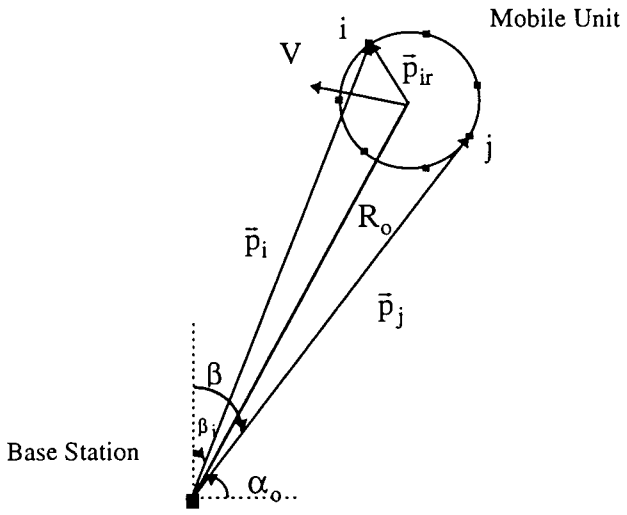

Figure 2.5 Scattering Model for the Reverse Channel

With a few additional assumptions, the model can be used to evaluate the spatial correlation of signals received at the base station, as well as their power spectral density. However, one important limitation of this model is that the observation time during which the model can be applied is small. A modification that overcomes this limitation will be discussed in Chapter 3.

2.2 Array Theory

For many radio communications applications it is desirable to have a directional radiation pattern that focuses the energy in a particular direction. In general, directivity is a function of both the frequency and the size of the antenna, with larger antennas achieving higher directivities. In these cases, one interesting alternative to the use of oversized, bulky antennas is to arrange several smaller antennas in such a manner that their interconnection results in a directional overall pattern. Such a configuration is known as an array antenna. Although arrays have been studied and very well documented since the early days of radio electronics, their application has been restricted to radar, military use and, most recently, satellite communications. Their apparent functional simplicity contrasts with the high cost involved in providing accurate processing and control at the RF stages. Recent developments in DSP technology suggest the possibility of implementing a cost effective system that uses an antenna array, with all the processing performed at baseband. Arrays can be of many types, depending on the geometrical disposition of their elements and a complete overview is beyond the purpose of this study. The focus will be on one-dimensional arrays, particularly linear arrays.

2.2.1 Linear Arrays

A typical configuration for a linear array is shown in Figure 2.6, where the antenna is assumed to be operating in reception. The array elements lie along a straight line, their outputs are weighted and summed to form the received signal. It will then be input to the receiver if the weight is generated at RF, or simply to the demodulator when operating at baseband. As shown, there is a relative phase shift between elements, due to the difference in paths traveled by the arriving wave, that depends on both the angle of arrival and the separation between elements. When each of the antennas is omnidirectional the resulting pattern is known as the array factor, AF.

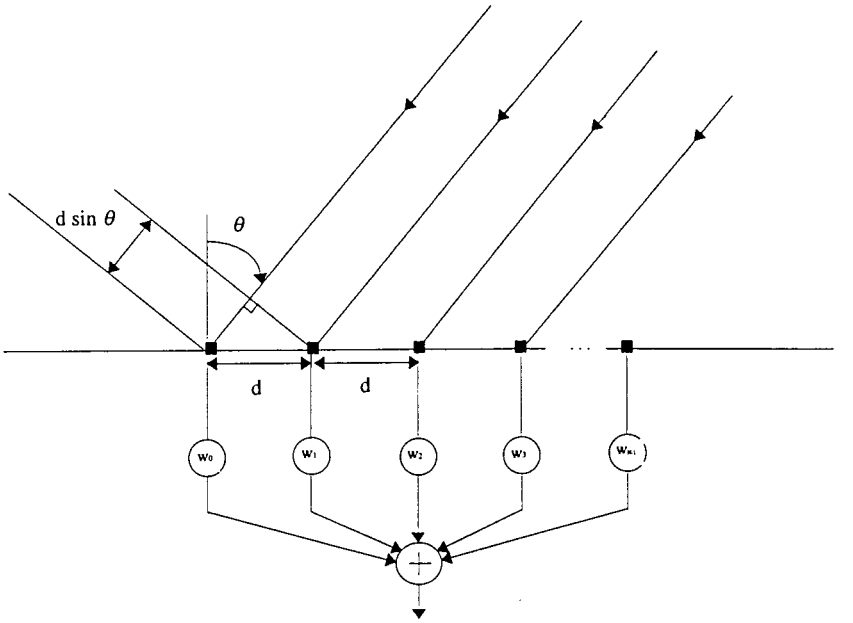

Figure 2.6 Linear Array of Isotropic Sources

The array factor can be calculated as:

$$AF = w_o + w_1 e^{j\beta d_1 \sin\theta} + w_2 e^{j\beta d_2 \sin\theta} + \ldots + w_{N-1} e^{j\beta d_{N-1} \sin\theta}$$
$$= \sum_{n=0}^{N-1} w_n e^{j\beta d_n \sin\theta} \qquad (2.15)$$

By letting:

$$w_n = |w_n| e^{j\alpha_n} \qquad (2.16)$$

Equation (2.15) becomes :

$$AF = \sum_{n=o}^{N-1} |w_n| e^{j(\beta d_n \sin\theta + \alpha_n)} \qquad (2.17)$$

A very convenient case is that of equally spaced arrays. In that case $d_n = n \cdot d$. Furthermore, if the weights have a linear phase progression: $\alpha_n = n \cdot \alpha$ and are equal in modulus, $|w_n| = 1$, a compact expression can be found for equation (2.17). By introducing the generalized angle

$$\psi = \beta d \sin\theta + \alpha \qquad (2.18)$$

equation (2.17) can be written as:

$$AF = \sum_{n=o}^{N-1} e^{j\,n\psi} = \frac{1-e^{jN\psi}}{1-e^{j\psi}} = \frac{e^{j\frac{N\psi}{2}}(e^{-j\frac{N\psi}{2}} - e^{j\frac{N\psi}{2}})}{e^{j\frac{\psi}{2}}(e^{-j\frac{\psi}{2}} - e^{j\frac{\psi}{2}})} = e^{j\frac{\psi}{2}(N-1)}\,\frac{\sin(\frac{N\psi}{2})}{\sin(\frac{\psi}{2})} \tag{2.19}$$

The normalized array factor for a maximum value of unity is then defined as:

$$|f(\psi)| = \frac{1}{N}\left|\frac{\sin(\frac{N\psi}{2})}{\sin(\frac{\psi}{2})}\right| \tag{2.20}$$

Figure 2.7 is a plot of Equation (2.20) for a seven element antenna array with equal weights defined by $\alpha = 0$, $w_n = 1$ and spacing between elements of $d = \lambda / 2$.

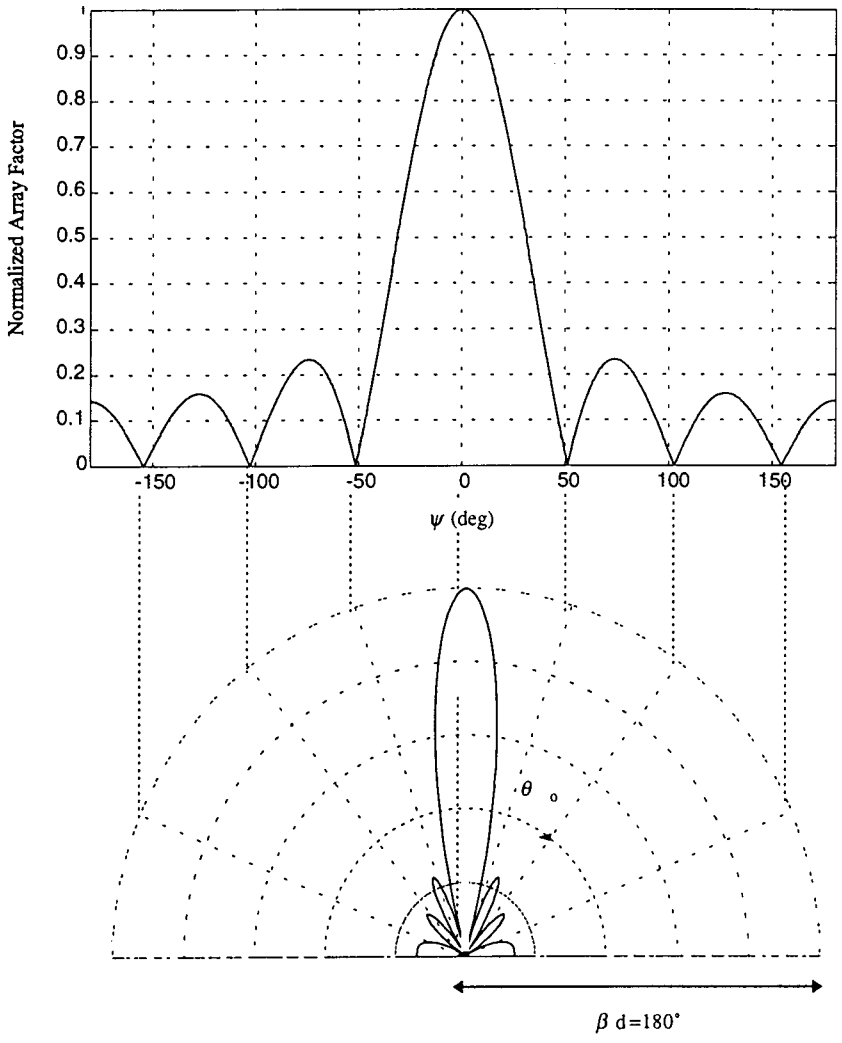

Figure 2.7 Schelkunoff's Graphical Technique

The lower part of the figure illustrates Schelkunoff procedure [5] for finding the array factor as a function of the real angle θ and the progressive phase shift α, given $|f(\psi)|$. In this case, since $0 \le \theta \le 2\pi$, $\psi = \pi \sin\theta \Rightarrow -\pi \le \psi \le \pi$, one whole period of the array factor is mapped to its polar representation.

2.2.2 Phased Arrays

The main beam maximum direction of an array can be controlled by the relative phase α. It can be written as

$$\alpha = -\beta \, d \sin(\theta_0) \tag{2.21}$$

where θ_0 is the direction for which the array factor is maximum. This feature has made antenna arrays particularly interesting for radar and tracking applications, since the beam can be electronically scanned at a very high speed. When α=0, as in Figure 2.7, the beam is said to be pointing at boresight. Similarly, the pattern shape could be altered by adequately choosing the set of weights and the addition of a linear phase shift would still provide scanning capabilities. For simplicity, equal weights were used in this study, where only one parameter, the phase shift α, is needed to fully characterize the state of the array. Figure 2.8 depicts the process of transforming the array factor as a function of the generalized angle ψ into the real pattern for a phase shift of -30°.

As the beam is scanned away from boresight the main beam tends to broaden. The half power beamwidth, HP, for the antenna array under study (seven elements, $d = \lambda / 2$) can be calculated as:

$$|f(\psi_{HP})| = \frac{1}{7}\left|\frac{\sin(\frac{7\psi_{HP}}{2})}{\sin(\frac{\psi_{HP}}{2})}\right| = \frac{1}{\sqrt{2}} \quad \Rightarrow \quad \psi_{HP} = 0.4011357 \tag{2.22}$$

$$HP = \left| \sin^{-1}\left(\frac{0.4011357}{\pi} + \sin\theta_0\right) - \sin^{-1}\left(\frac{-0.4011357}{\pi} + \sin\theta_0\right) \right| \tag{2.23}$$

HP = 14.67° at boresight.

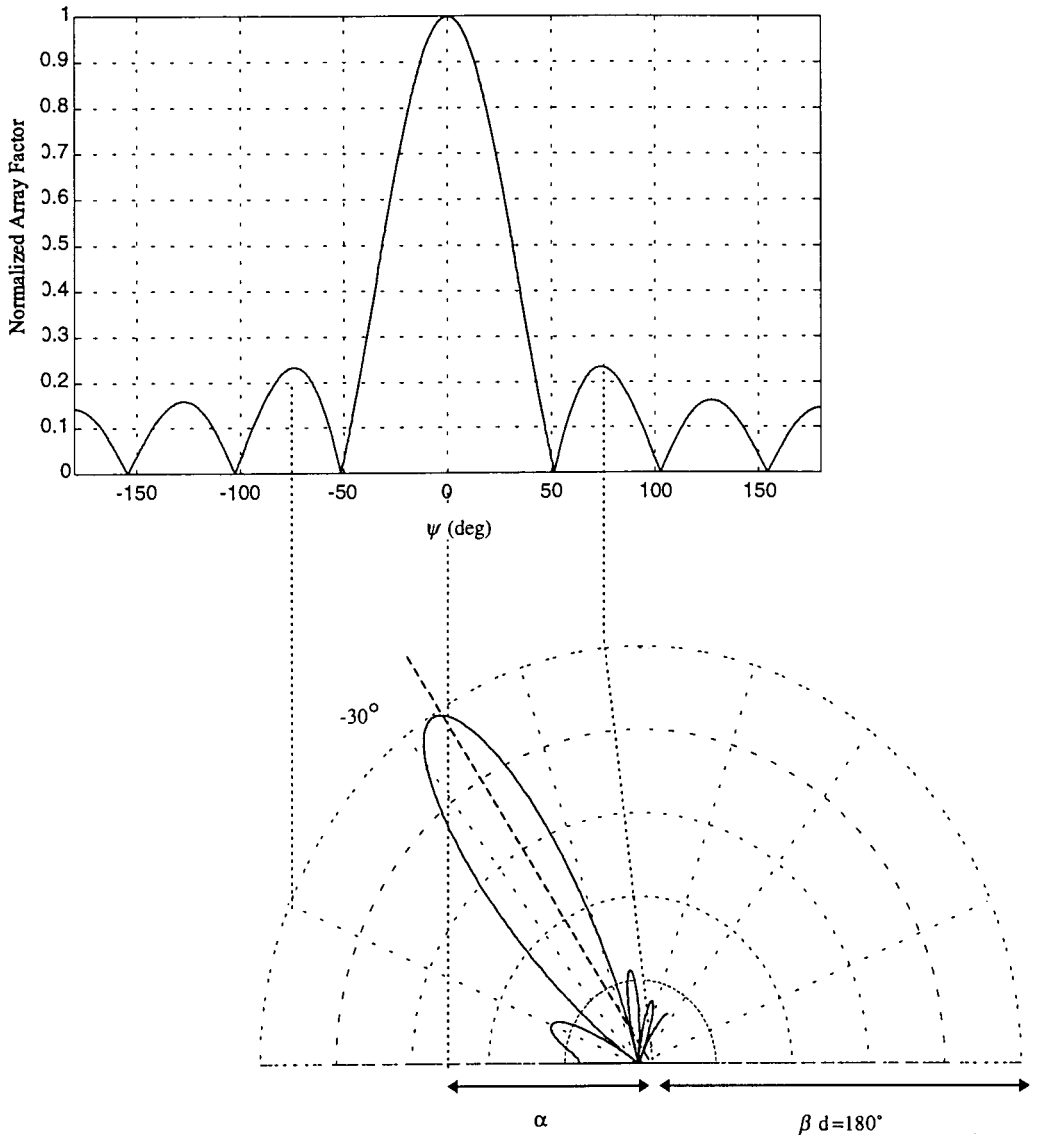

Figure 2.8 Schelkunoff's Graphical Technique

Equation (2.23) is plotted for the range of interest, that is $|\theta| \leq 30°$, in Figure 2.9. If desired, another measure of the beamwidth can be computed as the beamwidth between first nulls:

$$\text{BWFN} = \left|\theta_{\text{FN left}} - \theta_{\text{FN right}}\right| = \left| \sin^{-1}\left(\frac{2}{7} + \sin\theta_0\right) - \sin^{-1}\left(\frac{-2}{7} + \sin\theta_0\right) \right| \qquad (2.24)$$

BWFN turns out to be around 33° at boresight.

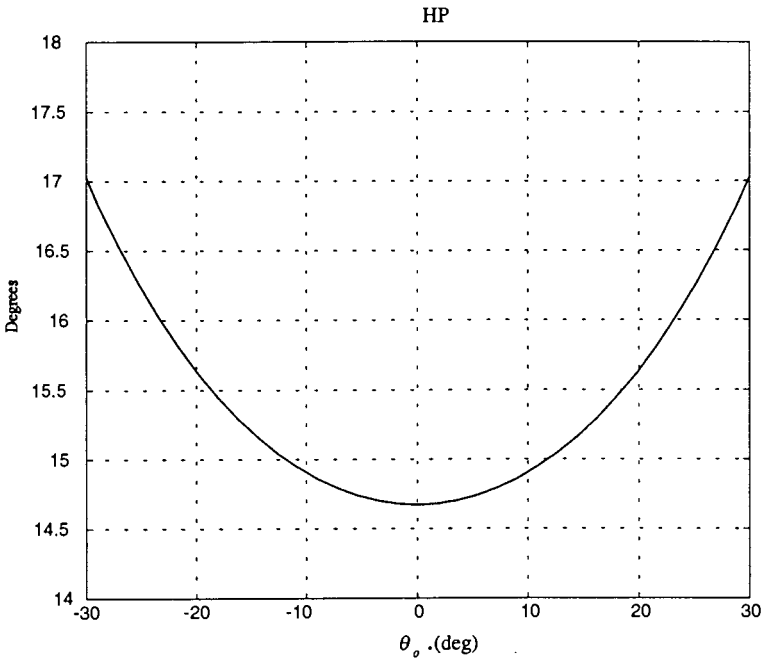

Figure 2.9 Half Power Beamwidth vs. θ_o

The directivity of the array defines its ability to concentrate energy in a particular direction. It can be calculated as:

$$D = \frac{4\pi}{\Omega_A} \quad ; \text{ where } \quad \Omega_A = \iint |f(\theta)|^2 \, d\Omega \tag{2.25}$$

The array factor can be written in an alternative form that makes its integration much easier to perform:

$$\begin{aligned} |f(\psi)|^2 &= \left| \frac{\sin(N\psi/2)}{N\sin(\psi/2)} \right|^2 \\ &= \frac{1}{N} + \frac{2}{N^2} \sum_{m=1}^{N-1} (N-m)\cos(m\psi) \end{aligned} \tag{2.26}$$

After several calculations [5] the directivity can be found to be

$$D = \frac{1}{\frac{1}{N} + \frac{2}{N^2} \sum_{m=1}^{N-1} \frac{N-m}{m\beta d} \sin(m\beta d)\cos(m\alpha)} \tag{2.27}$$

In this case, since the spacing is a multiple of half the wavelength, the directivity is equal to 8.45 dB, constant and independent of the scanning phase.

2.3 $\frac{\pi}{4}$-QDPSK Modulation Scheme

In general, the task of obtaining an accurate estimate of the channel phase is not a trivial one. In mobile radio channels this difficulty is magnified due to the presence of Rayleigh fading. On channels for which the fading is sufficiently rapid to make the estimation of a stable phase reference impossible, differential techniques are alternative signaling methods that can be used, since they require phase stability over only two consecutive signaling intervals.

In a $\frac{\pi}{4}$-QDPSK system, the transmitted signal is:

$$s(t) = A\left[\sum_k u_k p(t - k/r)\right]\cos(\varpi_c t) - A\left[\sum_k v_k p(t - k/r)\right]\sin(\varpi_c t) \qquad (2.28)$$

where:

A : constant

$f_c = \frac{\varpi_c}{2\pi}$: carrier frequency

$r = \frac{1}{T}$: baud rate

p(t) : square root raised cosine pulse

u_k : k^{th} transmitted symbol in the I channel

v_k : k^{th} transmitted symbol in the Q channel

and the complex baseband signal is:

$$w(t) = A\left[\sum_k w_k p(t - k/r)\right] \;;\; w_k = u_k + j\,v_k \qquad (2.29)$$

The transmitted symbol w_k is obtained from the data symbol through the differential encoding rule:

$$w_k = w_{k-1}\, s_k \qquad (2.30)$$

With a $\frac{\pi}{4}$ phase offset, the symbols s_k are chosen from the set shown in Figure 2.10 a), where the input bit pattern is explicitly shown.

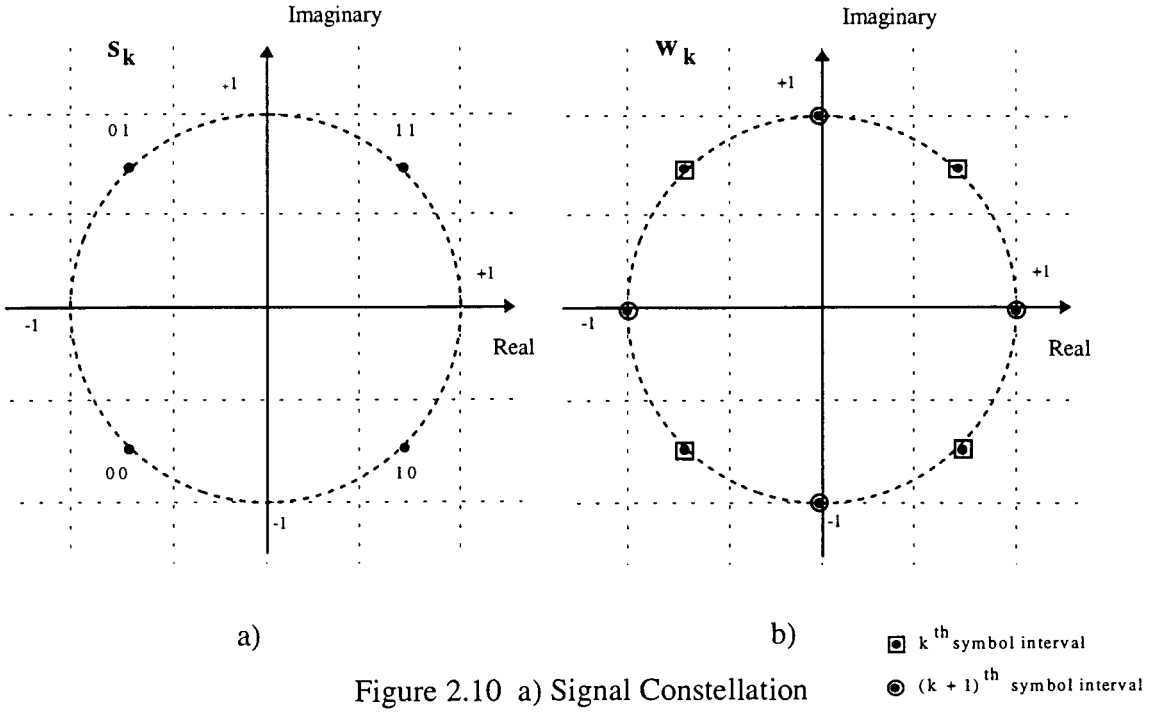

Figure 2.10 a) Signal Constellation
b) Encoded Constellation

$\pi/4$ is generally preferred versus zero shift QDPSK for timing recovery purposes. With this choice of parameters the constellation for the transmitted symbols, w_k, is divided into two subsets that are used in alternating symbol intervals, as seen in Figure 2.10 b).

The block diagram of the receiver is shown in Figure 2.11. The received signal r(t) is fed to a quadrature demodulator (QUAD DEMOD) which splits it into its in-phase and in-quadrature components. The two signals are passed through a matched filter, in this case identical to the transmitter filter p(t), and its output is sampled every T seconds. At the kth signaling interval this processing yields, in complex baseband form:

$$r_k = A\alpha_{Ik}u_k + n_{Ik} + j\left(A\alpha_{Qk}v_k + n_{Qk}\right) = A\tilde{\alpha}_k e^{j(\theta_k - \phi)} + \tilde{n}_k \qquad (2.31)$$

where $\tilde{\alpha}_k = \alpha_{Ik} + j\alpha_{Qk}$ is the contribution of the fading process, and $\tilde{n}_k = n_{Ik} + j\,n_{Qk}$ represents additive white Gaussian noise (AWGN).

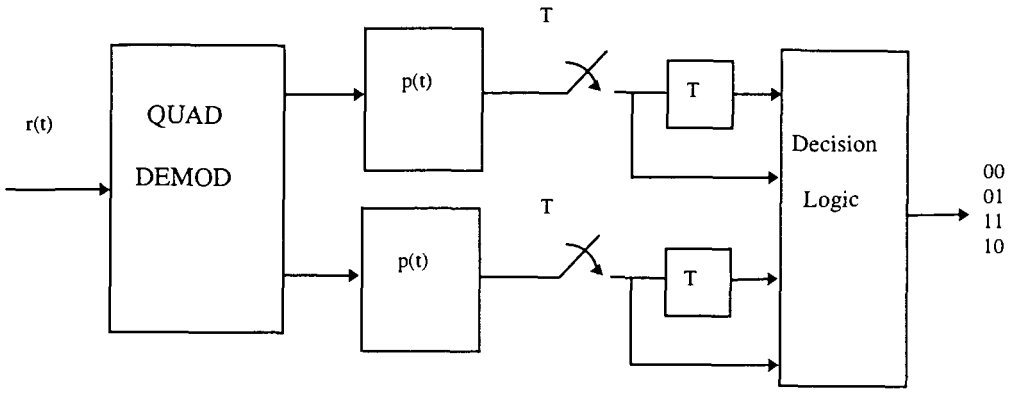

Figure 2.11 Receiver Block Diagram

Similarly, for the previous interval:

$$\begin{aligned} r_{k-1} &= A\alpha_{Ik-1}u_{k-1} + n_{Ik-1} + j\left(A\alpha_{Qk-1}v_{k-1} + n_{Qk-1}\right) \\ &= A\tilde{\alpha}_{k-1}e^{j(\theta_{k-1}-\phi)} + \tilde{n}_{k-1} \end{aligned} \tag{2.32}$$

The decision variable is computed as the phase of

$$\begin{aligned} d_k = r_k r^*_{k-1} = A^2\tilde{\alpha}_k\tilde{\alpha}^*_{k-1}e^{j(\theta_k-\theta_{k-1})} + A\tilde{\alpha}_k\tilde{n}^*_{k-1}e^{j(\theta_k-\phi)} \\ + A\tilde{\alpha}^*_{k-1}\tilde{n}_k e^{-j(\theta_{k-1}-\phi)} + \tilde{n}_k\tilde{n}^*_{k-1} \end{aligned} \tag{2.33}$$

which in the absence of fading and noise is $\theta_k - \theta_{k-1}$. From equation (2.30):

$$\theta_k = \theta_{k-1} + \theta_{newsymbol} \tag{2.34}$$

Thus, the phase recovered is that of the new transmitted symbol. Equation (2.33) can be used to calculate the theoretical probability of error as a function of the signal to noise ratio (SNR) for a system operating in an AWGN channel. The derivation is quite tedious and can be found in detail in [6,7]. The expression for the BER is:

$$P_b = Q(a,b) - \frac{1}{2}I_o(ab)\,e^{-\frac{1}{2}(a^2+b^2)} \tag{2.35}$$

with a and b defined as

$$a=\sqrt{2\gamma_b(1-\frac{1}{\sqrt{2}})}\quad ;\quad b=\sqrt{2\gamma_b(1+\frac{1}{\sqrt{2}})} \tag{2.36}$$

and $\gamma_b=\frac{E_b}{N_o}$ is the average normalized energy per bit. $I_{o(x)}$ is the modified Bessel function of order zero and Q(a,b) is the Q function defined as:

$$Q(a,b)=e^{\frac{-(a^2+b^2)}{2}}\sum_{k=0}^{\infty}\left(\frac{a}{b}\right)^k I_k(ab)\qquad ;\qquad b>a>0 \tag{2.37}$$

Equation (2.35) is plotted in Figure 2.12 as the non-fading case. In the presence of multiplicative Rayleigh fading the BER performance suffers from severe degradation. For a slowly fading channel a new expression can be found [6]

$$P_b=\frac{1}{2}\left[1-\frac{1}{\sqrt{2\left(1+\gamma_s^{-1}\right)^2-1}}\right]\qquad ;\qquad \gamma_s=2\cdot\gamma_b \tag{2.38}$$

Equation (2.38) can be generalized by introducing the fading correlation factor η, defined as the fading correlation between adjacent symbols [7]

$$P_b=\frac{1}{2}\left[1-\frac{\eta}{\sqrt{2\left(1+\gamma_s^{-1}\right)^2-\eta^2}}\right]\qquad ;\qquad \eta=\left\langle\tilde{\alpha}_k\tilde{\alpha}_{k-1}^{*}\right\rangle=J_o(2\pi f_d T) \tag{2.39}$$

The BER curves for various scenarios are illustrated in Figure 2.12. As expected, they are shown to be highly sensitive to the fading correlation, since QDPSK retrieves the new symbol based on the phase of the previous one. If the channel variation is sufficiently fast, there will be an additional error term due to a differential phase added by the fading process. The most noticeable effect is the flooring of the curves, which leads to an irreducible bit error rate, given by:

$$P_b=\frac{1}{2}\left[1-\frac{\eta}{\sqrt{2-\eta^2}}\right] \tag{2.40}$$

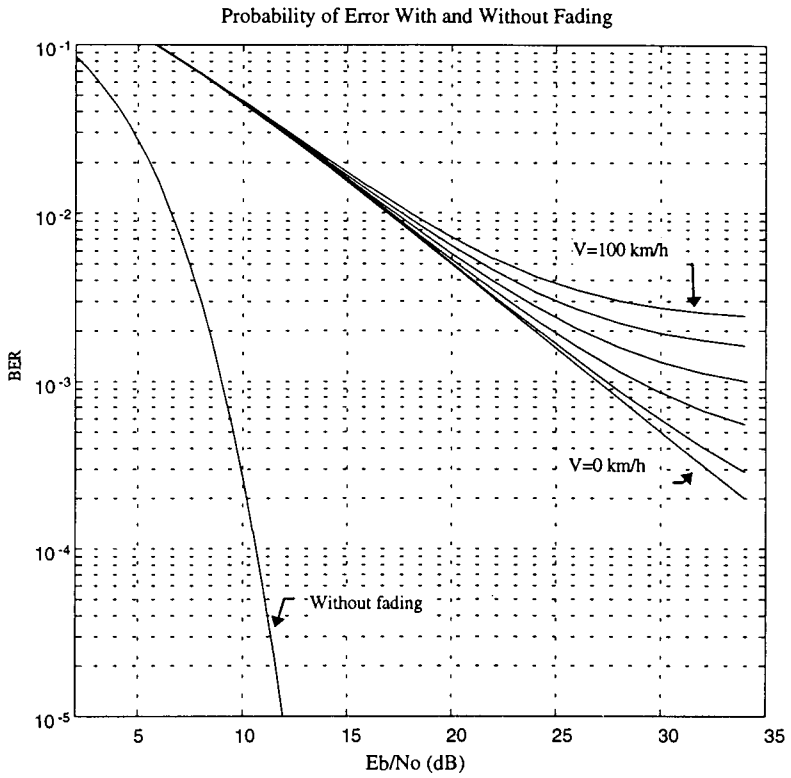

Figure 2.12 BER With and Without Fading

3. SPATIAL CHANNEL SIMULATOR MODEL

This section provides an analytical method to simulate the fast Rayleigh fading phenomenon experienced by a signal when transmitted from a mobile vehicle as it traverses a cell. It is very clear that if a channel simulator is to be used to study the performance of a base station antenna array, as in this particular thesis work, it must somehow take into account the spatial coordinates of the system. It must also allow lengthy simulations, for its intended use requires that the mobile unit be monitored for as long as it stays within the operating range of a particular base station. The transmitter must be allowed to move freely about the cell during the required duration of the test. Depending on the nature of the test, this could either be seconds or hours. Such a simulator is known as a spatial channel simulator.

The majority of existing papers in this area [8,9,10] take the approach of manipulating two randomly generated Gaussian processes to generate the in-phase and in-quadrature components of the fading process, but do not provide any information regarding the position of the source. The latter can be achieved by considering the mobile to be surrounded by a ring of scattering objects, as mentioned in Section 2.1.3. The transmitted waves reflect on these scatterers and combine at the base station with random phase to generate the well known Rayleigh fading effect. This widely accepted model can successfully predict the spatial correlation of signals received by two or more base station antennas. As it turns out, this correlation is very strong for typical antenna array spacings, which validates the assumption that the only difference between the signals received by two adjacent antenna elements is a phase term of the form $e^{j\beta d \sin\theta}$ due to the difference of traveled paths. Still, the remaining concern regarding Jake's model is the limitation of very small observation periods, as noted in Section 2.1.3. With a set of fixed scatterers, it will not be long until the mobile unit leaves the ring. Thus, it would seem quite evident that the ring of scatterers must somehow accompany the motion of the transmitter. The assumption that will be made is that the scatterers are rotating around the mobile unit.

Their velocity has a radial component equal to that of the vehicle and an angular component whose value will be derived later in the chapter. The circular motion of the scatterers ensures that the fading statistics will be realized without altering the delay spread, which is intimately related to the radius of the ring of scatterers [11].

The performance of the spatial channel simulator will be evaluated by comparing the power spectrum and signal statistics given by the simulated model with the desired theoretical ones. Analytical expressions are provided for using the model in conjunction with a base station phased array antenna, composed of seven equally spaced elements. The utilities of such an arrangement will be discussed in the next chapter.

3.1 Theoretical Model

The signal is assumed to be transmitted from a vehicle that is moving in a uniformly scattered area. All the waves received at the base station site arrive from reflections in the scatterers surrounding the mobile unit and, as Figure 3.1 shows, there is no line-of-sight propagation. It will be further assumed that the reflection coefficients are all constant and approximately equal to -1. The scatterers are moving around the mobile with an angular velocity $\dot{\theta}$, as can be seen in Figure 3.2.

The following set of equations fully characterizes the system, and can be easily derived from Figure 3.1 and Figure 3.2:

$$
\begin{aligned}
&\vec{v} = Ve^{j\gamma} \\
&\vec{P}_o = R_o e^{j\alpha_o} \\
&\vec{P}(t) = \vec{P}_o + \vec{v} \cdot t \\
&\vec{p}_{iro} = re^{j\theta_{io}} \\
&\vec{p}_{ir}(t) = re^{j(\theta_{io} + \dot{\theta} \cdot t)} \\
&\vec{p}_i(t) = \vec{P}(t) + \vec{p}_{ir}(t) = R_o e^{j\alpha_o} + V \cdot t \cdot e^{j\gamma} + re^{j(\theta_{io} + \dot{\theta} \cdot t)}
\end{aligned}
\tag{3.1}
$$

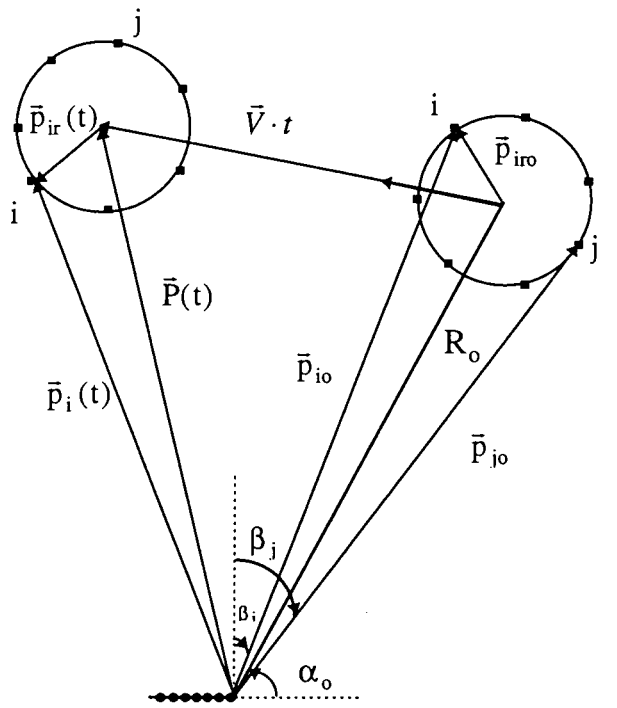

Figure 3.1 Spatial Coordinates of the Model

where the origin of coordinates has been taken to be at the location of the first antenna element and the subindex o denotes the initial state of the system.

It will be assumed from here on that the distance between the mobile and the base station is much greater than the radius of scatterers at any time. The distance from the ith scatterer to the first element of the base station antenna is

$$\begin{aligned}\| \vec{p}_i(t) \| = \Big(& R_o^2 + (V\cdot t)^2 + r^2 + 2R_o V\cdot t\cdot\cos(\alpha_o - \gamma) \\ & + 2r\cdot V\cdot t\cdot\cos(\gamma - (\theta_{io} + \dot{\theta}\, t)) + 2R_o r\cos(\alpha_o - (\theta_{io} + \dot{\theta}\, t))\Big)^{1/2}\end{aligned} \tag{3.2}$$

$$\begin{aligned}\| \vec{p}_i(t) \| = R_o \Bigg(& 1 + \left(\frac{V\cdot t}{R_o}\right)^2 + \left(\frac{r}{R_o}\right)^2 + \frac{2V\cdot t}{R_o}\cos(\alpha_o - \gamma) \\ & + \frac{2r\cdot V\cdot t}{R_o^2}\cdot\cos(\gamma - (\theta_{io} + \dot{\theta}\, t)) + \frac{2r}{R_o}\cos(\alpha_o - (\theta_{io} + \dot{\theta}\, t))\Bigg)^{1/2}\end{aligned}$$

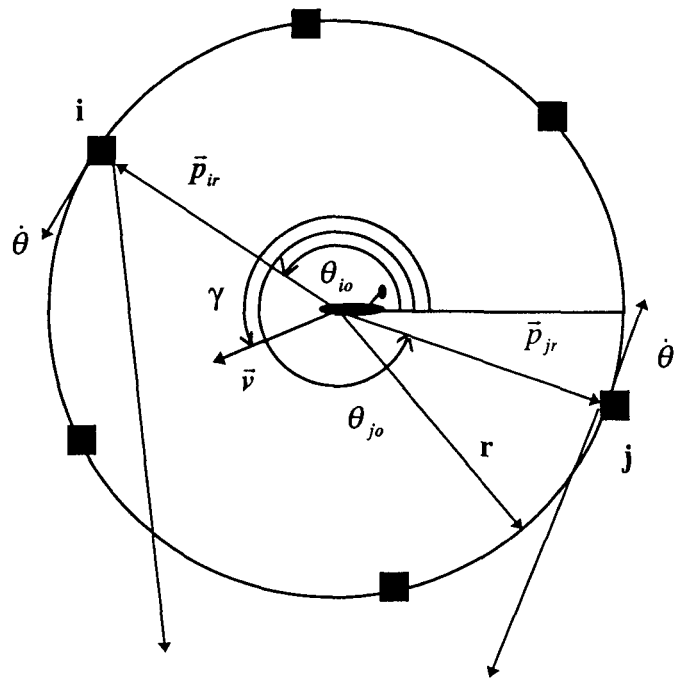

Figure 3.2 Dynamic Scatterers Around the Vehicle

Assuming $r << R_o$ and $V \cdot t << R_o$,

$$\|\vec{p}_i(t)\| \cong R_o + V \cdot t \cdot \cos(\alpha_o - \gamma) + r\cos(\alpha_o - (\theta_{io} + \dot{\theta}\, t)) \tag{3.3}$$

If the transmitted signal is of the form

$$S_{TX}(t) = E_o(t) = |E_o(t)|\, e^{j\varphi(t)} \tag{3.4}$$

the contribution of the ith scatterer to the total signal present at the first antenna element is

$$S_{1i}(t) = \alpha_{att} E_o(t)\, \rho_i\, e^{-j\beta\left(\|\vec{p}_i(t)\| + r\right)} \quad \text{where} \quad \rho_i = |\rho_i|\, e^{j\phi_i} \quad \text{and} \quad \beta = \frac{2\pi}{\lambda} \tag{3.5}$$

α_{att} is an attenuation factor that includes the path loss between transmitter and receiver. It is taken to be constant and approximately equal for all the scatterers.

The total signal is then, given N scatterers:

$$S_1(t) = \alpha_{att} E_o(t)\, e^{-j\beta r} \sum_{i=1}^{N} \rho_i\, e^{-j\beta \left(\| \vec{p}_i(t) \| \right)} \tag{3.6}$$

$$S_1(t) = \alpha_{att} |E_o(t)| e^{j[\varphi(t) - \beta (r + R_o) - \beta V \cdot t \cos(\alpha_o - \gamma)]} \sum_{i=1}^{N} |\rho_i| e^{j[\phi_i - \beta r \cos(\alpha_o - (\theta_{io} + \dot{\theta} t))]} \tag{3.7}$$

The signal present at the first element can be written in a more compact form by defining two terms, one of them independent of the scatterer,

$$\begin{aligned} K(t) &= \alpha_{att} |E_o(t)| e^{j\left(\varphi(t) - \beta (r + R_o) - \beta V \cdot t \cos(\alpha_o - \gamma)\right)} \\ S_{Gi}(t) &= |\rho_i| e^{j[\phi_i - \beta r \cos(\alpha_o - (\theta_i + \dot{\theta} t))]} \end{aligned} \tag{3.8}$$

as

$$S_1(t) = K(t) \sum_{i=1}^{N} S_{Gi}(t) \tag{3.9}$$

According to Figure 3.3, the signal present at the second antenna element is

$$S_2(t) = K(t) \sum_{i=1}^{N} S_{Gi}(t)\, e^{-j\beta d \sin \beta_i(t)} \tag{3.10}$$

and, in general, the signal present at the mth element can be expressed as

$$S_m(t) = K(t) \sum_{i=1}^{N} S_{Gi}(t)\, e^{-j(m-1)\beta d \sin(\beta_i(t))} \tag{3.11}$$

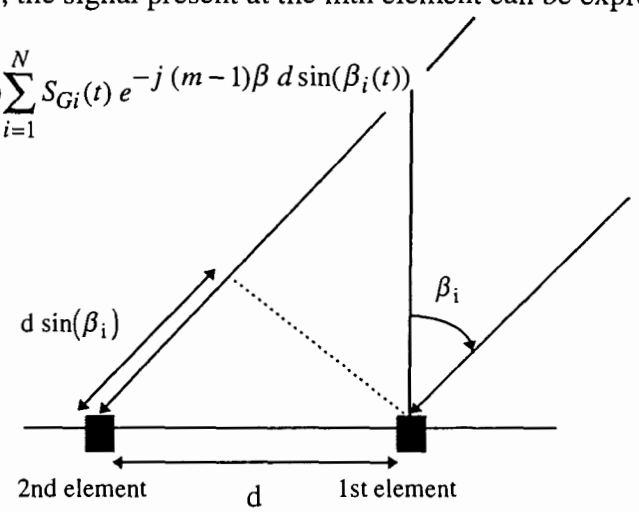

Figure 3.3 Linear Array Front

The actual signal received by each antenna will depend on their individual space factor, i.e. for a microstrip traveling patch antenna

$$SF(\beta_i(t)) = \frac{\cos\left(\frac{\pi}{2}\sin(\beta_i(t))\right)}{\cos(\beta_i(t))} \quad ; \quad 0 \le |(\beta_i(t))| \le \frac{\pi}{2} \quad ; \quad \text{zero elsewhere} \tag{3.12}$$

Then the signal received by the mth antenna element is

$$S_{RXm}(t) = K(t)\sum_{i=1}^{N} S_{Gi}(t)\, SF(\beta_i(t))\, e^{-j(m-1)\beta\, d\sin(\beta_i(t))} \tag{3.13}$$

The resulting combined signal is

$$\begin{aligned} S_{RX_T}(t) &= \sum_{m=1}^{7} w_{m\cdot}(t)\, S_{RXm}(t) \\ &= K(t)\sum_{m=1}^{7} w_{m\cdot}(t) \sum_{i=1}^{N} S_{Gi}(t)\, SF(\beta_i(t))\, e^{-j(m-1)\beta\, d\sin(\beta_i(t))} \end{aligned} \tag{3.14}$$

In this case the weights are of the form

$$w_m(t) = e^{j\psi_m(t)} \text{ , with } \psi_m(t) = (m-1)\psi(t) \tag{3.15}$$

then

$$S_{RX_T}(t) = K(t)\sum_{i=1}^{N} S_{Gi}(t)\, SF(\beta_i(t)) \sum_{m=1}^{7} e^{-j(m-1)\left[\beta\, d\sin(\beta_i(t)) - \psi(t)\right]} \tag{3.16}$$

The last summation is a geometric series that defines the array factor of the antenna

$$\begin{aligned} S_{RX_T}(t) = K(t)\sum_{i=1}^{N} S_{Gi}(t)\, SF(\beta_i(t))\, e^{-3j\left[\beta\, d\sin(\beta_i(t)) - \psi(t)\right]} \\ \cdot \frac{\sin\left[\frac{7}{2}\left(\beta\, d\sin(\beta_i(t)) - \psi(t)\right)\right]}{\sin\left[\frac{1}{2}\left(\beta\, d\sin(\beta_i(t)) - \psi(t)\right)\right]} \end{aligned} \tag{3.17}$$

By defining

$$AF(\beta_i(t),\psi(t)) = \frac{\sin\left[\frac{7}{2}\left(\beta\, d \sin(\beta_i(t)) - \psi(t)\right)\right]}{\sin\left[\frac{1}{2}\left(\beta\, d \sin(\beta_i(t)) - \psi(t)\right)\right]} \tag{3.18}$$

and

$$G(\beta_i(t),\psi(t)) = SF(\beta_i(t)) \cdot AF(\beta_i(t),\psi(t)) \tag{3.19}$$

the combined signal can be written as

$$S_{RX_T}(t) = K(t)\sum_{i=1}^{N} S_{Gi}(t)\, G(\beta_i(t),\psi(t))\, e^{-3j\left[\beta\, d \sin(\beta_i(t)) - \psi(t)\right]} \tag{3.20}$$

It can be seen from Equation (3.20) that the overall effect of the array is to multiply each of the N reflected waves by its own factor, prior to adding them. This factor, in turn, depends on the direction of the incoming wave relative to the center of the main lobe. Also, $\psi(t)$ defines the position of the center of the beam and has to be dynamically adjusted as the vehicle traverses the cell.

Ideally, $\psi(t) = \beta\, d \sin\left(\frac{\pi}{2} - \alpha(t)\right) = \beta\, d \cos\left(\alpha(t)\right)$ where $\alpha(t) = \angle \tilde{P}(t)$ (3.21)

Two parameters remain to be evaluated. The angular velocity of the scatterers can be determined by analyzing the contribution of one of the scatterers to the doppler frequency:

$$S_{RXi}(t) = |E_o(t)|\, A_{RXi}(t)\, e^{j(\varphi(t) + \theta_{RXi}(t))} \tag{3.22}$$

where

$$\begin{aligned} A_{RXi}(t) &= \alpha_{att} |\rho_i|\, G(\beta_i(t),\psi(t)) \\ \theta_{RXi}(t) &= -\beta\,(r + R_o) - \beta\, V \cdot t \cdot \cos(\alpha_o - \gamma) \\ &\quad + \phi_i - \beta\, r \cdot \cos(\alpha_o - (\theta_i + \dot{\theta} \cdot t)) - 3 \cdot (\beta\, d \sin(\beta_i(t)) - \psi(t)) \end{aligned} \tag{3.23}$$

The contribution to the doppler frequency can be found by differentiating $\theta_{RXi}(t)$ with respect to time

$$\varpi_m = \frac{d\theta_{Rxi}(t)}{dt} = -\beta V \cdot \cos(\alpha_o - \gamma) - \beta r \cdot \dot{\theta} \sin(\alpha_o - (\theta_i + \dot{\theta} \cdot t)) \\ - 3\beta d \cdot \beta_i'(t) \cos(\beta_i(t)) + 3\psi'(t) \tag{3.24}$$

The last two terms are very small and can be discarded. The second term provides the expected spectral characteristics, and the first one, $\beta V \cdot \cos(\alpha_o - \gamma)$, is a spectral shift that needs to be compensated for. The resulting simplified expression gives a maximum doppler frequency $|\varpi_{max}| = \beta r \cdot \dot{\theta}$. Finally, by equating this result to the desired value for the maximum doppler frequency βV, it can be seen that a proper choice for the angular velocity of the scatterers is

$$\dot{\theta} = \frac{V}{r} \tag{3.25}$$

The radius of scatterers r is determined from the delay spread Δ [11]. The result is

$$r = \sqrt{2} \cdot c \cdot \Delta \tag{3.26}$$

Log-normal fading was not included in the model. Although it is a very straightforward feature to implement, it would have unnecessarily complicated the analysis and slowed down the computer simulations.

3.2 Simulation Results

The parameters used in the simulations were:

$E_o(t) = 1$

$\vec{P}_o = 5000e^{j\frac{\pi}{2}}$ the initial position, 5km from the base station, at boresight

$\vec{v} = 13.89e^{j\pi}$ the vehicle speed, 50km/h traveling West

$\Delta = 1.2\ \mu s$ the delay spread

$r = 509$ m the radius of the ring of scatterers

$\dot{\theta} = 2.728 \cdot 10^{-2}$ rad / s the angular velocity of the scatterers

$f_c = 815$ Mhz the carrier frequency

N=25 the number of scatterers considered

Figure 3.4 shows the simulated fading envelope as seen by the first array element, normalized to its root mean square value.

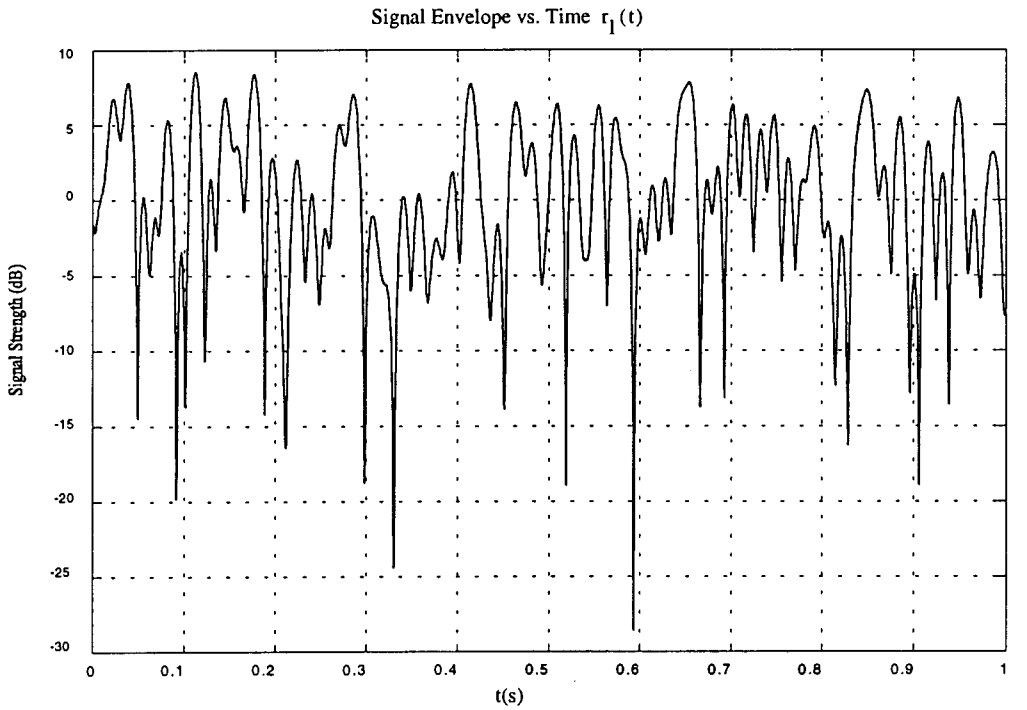

Figure 3.4 Sample of the Simulated Envelope

By writing Equation (3.9) as $s_i(t) = r_i(t)e^{j\theta_i(t)}$, the above mentioned envelope is $r_i(t)$.

The following two figures show the characteristic U shape of the power spectrum of the complex envelope. It also confirms that the maximum doppler frequency is accurate, in this case 37.73 Hz.

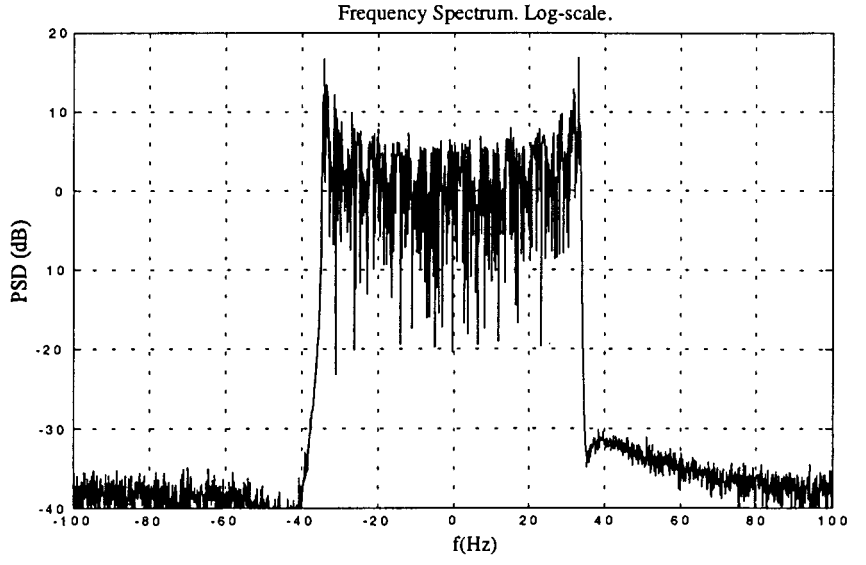

a)

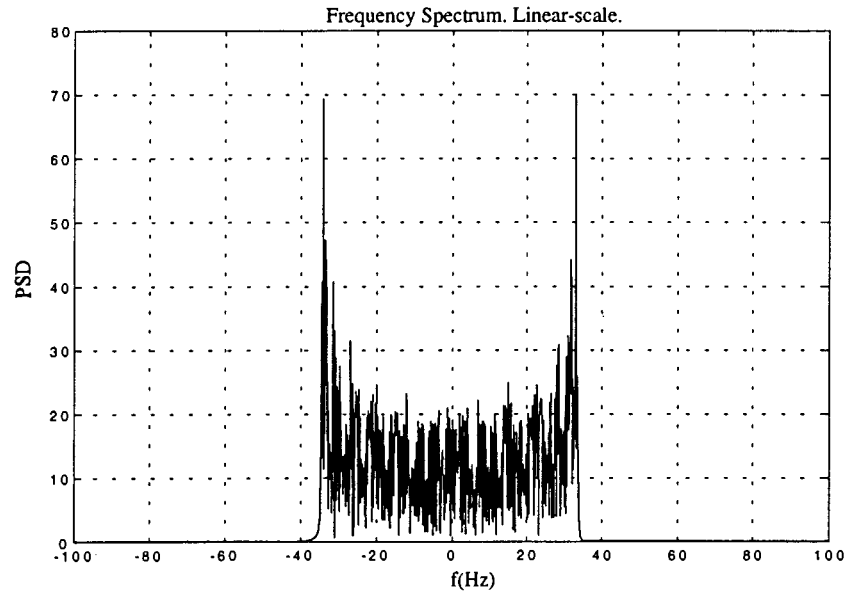

b)

Figure 3.5 Simulated Signal Spectrum

The statistical properties of the model are tested and plotted in the following figures. Figure 3.6 displays a bar graph of the envelope distribution versus the theoretical probability density function for a Rayleigh distributed random variable, as described in Equation (2.8). For the sake of comparison, the envelope has been normalized to its rms value:

$$\sqrt{E\left[r1^2\right]} = \sqrt{2\sigma^2} \tag{3.27}$$

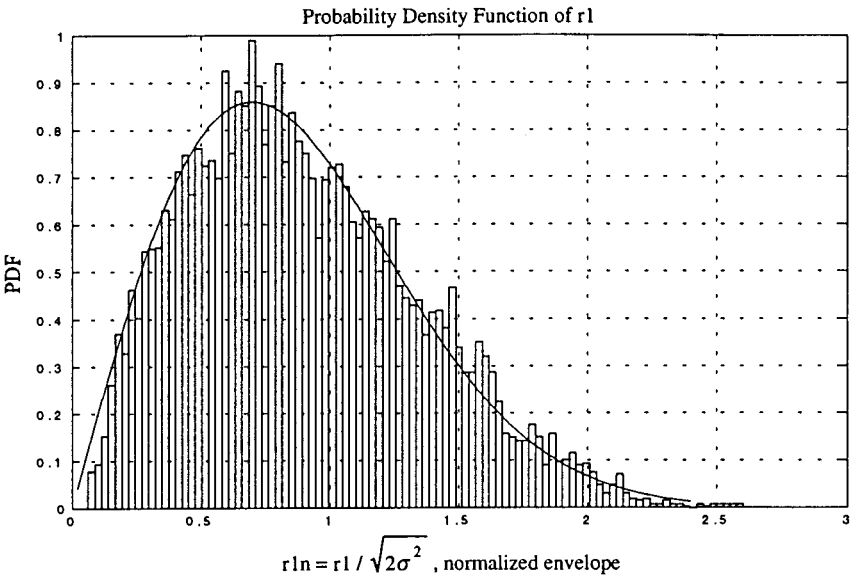

Figure 3.6 Simulated Envelope Distribution

Perhaps the best way to show how closely the result is to the ideal Rayleigh distribution is by plotting the cumulative distribution, which can be seen in the next two figures, where the dashed trace is the theoretical curve. Figure 3.8 is a very useful representation of the CPD of a Rayleigh faded envelope. By defining the variable $x = e^{-r1n^2}$, Equation (2.9) becomes:

$$P_{r1n}(r1n) = 1 - x \tag{3.28}$$

so that the CPD can be plotted as a linear function of the new variable x.

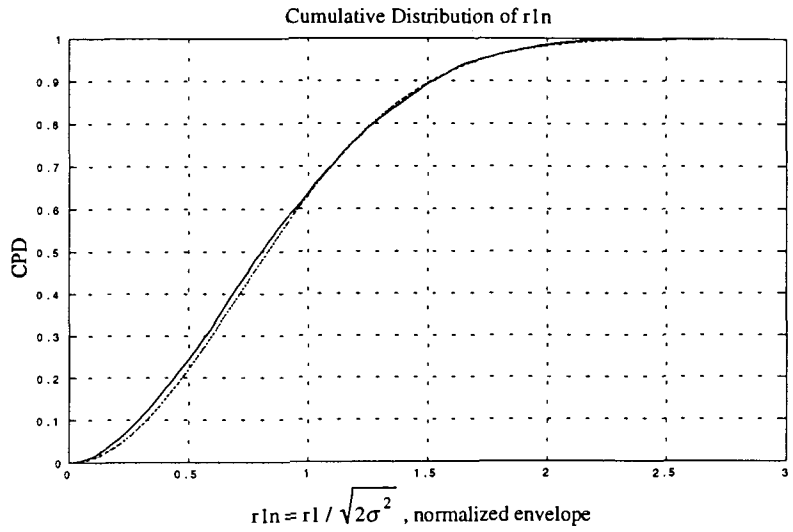

Figure 3.7 Simulated Envelope Cumulative Distribution

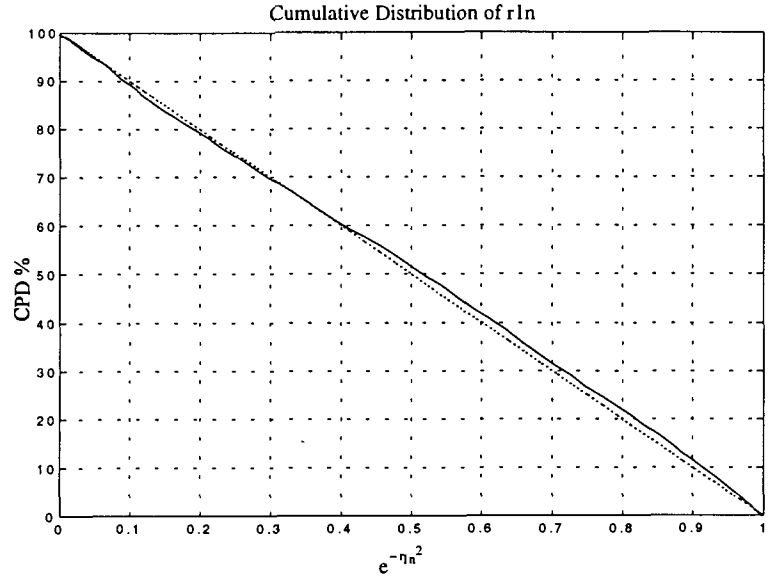

Figure 3.8 Simulated Envelope Cumulative Distribution
Linear Scale

The PDF of the phase component is also evaluated. The result agrees very closely with the expected uniform distribution, as Figure 3.9 shows.

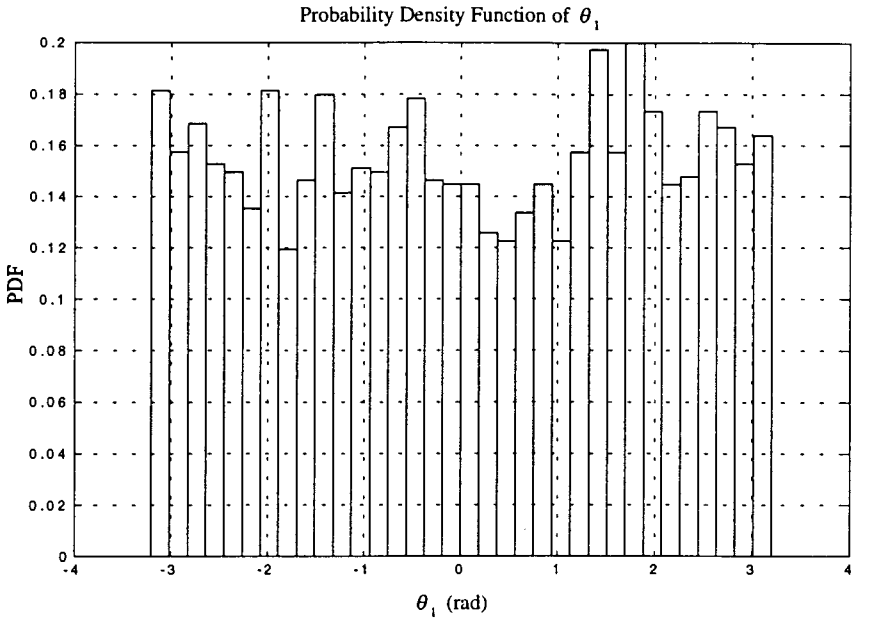

Figure 3.9 Simulated Phase Distribution

The main conclusion to be drawn from the previous results is that the model effectively recreates the expected characteristics of the fading environment. It remains to be seen if the individual signals from each antenna element can be combined to generate directional beams. In general, the signals across the array front are found to be highly correlated and it can be assumed that the distortion introduced in the array space factor will be minimal. The resulting array pattern can be obtained by taking a snapshot of the 7 signals and combining them using the appropriate set of complex weights that would scan the angular sector, from -90 to +90 degrees. The result should follow the shape of the array space factor. The expression for the weights is

$$w_{ik} = e^{j\beta \cdot d(i-1) \cdot \sin(k \cdot \Delta\beta)} \; ; \; i = 1..7 \; ; \quad M = \frac{\pi}{2 \cdot \Delta\beta} \; ; \quad k = -M...M \tag{3.29}$$

where $\Delta\beta$ is the angle resolution.

Figure 3.10 shows the result of plotting the magnitude of the combined signal versus $k \cdot \Delta\beta$, the phase shift from boresight. This is the space factor at a given instant t_o. For sufficiently large values of R_0, the distance from the mobile to the base station, the transmitter can be considered similar to a point source and therefore, the array space factor will not change significantly with time. As the distance becomes progressively smaller, the punctual source approach loses validity and the nulls tend to oscillate about their original position. The oscillation is, however, rather small and its only effect is to provide smoother transitions between sidelobes on the average pattern. This average pattern can be seen in Figure 3.10 as a dashed line.

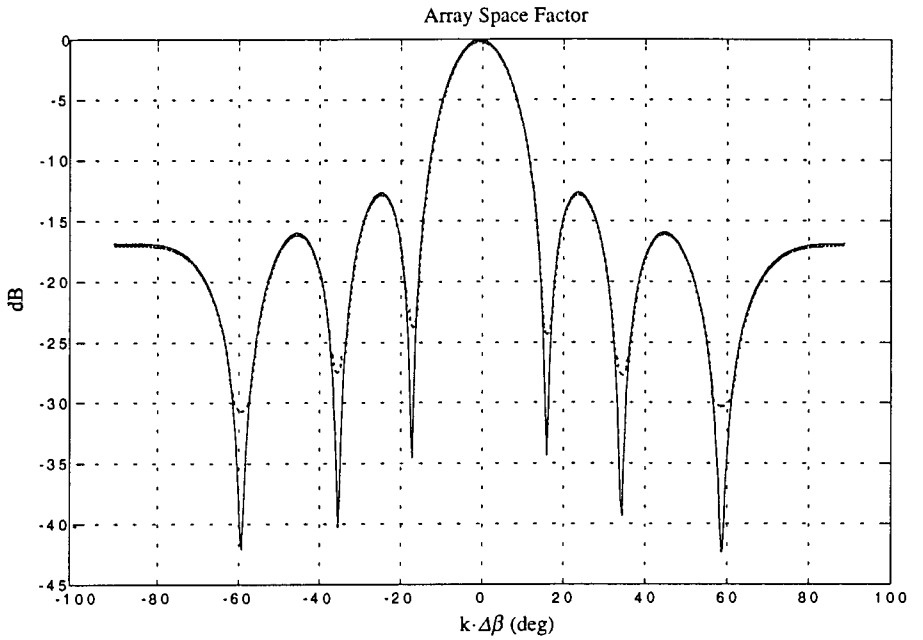

Figure 3.10 Simulated Array Pattern

Figure 3.11 illustrates the received signal when a pulse of length 0.5 μs is transmitted. There are two noticeable peaks that take place very close to the maximum and minimum delays. This is due to the fact that a higher number of scatterers are placed at those distances. The shape of the delay profile can be altered, if necessary, by introducing additional rings of scatterers with different values for the reflection coefficients.

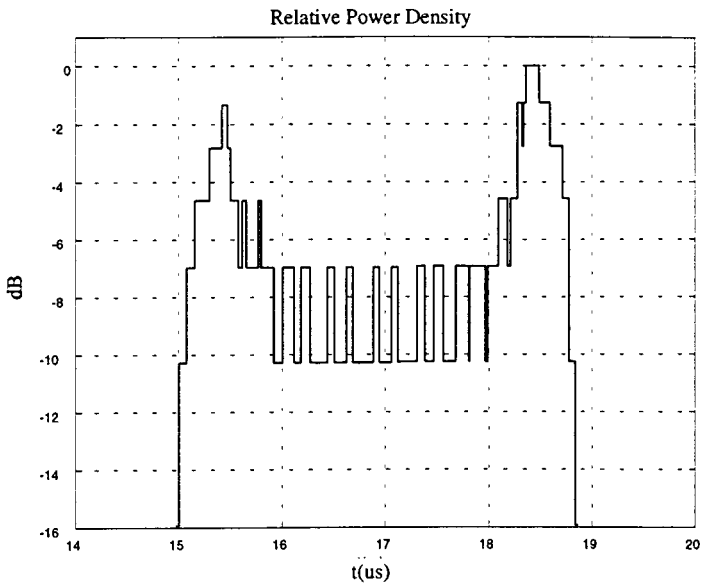

Figure 3.11 Delay Spread Profile

The average delay is 16.7 μs, which corresponds to an average distance of 5Km. Likewise, the resulting delay spread is exactly 1.2 μs.

4. APPLICATIONS OF THE MODEL

The simulated space factor of the array obtained in the last section can be seen in Figure 4.1 in a polar plot. The ring of scatterers has been added to show the total geometry of the simulation. It is obvious, from Figure 4.1, that any practical system that uses the antenna array at the base station will have to be able to automatically track the vehicle.

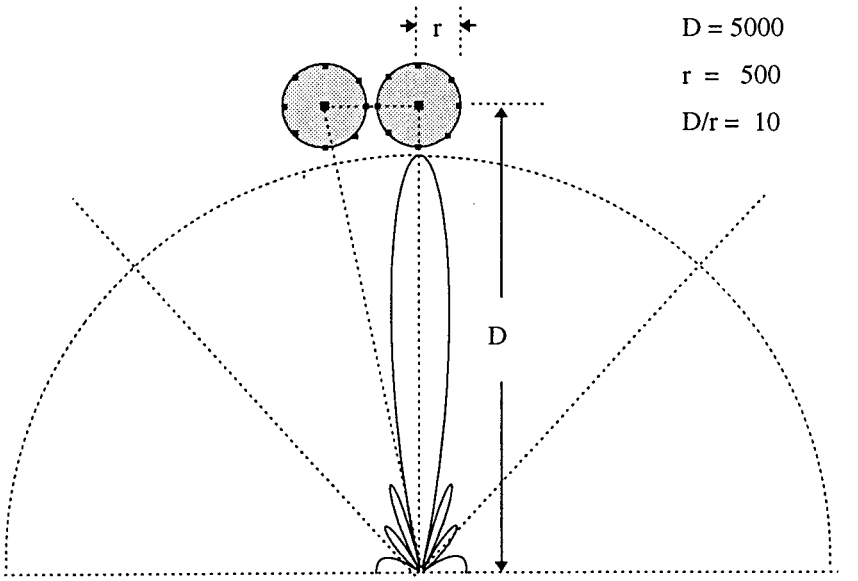

Figure 4.1 Array's Main Beam

It can also be seen that if the main lobe were to point slightly off the vehicle, the ring of scatterers would be unevenly illuminated, so that the contribution of each scatterer to the total signal could be modified just enough to significantly reduce the depth of a fade. By adequately combining the signals obtained from the two beams, deep nulls could be avoided, thus improving the BER of the system.

In this section a practical algorithm to perform tracking is developed and tested. In addition, the possible use of multiple beams for diversity purposes is investigated.

4.1 Tracking

The configuration used to implement the tracking algorithm can be seen in Figure 4.2. Two beams are formed at either side of the mobile unit. As the vehicle moves away from its previous location the average power received by one of the beams will increase, while the other one decreases accordingly. The difference in received power can be used to determine the new position of the vehicle. To this end, the ratio χ is defined as the quotient of the signal power received by the two beams:

$$\chi^2 = \frac{P_1}{P_2} \cong \frac{|G(\beta_o,\psi_1)|^2}{|G(\beta_o,\psi_2)|^2} = \frac{|AF(\beta_o,\psi_1)|^2}{|AF(\beta_o,\psi_2)|^2}$$
$$= \left|\frac{\sin(\frac{7}{2}(\beta\, d\sin(\beta_o)-\psi_1))}{\sin(\frac{1}{2}(\beta\, d\sin(\beta_o)-\psi_1)}\right|^2 \left|\frac{\sin(\frac{1}{2}(\beta\, d\sin(\beta_o)-\psi_2))}{\sin(\frac{7}{2}(\beta\, d\sin(\beta_o)-\psi_2)}\right|^2 \qquad (4.1)$$

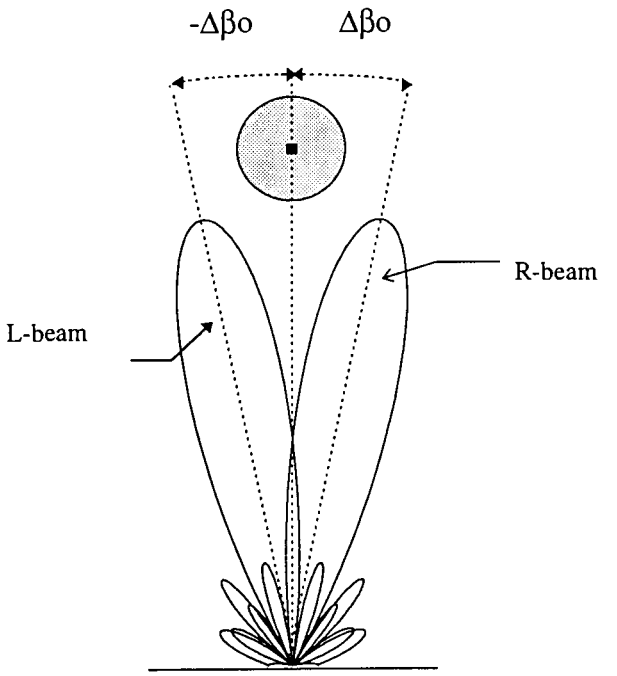

Figure 4.2 Beam Arrangement for Tracking

In this case

$\psi_1 = \beta\, d \sin(\Delta\beta_o)$; $\psi_2 = -\beta\, d \sin(\Delta\beta_o)$; $\beta\, d = \pi$;

so that (4.1) can be rewritten as

$$\chi^2 \equiv \left| \frac{\sin\left(\frac{7\pi}{2}(\sin(\beta_o) - \sin(\Delta\beta_o))\right)}{\sin\left(\frac{\pi}{2}(\sin(\beta_o) - \sin(\Delta\beta_o))\right)} \right|^2 \left| \frac{\sin\left(\frac{\pi}{2}(\sin(\beta_o) + \sin(\Delta\beta_o))\right)}{\sin\left(\frac{7\pi}{2}(\sin(\beta_o) + \sin(\Delta\beta_o))\right)} \right|^2 \tag{4.2}$$

which can be decomposed in two terms of the form

$$\left| \frac{\sin(A \pm B)}{\sin(A \mp B)} \right|^2 = \left| \frac{1 \pm \frac{\tan(B)}{\tan(A)}}{1 \mp \frac{\tan(B)}{\tan(A)}} \right|^2 \tag{4.3}$$

leading to

$$\chi \equiv \left| \frac{1 + \frac{\tan\left(\frac{\pi}{2}\sin(\Delta\beta_o)\right)}{\tan\left(\frac{\pi}{2}\sin(\beta_o)\right)}}{1 - \frac{\tan\left(\frac{\pi}{2}\sin(\Delta\beta_o)\right)}{\tan\left(\frac{\pi}{2}\sin(\beta_o)\right)}} \right| \left| \frac{1 - \frac{\tan\left(\frac{7\pi}{2}\sin(\Delta\beta_o)\right)}{\tan\left(\frac{7\pi}{2}\sin(\beta_o)\right)}}{1 + \frac{\tan\left(\frac{7\pi}{2}\sin(\Delta\beta_o)\right)}{\tan\left(\frac{7\pi}{2}\sin(\beta_o)\right)}} \right| \tag{4.4}$$

The above equation can be significantly simplified by noting that the two terms on the right hand side yield similar values for small values of βo. Thus, (4.4) can be rewritten as

$$\chi \equiv \left| \frac{1 + \frac{\tan\left(\frac{\pi}{2}\sin(\Delta\beta_o)\right)}{\tan\left(\frac{\pi}{2}\sin(\beta_o)\right)}}{1 - \frac{\tan\left(\frac{\pi}{2}\sin(\Delta\beta_o)\right)}{\tan\left(\frac{\pi}{2}\sin(\beta_o)\right)}} \right|^2 \tag{4.5}$$

Figure 4.3 shows the result of approximating (4.4) by (4.5). In this simulation the value chosen for $\Delta\beta_o$ was 10 degrees. Note that the error is minimal for small values of βo.

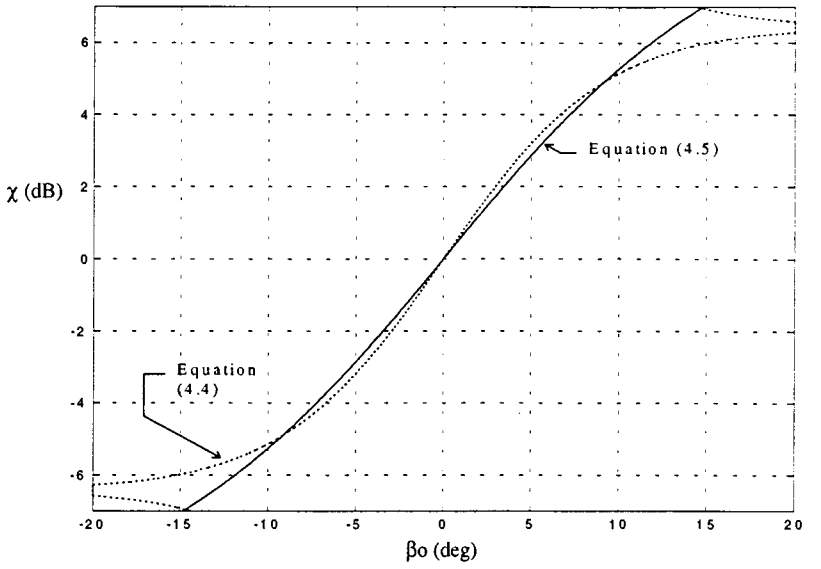

Figure 4.3 Equation (4.4) vs. Equation (4.5)

Finally, βo can be found in terms of the parameter χ,

$$\beta_o = \sin^{-1}\left(\frac{2}{\pi}\tan^{-1}\left(\frac{1+\chi-2\sqrt{\chi}}{\chi-1}\tan\left(\frac{\pi}{2}\sin\Delta\beta_o\right)\right)\right) \tag{4.6}$$

When the amount of power received by the two beams is equal χ=1, and βo=0, the requirement for perfect tracking is met.

One important consideration is to determine the time interval T that needs to be used to average the received signal power. T has to be short enough that the local mean is not wiped out from the averaging process. On the other hand, if T is too short the estimated average power will contain residual short term fading. In general, [3] the value for T in units of distance should be anywhere between 40 and 200 wavelengths. For tracking purposes it is necessary to have an estimate of the signal power as soon as possible, so

that the vehicle cannot be too far from its original position. To this effect, a minimum value of 40 wavelengths was used in the simulations. Figure 4.4 plots the power received by the two fixed beams of Figure 4.2 when the mobile is traveling East, moving away from the R-Beam, towards the L-Beam.

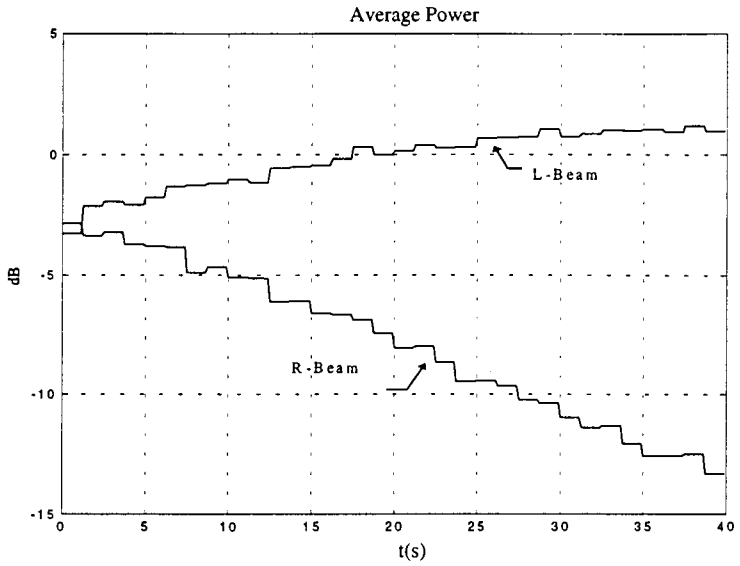

Figure 4.4 Average Power Received by the L and R Beams

The tracking algorithm was tested using 4 different values for both the velocity of the mobile and its direction of travel. Assuming the direction of boresight is North:

i) 50 km/h , 45 degrees relative to the array front (North-East).

ii) 50 km/h , 180 degrees relative to the array front (West).

iii) 75 km/h , 180 degrees relative to the array front (West)

iv) 75 km/h , 0 degrees relative to the array front (East)

The rest of the parameters were those previously used in Section 3.2. An important geometrical parameter is the ratio D/r, where $D = \|\vec{P}_o\|$ and r is the radius of scatterers. In this case D/r=10.

The results are shown in Figure 4.5. The algorithm proves to be very robust and quite insensitive to changes in velocity or direction of travel. Some statistics were computed for a variety of simulator parameters such as radius of scatterers, distance between mobile

and base station, and velocity and direction of travel. The mean of the error was +0.03 and its variance ±0.05°. The maximum error ever experienced was +0.5°.

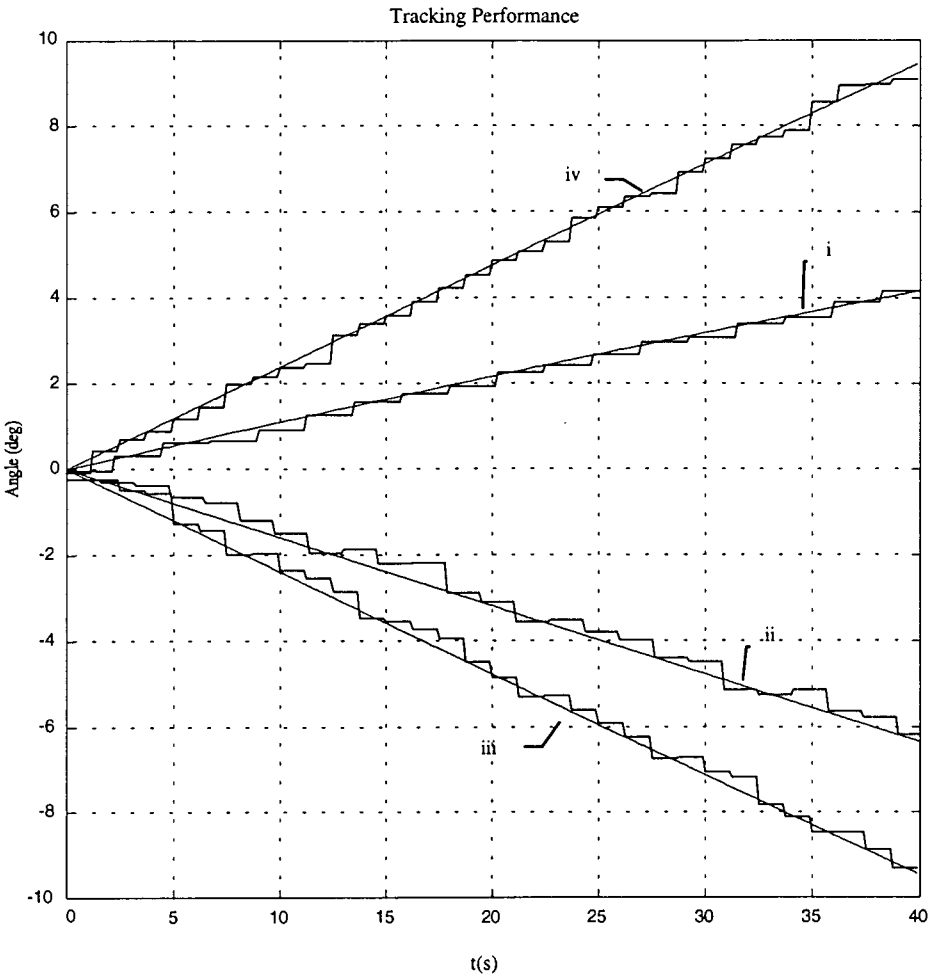

Figure 4.5 Tracking Algorithm Performance

4.2 Angle Diversity

The configuration used to investigate angle diversity is shown in Figure 4.6. There is one beam pointing directly at the mobile plus a second one which is offset by θ degrees. The former will be referred to as the C-beam (center) and the latter as the R-beam (right). From here on the position of the vehicle will be considered to be perfectly known. This information is used by the antenna control to constantly update the phase shifters that generate both beams, so that the relative geometry of Figure 4.6 remains constant with time. Then, without loss of generality, the vehicle can be assumed to be always at boresight.

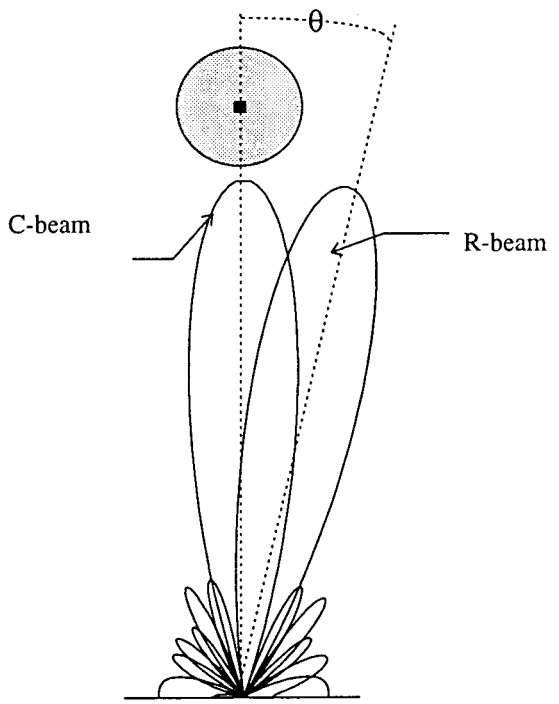

Figure 4.6 Beam Arrangement for Angle Diversity

The model described in Section 3 was utilized to simulate the signals received by the seven array elements. The parameters used were those given in Section 3.2. The combined signals received by the C-beam and R-beam are

$$s_{RX_{TC}} = \sum_{m=1}^{7} w_{Cm} s_{RXm}(t) \quad \text{with} \quad w_{Cm} = e^{j(m-1)0} = 1$$
$$s_{RX_{TR}} = \sum_{m=1}^{7} w_{Rm} s_{RXm}(t) \quad \text{with} \quad w_{Rm} = e^{j(m-1)kd\sin\theta} \tag{4.7}$$

Figure 4.7 illustrates the signal envelopes that correspond to phase shifts of 0, 1 and 2 degrees from boresight.

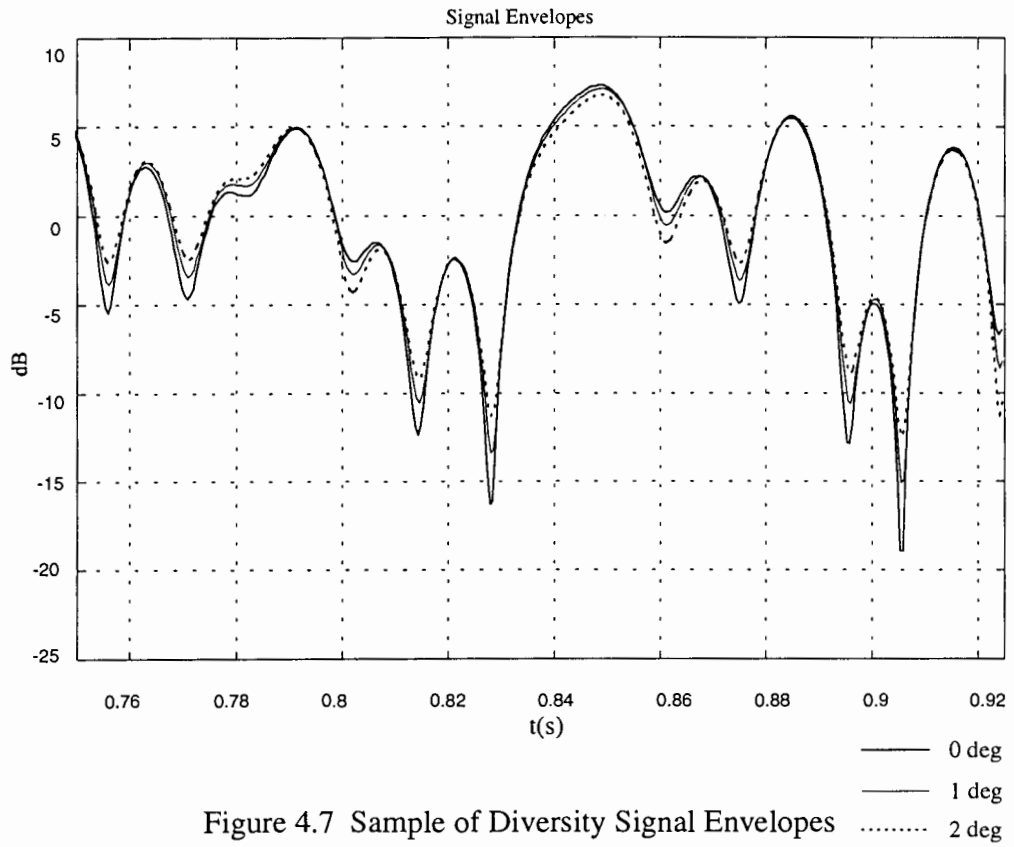

Figure 4.7 Sample of Diversity Signal Envelopes

The envelopes of the three generated signals are strongly correlated. However, as the signals experience fades the envelopes become uncorrelated. This effect is particularly noticeable in the neighborhood of deep nulls. The degree of correlation between the signal envelopes is determined, in general, by the phase shift applied and the ratio D/r described in Section 4.1.

This technique provides a unique way to obtain a postdetection diversity branch. Significant improvement in signal performance can be achieved by combining the waveforms received by the two beams. Maximal Ratio Combining (MRC) proves to be a very well suited combining technique for this particular application as will be seen in Section 4.3. The following is a brief description of the implementation of MRC in the system and its effect on the combined signal.

Let $u_1(t)$ and $u_2(t,\theta)$ denote the complex envelopes of the signals received by the C-beam and the R-beam respectively, where the dependence of the latter on the phase shift is explicitly stated. The output of the combiner can be expressed as

$$v(t,\theta) = \sum_{k=1}^{2} \alpha_k u_k(t,\theta) = \alpha_1 u_1(t) + \alpha_2 u_2(t,\theta) \tag{4.8}$$

In Maximal Ratio Combining [3]

$$\alpha_k = K\frac{u^*_k}{\eta_k} \quad ; \quad \text{In this case} \quad \alpha_1 = K\frac{u^*_1}{\eta_1} \quad \text{and} \quad \alpha_2 = K\frac{u^*_2}{\eta_2} \tag{4.9}$$

If the noise is considered to be introduced entirely by the receiver $\eta_1 = \eta_2$ then it is useful to define a new parameter μ as

$$\mu = \frac{\alpha_1}{\alpha_2} = \frac{u_1^*}{u_2^*} \tag{4.10}$$

and imposing the constraint:

$$\alpha_1^2 + \alpha_2^2 = 1 \tag{4.11}$$

α_1 and α_2 can be rewritten as

$$\alpha_1 = \sqrt{\frac{\mu^2}{1+\mu^2}} \quad \text{and} \quad \alpha_2 = \sqrt{\frac{1}{1+\mu^2}} \tag{4.12}$$

MRC yields its best results when the two diversity signals have the same power and are totally uncorrelated. In this case, the probability of a deep fade occurring simultaneously in both signals is remote. Figure 4.8 shows the result of using MRC when

θ = 10. Even with a relatively high correlation between the two envelopes, the deep fade at t=43 ms present in the original signal can be significantly reduced. At this point the limitations of this technique also become apparent. As θ increases, and consequently the correlation coefficient becomes smaller, so does the power level received by the R-beam. At the limit, and neglecting the side lobes of the array pattern, the correlation coefficient would be zero, but so would the received power as the beam would be totally off target. Therefore there is a clear compromise between correlation coefficient and signal power, which translates to an optimum value of θ for a particular D/r ratio.

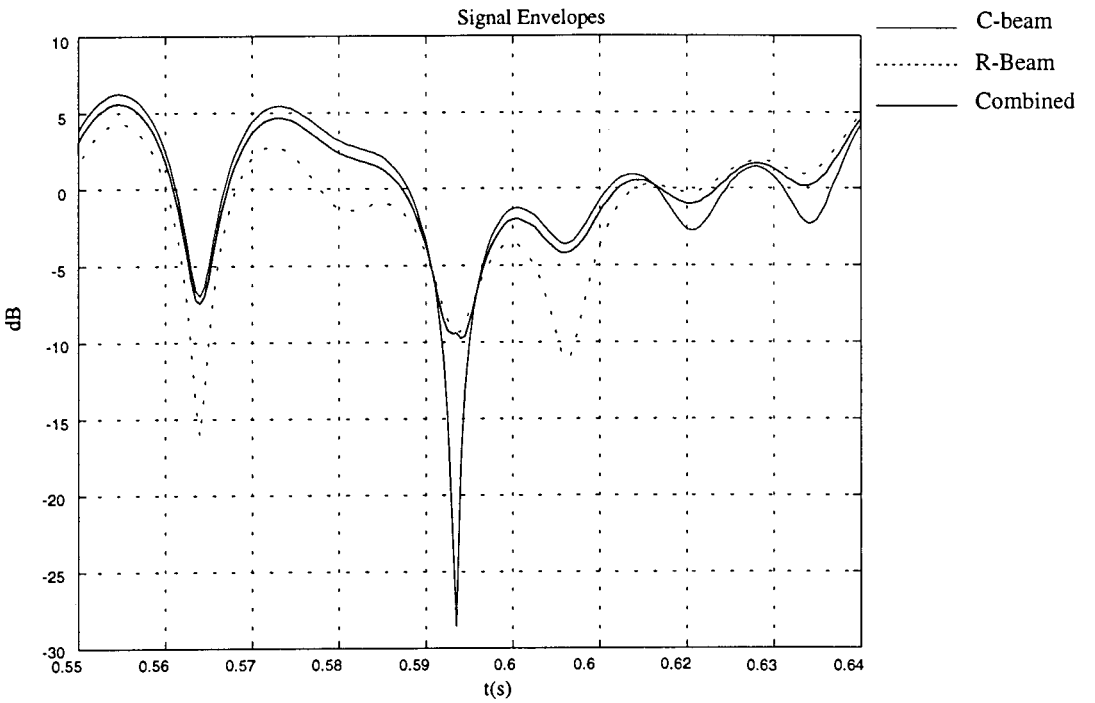

Figure 4.8 Improvement in Envelope Quality due to MRC

Because errors are more likely to occur in the vicinity of deep fades the percentage of time that the envelope drops below a certain level is a good indicator of the signal quality. Thus, the cumulative distribution function of the normalized envelope will be analyzed and used to determine the improvement achieved in each particular case. To this end, the following variables are defined:

γ : signal to noise ratio of the combined signal $v(t,\theta)$

Γ_1 , Γ_2 : signal to noise ratio of the individual branches $u_1(t)$ and $u_2(t,\theta)$

ρ : correlation coefficient of the complex envelopes

From [3] the cumulative distribution of γ is given by the expression

$$P(\gamma \le x) = 1 - \sum_{j=1}^{M} \frac{(\lambda_j)^{M-1} \exp(-x/\lambda_j)}{\prod_{k \ne j}^{M} (\lambda_j - \lambda_k)} \tag{4.13}$$

or for M=2

$$P(\gamma \le x) = 1 - \frac{1}{\lambda_1 - \lambda_2}\left[\lambda_1 \exp(-x/\lambda_1) - \lambda_2 \exp(-x/\lambda_2)\right] \tag{4.14}$$

where λ_1 and λ_2 are the eigenvalues of the matrix $[\Lambda]$defined as

$$[\Lambda] = \begin{bmatrix} \Gamma_1 & \rho\sqrt{\Gamma_1\Gamma_2} \\ \rho^*\sqrt{\Gamma_1\Gamma_2} & \Gamma_2 \end{bmatrix} \tag{4.15}$$

They can be found to be

$$\begin{aligned} \lambda_1 &= \frac{1}{2}\left[\Gamma_1 + \Gamma_2 - \sqrt{(\Gamma_1 + \Gamma_2)^2 - 4\Gamma_1\Gamma_2(1 - |\rho|^2)}\right] \\ \lambda_2 &= \frac{1}{2}\left[\Gamma_1 + \Gamma_2 + \sqrt{(\Gamma_1 + \Gamma_2)^2 - 4\Gamma_1\Gamma_2(1 - |\rho|^2)}\right] \end{aligned} \tag{4.16}$$

As mentioned earlier, the noise power is considered to be equal in both branches, thus it factors out in the calculation of the cumulative distribution and need not be considered. Therefore, Γ_1 and Γ_2 can be replaced by P_1 and P_2 ,the signal power of the individual branches.

P_1 , P_2 and ρ were obtained from the simulated signals $u_1(t)$ and $u_2(t,\theta)$ for selected values of θ. The results correspond to a value of D/r=10 and are listed in Table 4.1.

θ (deg)	ρ_{12}	P_2 / P_1
0	1.0	1
2	0.9898	0.9996
4	0.9585	0.9993
6	0.9032	0.9542
8	0.81908	0.8225
10	0.69856	0.5889
12	0.53275	0.3881
14	0.31867	0.2359
16	0.092052	0.1357
18	0.0068387	0.0803

Table 4.1 Correlation Coefficients and Relative Power vs. θ

Figure 4.9 plots the cumulative distribution of γ in logarithmic scale for values of θ in increments of 2°. The ordinate represents the probability that the amplitude is less than the abscissa. For example, with a phase shift of 0° (without diversity), the probability of the envelope dropping 20 dB below its average value is 0.5%, whereas in the best case, with a phase shift of 14° the same probability drops to 0.015%. Initially, any small change in the correlation coefficient is enough to provide a significant improvement. As θ increases the signals become progressively uncorrelated while their relative power level is still quite significant. However, as the power level decreases the improvement tends to saturate and beyond approximately 14° the curves start slowly moving back inwards. The cycle does not completely reverse, but oscillates around a certain point due to the presence of sidelobes in the array pattern.

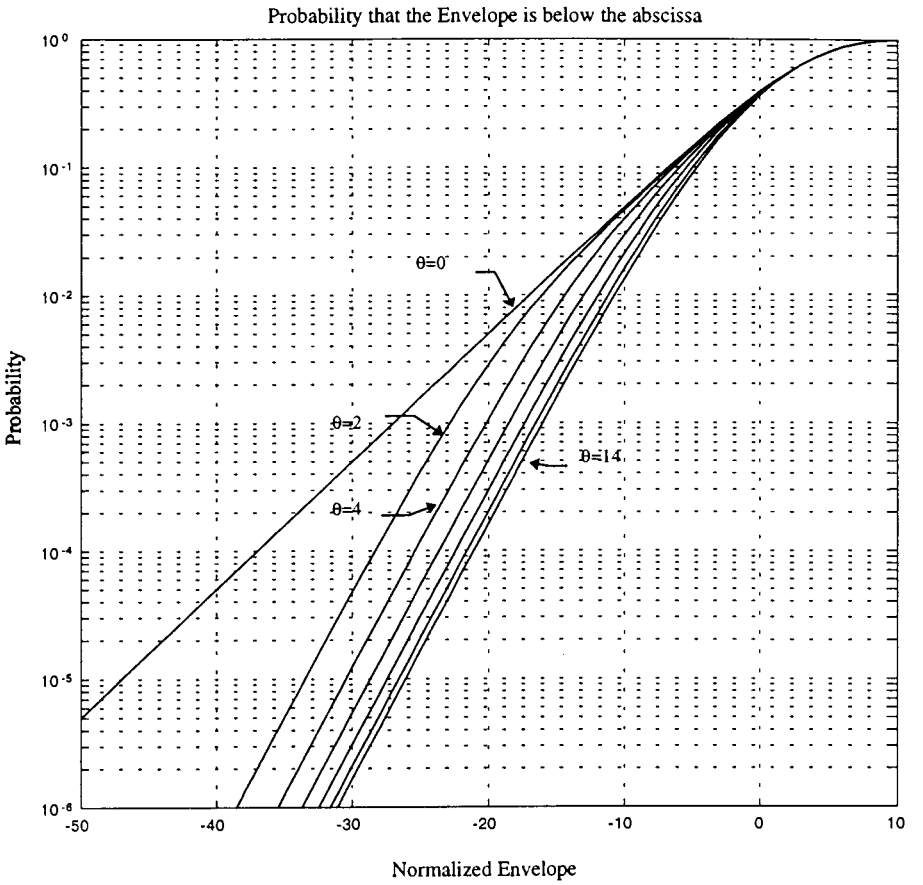

Figure 4.9 Improvement in Envelope Quality vs. θ

As stated, the results shown above correspond to a D/r ratio of 10. The process was iterated using values of D/r ranging from 5 to 30. For the sake of comparison a new graphing method will be used that allows the incorporation of all the results in the same plot. It consists of taking the 0.1% probability point as the one of interest. The abscissa points that correspond to this level are then plotted in Figure 4.10 as a function of θ. The newly generated plot is read as follows: the normalized envelope is greater than x dB with probability 99.9%, x being the ordinate value. There are several interesting conclusions that can be drawn from the plots. First, the curves are symmetrical for negative values of θ, which is not at all surprising. Second, the overall behavior remains basically unchanged: there is a fast rising towards the optimal point followed by a slower decay. The main difference lies in the value achieved at the optimal point which varies greatly

from one curve to another. Whereas an overall improvement of 13 dB can be achieved when D/r=5, it will only be of roughly 6 dB for D/r=30.

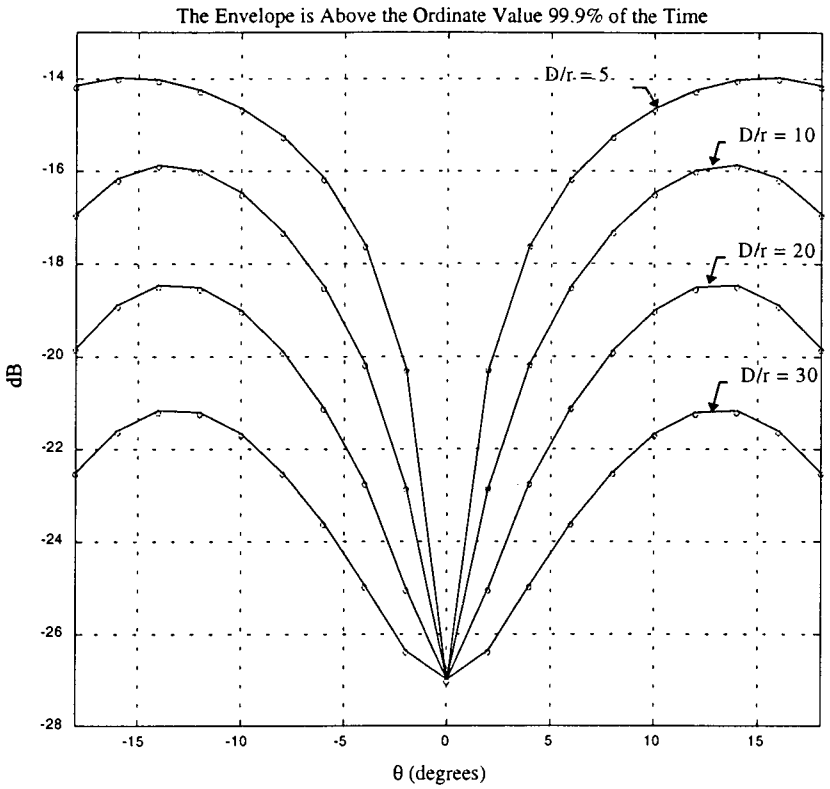

Figure 4.10 Envelope Improvement vs. θ for Several D/r Ratios

Unfortunately, the ratio D/r will be imposed by the environment which will ultimately determine the maximum achievable improvement. However, it is important to note that these results have been obtained using a linear array configuration composed of seven equally spaced elements with separation d=0.5λ, which results in a 3 dB beamwidth of 14.5°. This beamwidth plays a key role in the previous analysis and could be dynamically adjusted (diminished) to compensate for large values of D/r.

4.3 Fading on π/4-QDPSK Modulation

The analysis of Section 4.1 and Section 4.2 showed some of the advantages of utilizing a base station phased array antenna. So far, only the fading envelope has been taken into consideration, with all the simulations assuming the transmission of an unmodulated carrier. In this section the tracking algorithm and diversity techniques are implemented on a π/4-QDPSK receiver system. The simplified block diagram can be seen in Figure 4.11.

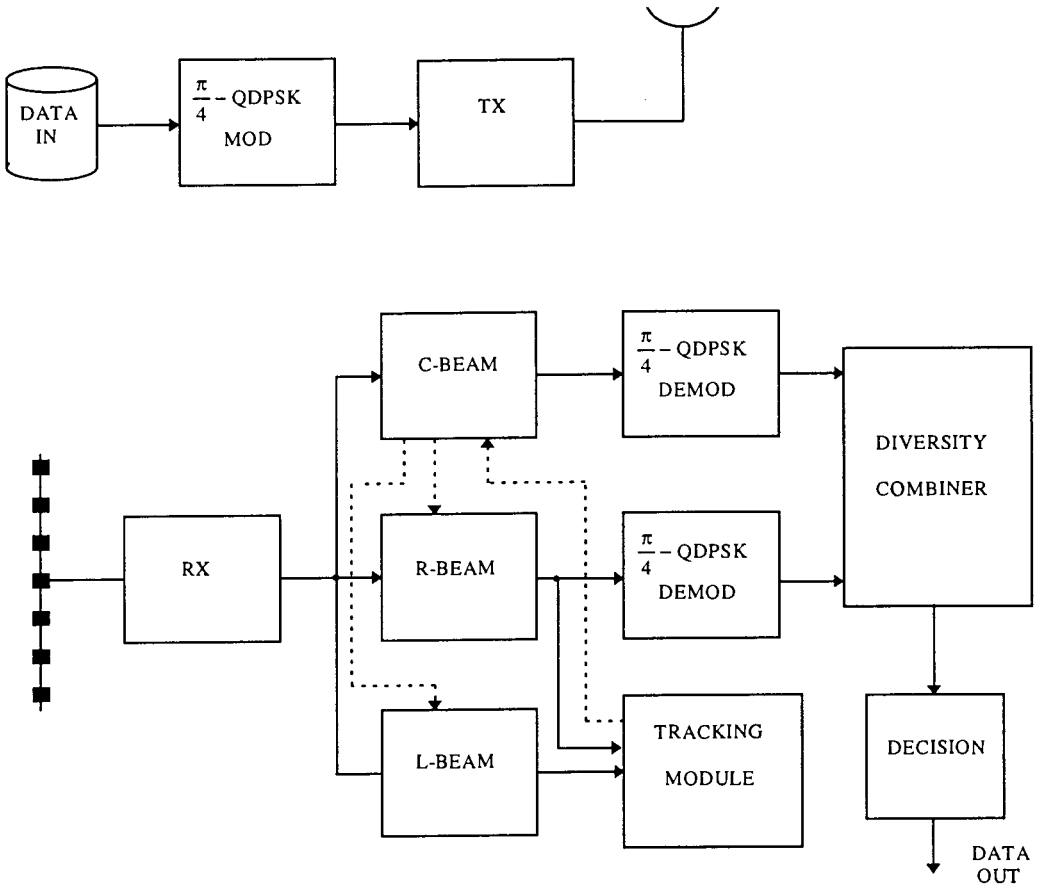

Figure 4.11 Receiver Block Diagram

At the mobile site the input data stream is modulated at 10kbit/s to form a $\pi/4$-QDPSK baseband signal. It is then upconverted to the carrier frequency, amplified and fed to the transmitting antenna. The multipath effect is simulated by passing the transmitted signal through the channel simulator developed in Section 3 which gives the seven baseband outputs corresponding to each one of the seven antenna elements. At a software level the RF transmitting and receiving stages can be seen to be part of the channel simulator module. Three blocks of phase shifters follow which will effectively form the beams shown in Figure 4.12.

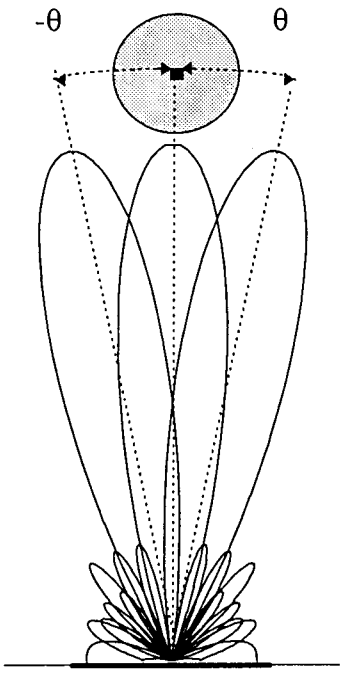

Figure 4.12 Tracking and Diversity Beams

Only the signals obtained from the R-beam and the C-beam are demodulated. The signal from the L-beam is exclusively used for tracking purposes. That is so because most of the computational complexity is inherent to the demodulation process. However, if the load requirements can be met, this signal could be used as a third diversity branch with very similar characteristics to the second one. The tracking module provides constantly updated information about the position of the mobile that is fed back to the phase shifters.

After demodulation the signals are combined using MRC and the final decision is made upon the result.

A square root raised cosine pulse in the frequency domain [6] was used as the pulse shape with a rolloff factor of 0.33. The pulse was truncated to 8 symbols length and Kaiser windowed with parameter 4. At the receiver the same pulse was used as the matched filter resulting in an overall Nyquist response. Figure 4.13 plots the simulated constellation of the received signal after the matched filter for the nonfading case. Note that the ideal sampling instants have been highlighted

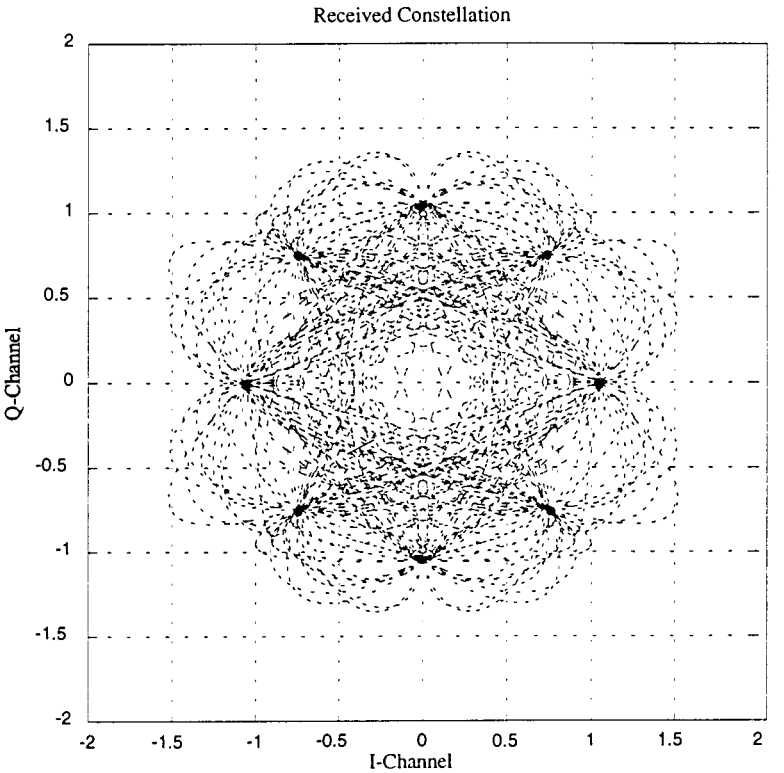

Figure 4.13 $\frac{\pi}{4}$-QDPSK Encoded Constellation

After differentially decoding, the constellation of Figure 4.14 a) is obtained. Rayleigh fading introduces a considerable amount of amplitude and phase distortion that can only be partially reduced by differentially encoding the transmitted signals, as in this case with

π/4-QDPSK. Its severe effect is most felt in the signal before differentially decoding which results in a highly cluttered and practically unrecognizable constellation. The aforementioned constellation is not plotted here because it lacks interest. Instead, the constellation after differentially decoding has been plotted in Figure 4.14 b. It can be seen that the phase remains for the most part unaffected, while the amplitude suffers severe degradation.

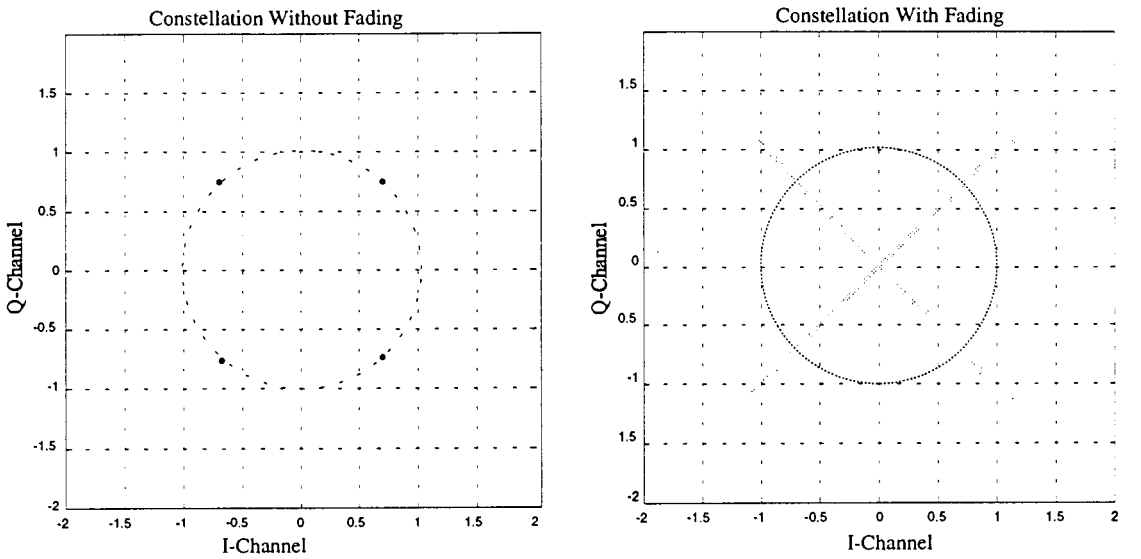

(a) (b)

Figure 4.14 Decoded Constellations:
a) Non-fading case
b) Fading case: fd=37 Hz

The parameters used for the channel simulator were those given in Section 3.2. As for the beamformers, the same phase shift needs to be used for both the tracking algorithm and diversity modules. From Figure 4.10, the maximum improvement that diversity can provide occurs when the phase shift equals approximately 14° for a wide range of values of the parameter D/r. After ensuring that the tracking algorithm does not suffer from this change (the value previously used had been 10°) the value adopted for the phase shifters was θ=14°. It is interesting to note that 14.5° is precisely the beamwidth of the array.

A Gaussian noise source was subsequently simulated and added to the system in order to obtain the bit error rate (BER) as a function of the signal to noise ratio. The simulations used a set of 50,000 symbols (100,000 bits) which translate into 10 seconds at the present transmission rate. Those 10 seconds should allow for a very complete portrayal of the fading envelope and its effects on the modulation scheme under study, as well as providing a minimum detectable BER of 10^{-5}. Two values were measured at every run: the BER of the global system as designed and that of a system whose decision was made based on the output of the C-beam and its corresponding demodulator alone, that is, without any diversity improvement.

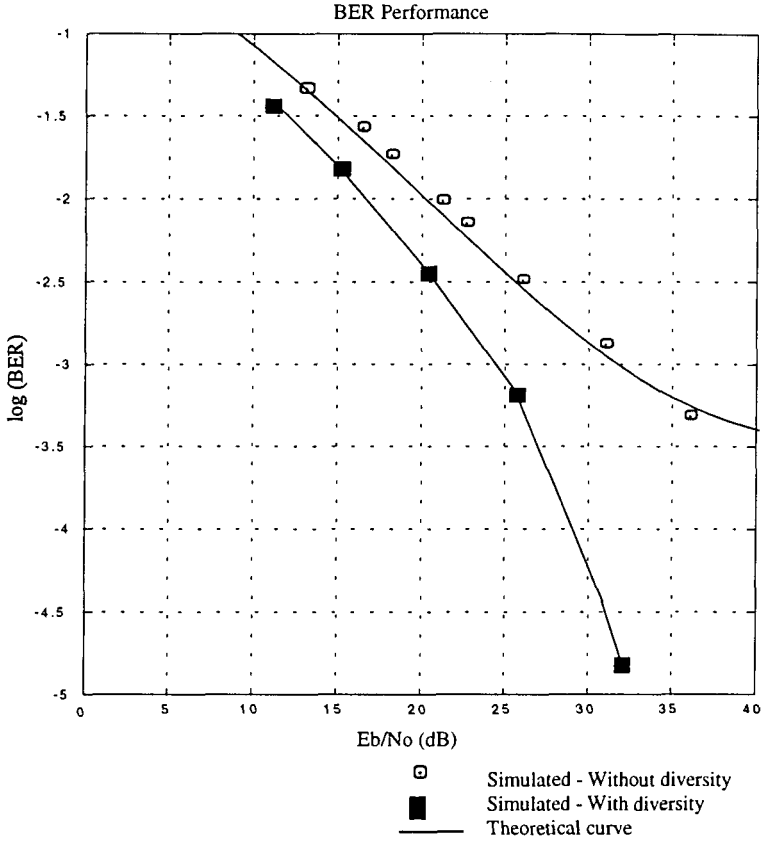

Figure 4.15 BER With and Without Diversity

The results are plotted in Figure 4.15, where the solid upper trace is the theoretical BER curve for QDPSK. The agreement with the simulated data is quite remarkable and proves

that the overall model is a valid one. The lower trace is the one of interest as it shows how the improvement in the quality of the fading envelope seen in Section 4.2 effectively translates into a decrease of the BER, which is the ultimate goal of a digital communications system designer. As expected, for low signal to noise ratios little improvement is achieved since the diversity branch, being 6.27 dB weaker than the main one (see Table 4.1), is very noisy itself. As Eb/No increases, the effect of the diversity branch turns more and more evident until the improvement becomes quite dramatic for values of Eb/No greater than 25 dB. For the simulated fading rate of 37 Hz the theoretical limit of the BER that can be achieved is close to $3 \cdot 10^{-4}$ for values of Eb/No over 40 dB. By using the described diversity technique the same performance is attained with Eb/No equal to only 27 dB, and is rapidly surpassed with little increment of the Eb/No. As a reference, the reduction of the Eb/No necessary to achieve a BER of 10^{-3} is about 8 dB.

The next two figures are intended to provide a clearer understanding of the error correcting process. The constellations of the signals with and without diversity are plotted in logarithmic scale, the center of the polar plots in both cases being -30 dB. Figure 4.16 a) shows the signal without diversity for a Eb/No of 27 dB. There are several data points very close to the center of the plot and, consequently, very sensitive to noise. In fact most of them have probably already been corrupted by noise and appear in the wrong quadrant, which will lead to decision errors. On the other hand, Figure 4.16 b) shows the result of combining the two diversity branches. The central region now appears much less cluttered and most likely will not produce any errors.

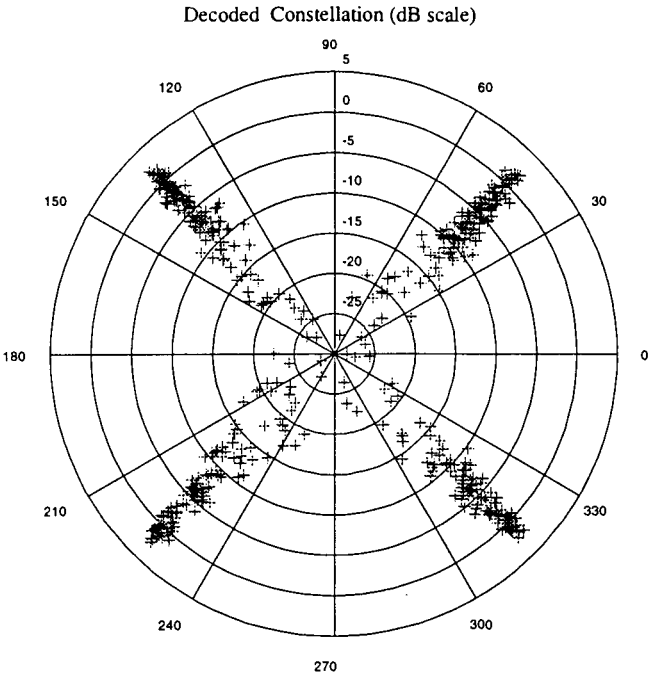

(a)

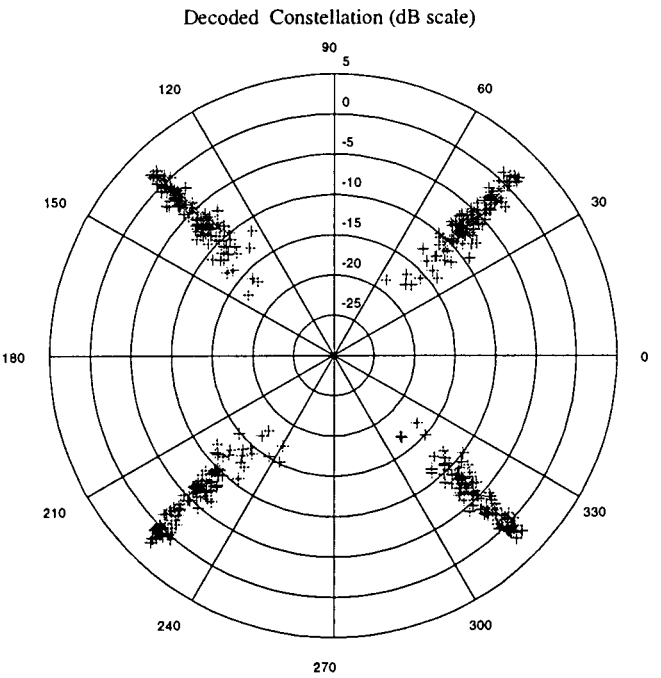

(b)

Figure 4.16 Decoded Constellations:
a) Without Diversity
b) With Diversity

5. FIELD TESTS

5.1 Hardware Components and Test Setup

This section provides a brief description of the hardware involved in the design of the phased array antenna system, as well as the equipment used to test its performance in a real mobile environment.

5.1.1 Transmitter

The transmitting system was assembled using entirely existing, general purpose equipment. The baseband signal was generated with the aid of a TMS320C25 DSP board, equipped with two DACs. The I and Q samples were output at a rate of 40 k samples per second, low pass filtered to create the analog signal and directly upconverted to the carrier frequency of 815 MHz. An HP8657A signal synthesizer was used to provide a very stable LO for the quadrature modulator. Its output was fed to a 3W Mini Circuits power amplifier which was backed off to 1.5 W to avoid excessive spurious levels. The block diagram can be seen in Figure 5.1.

The assembly code running on the DSP processor was the only part of the transmitter specifically designed for use in this project. Three separate tests were performed, each one requiring its own software. They will be seen in greater detail in following sections. In addition, an existing C program was run under DOS to provide a user interface with the DSP board. This feature allowed the user to compensate for unwanted DC components that are present in the in-phase and in-quadrature branches, as well as for gain and phase imbalances between them, that result in fairly large levels of carrier and image frequency at the output of the QUAD MOD. They were both successfully kept under at least -30 dBc at all times.

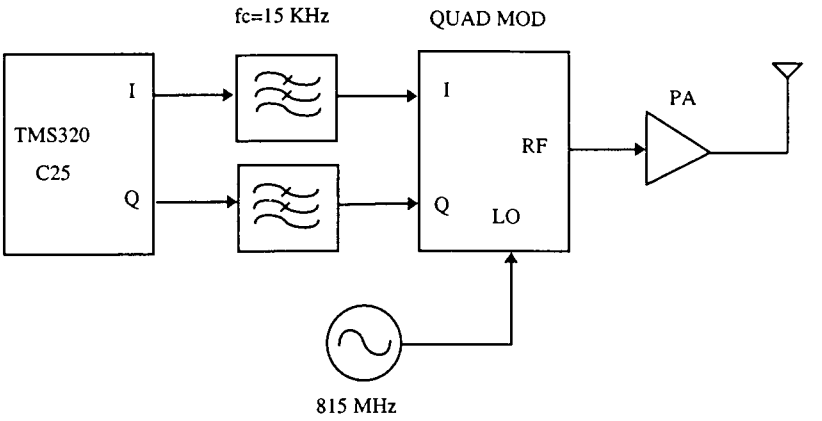

Figure 5.1 Transmitter Block Diagram

5.1.2 Receiver

The receiver was entirely built and tailored for this specific project in the Engineering Science Department at Simon Fraser University. It consists of the antenna array itself plus seven identical receivers, one per antenna element.

The base station antenna was a seven element array made up of omnidirectional microstrip patches. The spacing between elements was half a wavelength. The block diagram of one of the receivers can be seen in Figure 5.2. The signal impinging in one of the antenna elements is fed to the front end. It is subsequently filtered at RF and passed through a low noise amplifier before reaching the two downconversion stages. Finally, the signal is presented to the QUAD DEMOD at the second IF frequency of 455 KHz, which will take it down to complex baseband. Two HP8657A signal synthesizers, identical to the one used in the transmitter, were utilized to provide the two first local oscillators at 815 MHz and 44.545 MHz respectively. The third one was a Marconi 2022 signal generator, operating at 910 KHz, twice the second IF frequency, due to QUAD

MOD requirements. The sensitivity of the receivers was -80 dBm for a 10 KHz bandwidth, resulting in an overall dynamic range of 60 dB.

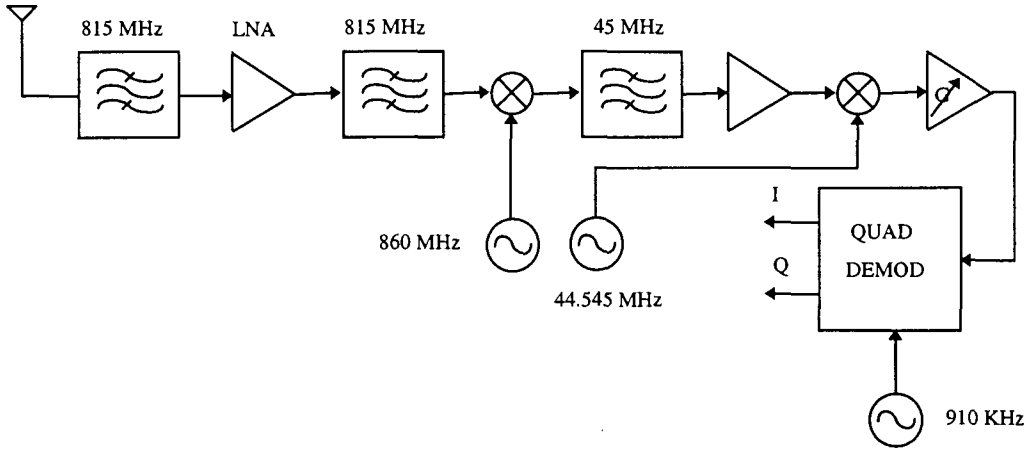

Figure 5.2 Receiver Block Diagram

5.1.3 Data Storage

Gathering a substantial amount of data from a mobile environment posed the problem of storage. The receiver provides seven complex baseband signals, which means 14 analog channels. They had to be digitized and stored for later analysis. The solution adopted was to use a professional Alesis ADAT 16 track recorder to store the information in analog format during the field tests. A 5 kHz synchronization sine wave was recorded on one of the remaining tracks, to be used as a reference when digitizing the channels at a later time.

A PC equipped with a TMS320C25 board was used to digitize the information.. A 20 KHz signal that was phase locked to the recorded sync, provided the sample clock to the ADC on the processor board. A very simple C program running on the PC waited for this value to be stable, read it from a common memory mapped register and wrote it to an

external 1.8 Gb SCSI drive. Several additional timing information marks were periodically inserted to ensure a proper channel alignment. The data on the SCSI drive was then written to a CD, erased and used again to store some more data.

5.1.4 Tests Location

The base station antenna array was located on the roof of the Glenayre Electronics R&D facility in Vancouver, BC. The tests were performed in what could be described a suburban, residential area, with alternate heavy shadowing zones and relatively open spaces. The prevailing structures were one or two stories, wooden houses. Figure 5.3 shows the geographical disposition of both transmitter and receiver, where Glenayre is located at (0,0). It can be seen that the vehicle trajectory was confined to a 30 degree angular sector relative to the antenna array front.

5.1.5 Tests description

Three different tests were performed:

- 5 KHz Complex Tone, widely covered in the following Section.
- $\pi/4$-QDPSK Data , reported in Section 5.3.
- 8 Complex Tones, as shown in Figure 5.4.

The utility of the third test was to characterize each of the individual receivers at a set of discrete frequencies over their bandwidth. They were disposed in that particular fashion so that the image frequencies generated by the QUAD MOD and the desired tones would not overlap.

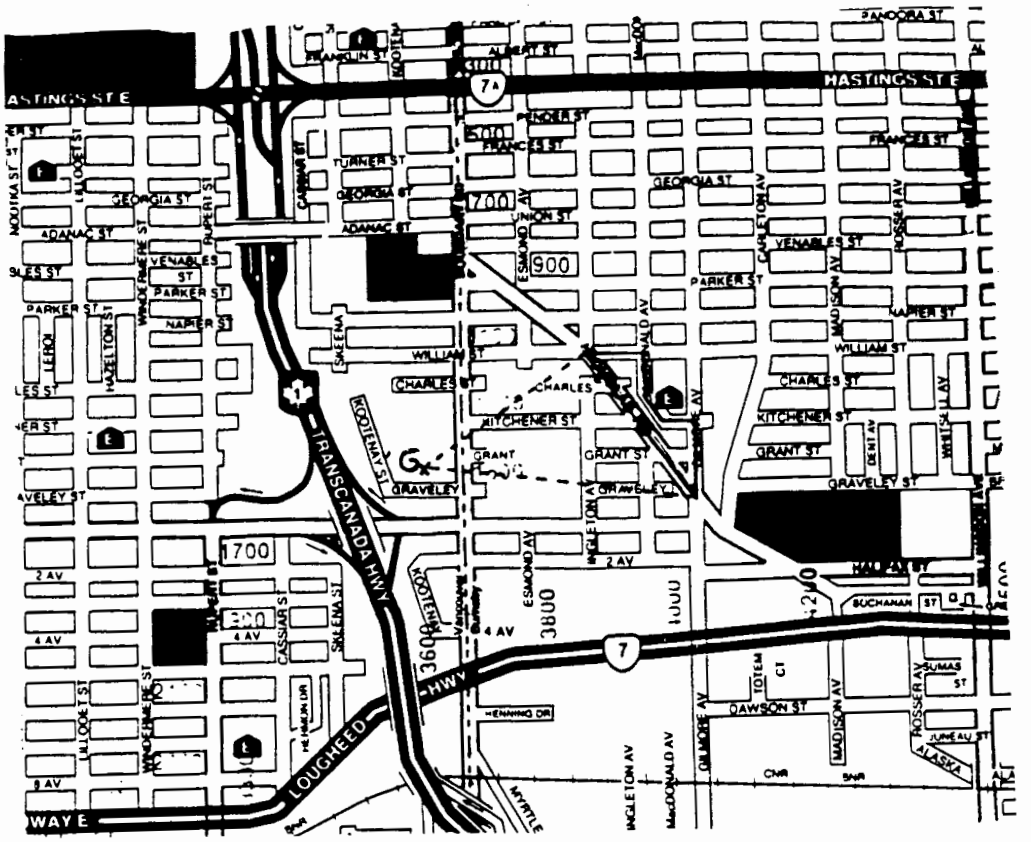

(a) Area Street Map

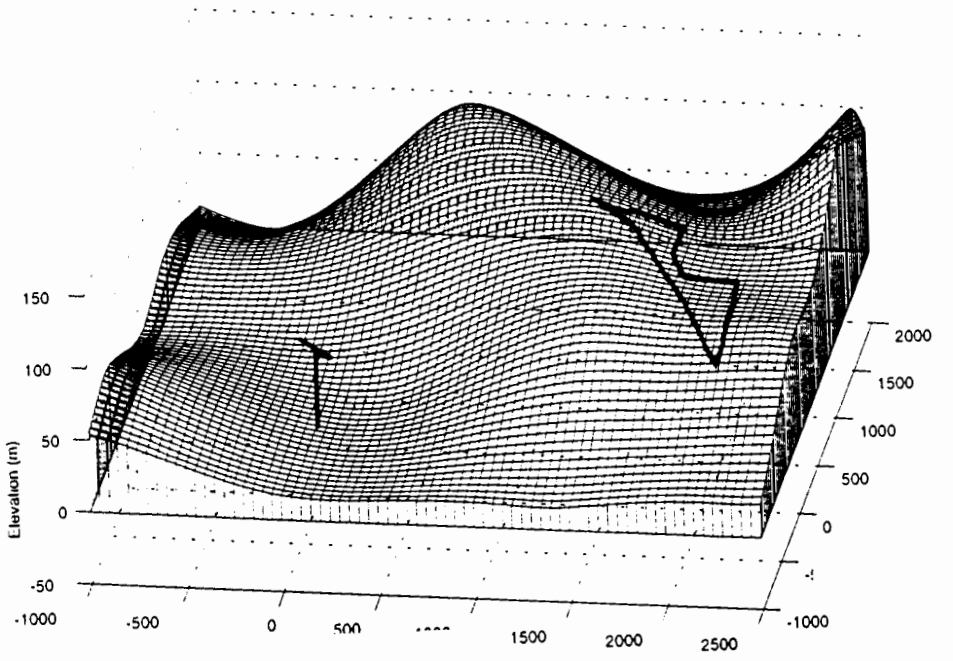

(b) Area Contour Map

Figure 5.3 Tests Location

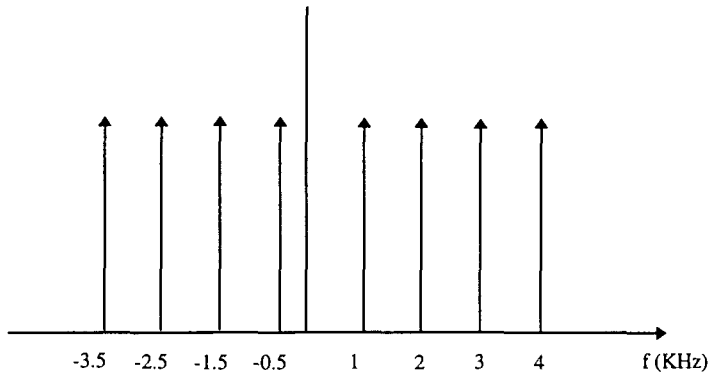

Figure 5.4 Transmitted Complex Tones

The calibration was performed based on stationary data recorded at location 1 [Figure 5.3]. The magnitude and phase of the transfer functions were obtained at the chosen frequencies and extended to the whole band by interpolation. This particular method takes into account the effect of the antenna elements and their feeds as well as the receiver itself and was chosen over the calibration in the lab approach. The main difficulty was trying to separate the contribution of the receiving system to the phase from that of the angle of arrival. The solution adopted was simply to cophase the signals thus redefining boresight as the present direction of arrival of the incoming wave. As a result, seven equalizer filters were obtained to be used with the digitally modulated data. As far as the complex tone test goes, since only one frequency is involved, the set of equalizers can be replaced by a set of initial complex weights, as will be seen in the next section.

5.2 Complex Tone Test

The complex tone measurements were clearly the most essential part of the field tests as far as this thesis was concerned. Their main purpose was to determine whether or not the developed algorithms for tracking and diversity would be operational in a real fading environment, and if so, how close their performance would be to that given by the simulations. At the same time, successful results would indicate the validity of the Rayleigh fading simulator developed in Section 3 and its suitability for use with in-lab system developing and testing. A complex tone has a constant envelope and a known phase, which allows us to extract the fading parameters introduced by the environment. In order to calibrate the receiving system the initial 30 seconds were recorded while the transmitting vehicle was stationary and in direct line of sight with the receiving antenna, at location 1. The following is a brief description of the postprocessing applied to the raw recorded data during that time interval. The transmitted tone was at 5 KHz.

The recorded envelope presents a very distinct ripple that was found to be caused by the image frequency. The quadrature modulator and power amplifier at the transmitter are greatly responsible for this effect. Despite being about 25 dB lower than the main tone it highly degrades the appearance of the envelope and needs to be removed. In addition, a dc level due to some local oscillator feedthrough of a similar power level is also present and contributes to the forementioned ripple. Instead of using a complex filter to remove the unwanted components a more convenient approach was taken. The original signal was downconverted to baseband (multiplied by $e^{-j2\pi 5000t}$) and low pass filtered. The usefulness of this technique lies in the fact that when the vehicle is moving the fading envelope will be presented at baseband as opposed to modulating a 5 kHz tone. Therefore it can be resampled at a much lower frequency than the original 20khz without losing any relevant information.

Since the vehicle was stationary at this point, the outcome of the previous process should have been a dc component. Unfortunately that was not the case. It was found that a

defective cable on the transmitter made the local oscillator lose its phase reference effectively causing the transmitted tone to be centered at 5 KHz $+\Delta f_o(t)$, where $\Delta f_o(t)$ is a time varying frequency offset term. Its maximum value was found to be around 150 Hz. The expression of the signal received by the i^{th} antenna elements is:

$$s_i(t) = a_i e^{j(\varpi_o(t)\, t + \phi_i)} = a_i e^{j\varphi_i(t)} \quad ; \quad i=1, 2, ..7 \tag{5.1}$$

where a_i and ϕ_i include the contributions of both the transmission medium and the receiver. The effect of the frequency offset is negligible for the purposes of these tests since every antenna element is affected in the exact same way and therefore can always be factored out. Thus, the envelope remains unaffected and only the phase measurements had to be discarded.

The last step to be taken was that of compensating the individual signals for differences in power levels and phases introduced by the receivers themselves. The bank of equalizers described in Section 5.1.5 could have been used for this purpose, but since only one complex weight per branch is needed in this test, a different approach was taken. The amplitude mismatches were easily solved by normalizing them all to the first element and then the signals were all cophased. By doing so, a set of initial weights was obtained that has the effect of steering a beam towards the vehicle. The weights were calculated as follows: from Equation (5.1),

$$\Delta\varphi_i = \varphi_1(t) - \varphi_i(t) = \phi_1 - \phi_i \quad ; \quad \alpha_i = \frac{a_1}{a_i} \quad ; \quad i=1, 2, ..7 \tag{5.2}$$

the initial weights w_{oi} can be written as:

$$w_{oi} = \alpha_i e^{j\Delta\varphi_i} \quad ; \quad i=1, 2, ..7 \tag{5.3}$$

These weights are to be used at all times as a correction factor right at the output of the quadrature demodulators.

The technique described in Section 3, Equation (3.29), is used again to obtain the space factor of the antenna array at a particular instant in time. In this case, the set of

weights w_{ik} is applied after the initial correcting set. The resulting plot can be seen in Figure 5.5, where the dashed trace is the theoretical curve.

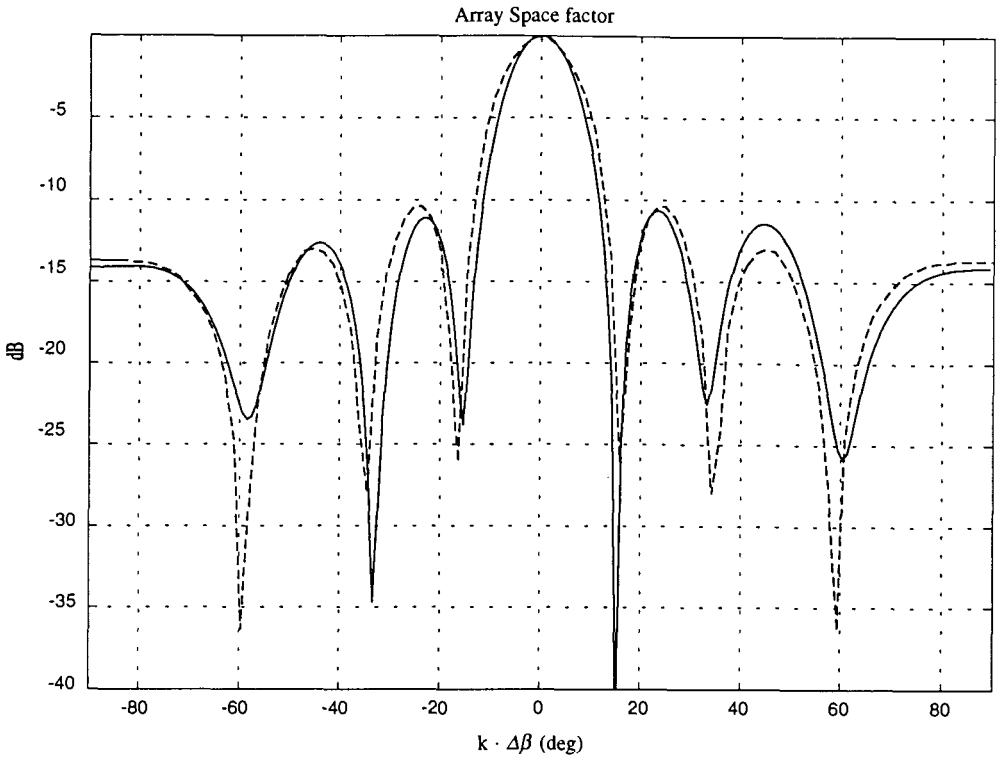

Figure 5.5 Measured Array Pattern

Although the measured pattern seems to follow the theoretical one very closely, this is not always the case. The correlation between adjacent array elements is suspected to have been affected by the presence of local scatterers around the base station. Its value fluctuates with time, and eventually drops to very low level. It is unclear how this will affect the performance of the antenna array on average.

At this point the system has been perfectly tuned up and the data recorded with the vehicle in motion can be analyzed. First, the frequency spectrum was obtained. Despite the driver's best attempts to keep a fairly constant velocity ,that was hardly ever the case, and the spectrum was found to be highly time dependent, leading to all kinds of different shapes depending on the observation period. Two of those have been randomly chosen

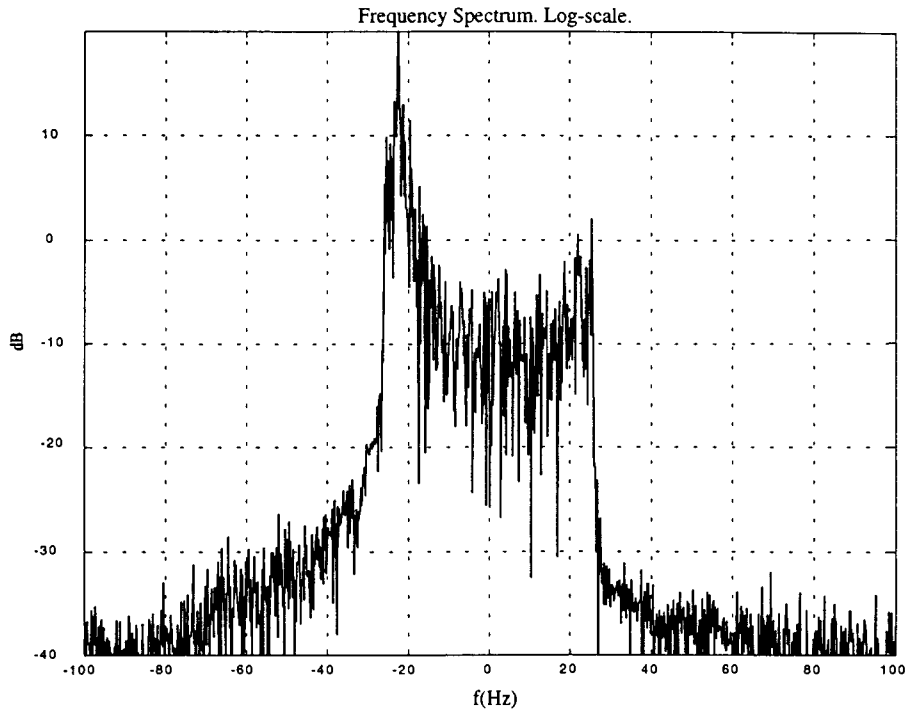

(a)

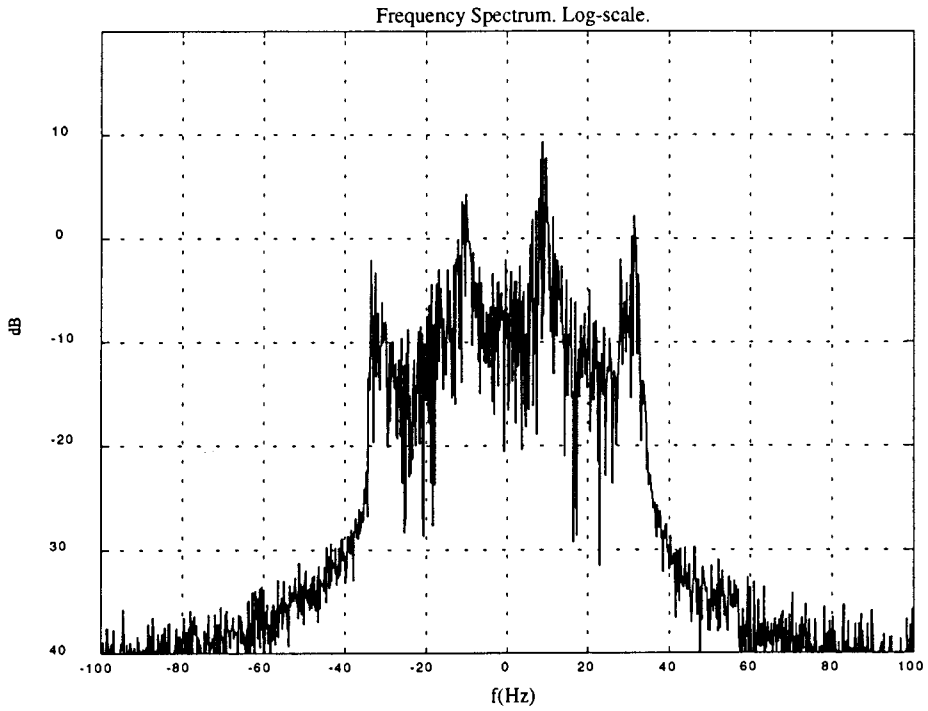

(b)

Figure 5.6 Measured Signal Spectrum

and are plotted in Figures 5.6 (a) and (b). The observation period was 3 seconds. Both figures illustrate vague traces of the typical U-shape that is expected. In the first case the maximum Doppler frequency is around 25 Hz, which would translate into a traveling velocity of 33 km/h. The second figure illustrates an interesting phenomena that could be interpreted as having the vehicle abruptly change its velocity from approximately 43 km/h down to 13 km/h, or viceversa.

Next, the fading envelope was analyzed. One additional effect that has not been considered throughout this thesis is the long term or log-normal fading, mainly caused by large scale obstacles in the propagation path. It had to be removed from the original received signal in order to obtain the statistics of the Rayleigh envelope. The procedure adopted is described in [3] and consists of taking the moving average of the original envelope with the proper choice of the averaging interval. Figure 5.7 illustrates the process. The log-normal fading in (b) can be seen to change very slowly compared to the Rayleigh fading, but the variation can be rather large.

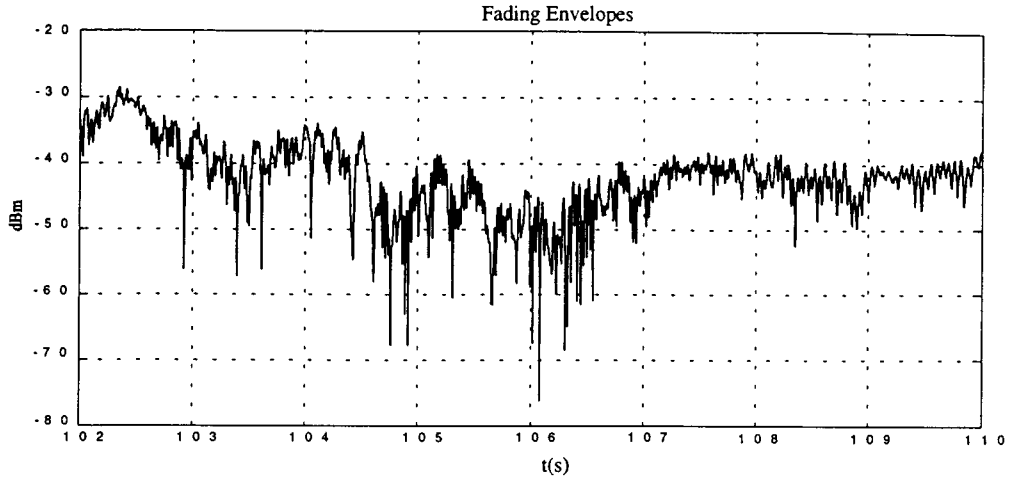

(a) Recorded Envelope

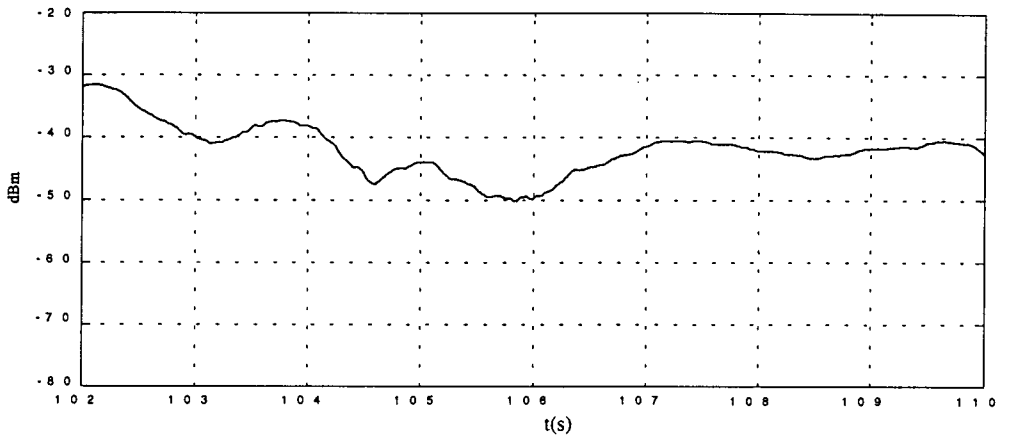

(b) Log-normal Fading Component

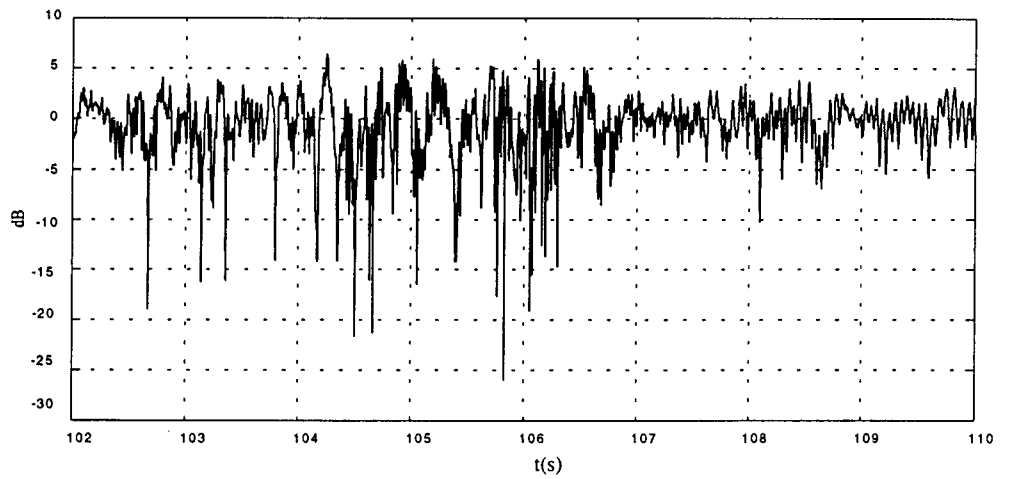

(c) Rayleigh Fading Component

Figure 5.7 Sample of the Recorded Fading Envelope

Again, the non constant velocity caused a great deal of distortion and the measured statistics, in general, had little resemblance to those expected from a Rayleigh process, even after the log-normal fading had been removed. It is also very possible that a strong, direct wave could have reached the receiver from some of the locations where the tests were performed, causing the envelope to fade with a Ricean PDF instead. The statistics were computed again, this time over the same observation period used to obtain Figure 5.6 (a), hoping that the assumption of nearly constant velocity would be accurate. The signal level over this period was relatively small, which almost certainly indicates that there was no direct wave being received. In this case the results clearly show the probability density function and cumulative distribution of a Rayleigh process, as can be seen in Figures 5.8 to 5.10.

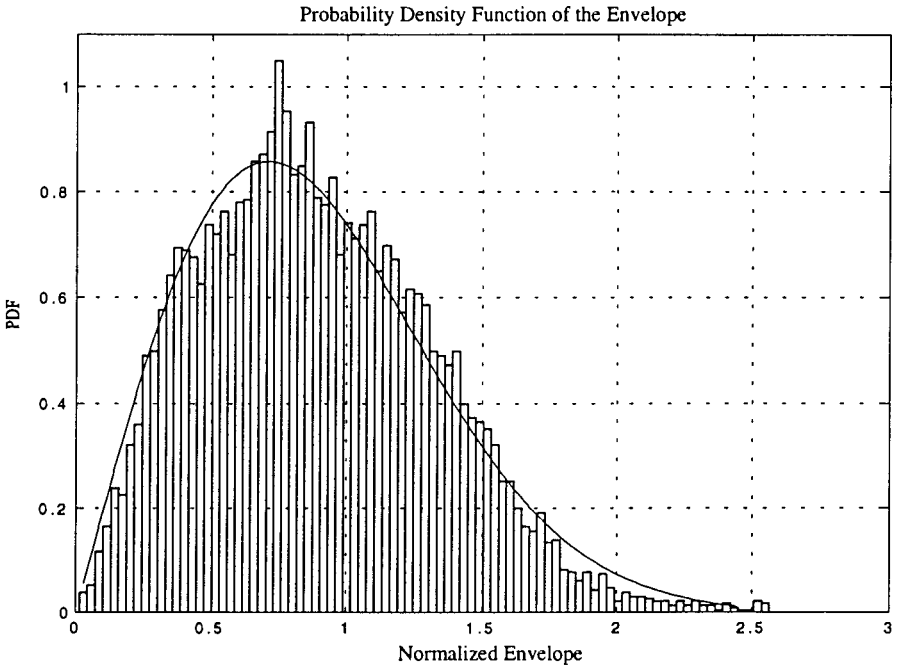

Figure 5.8 Measured Envelope Distribution

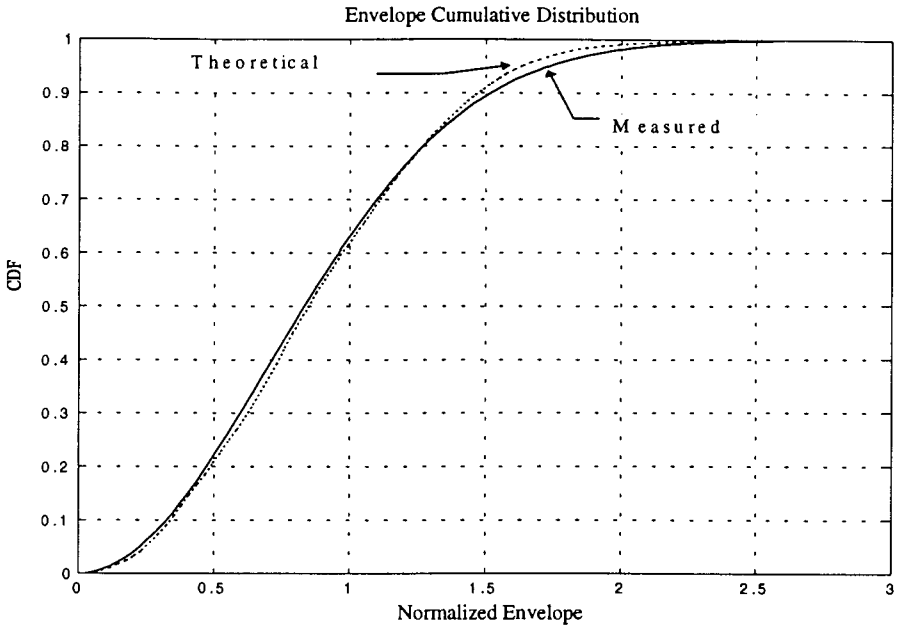

Figure 5.9 Measured Envelope Cumulative Distribution

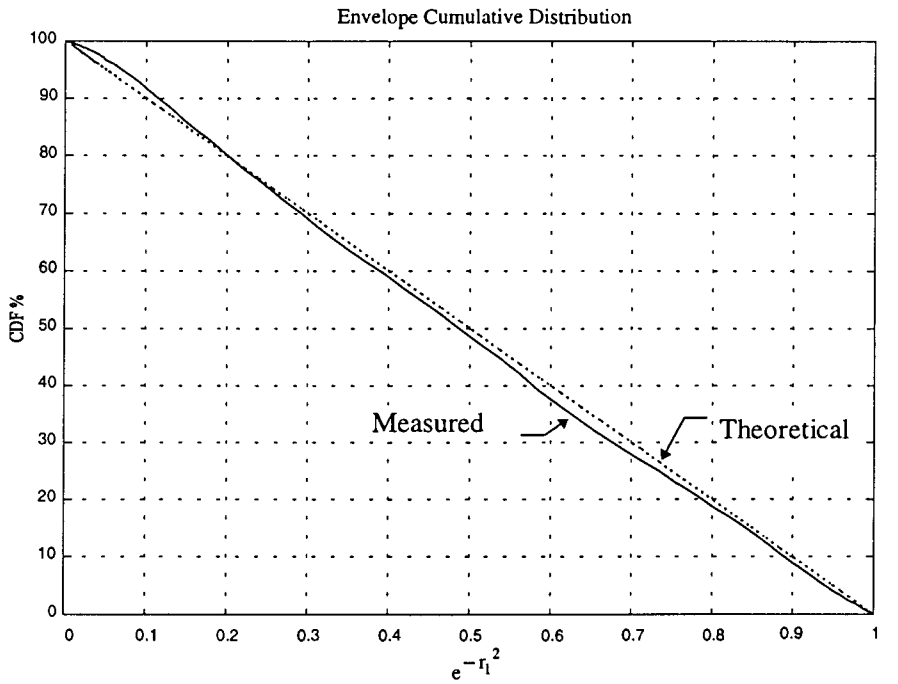

Figure 5.10 Measured Envelope Cumulative Distribution. Linear Form

5.2.1 Tracking

The results of section 5.2 showed that the reception of a complex tone transmitted from a mobile unit can be enhanced by the use of a seven element antenna array. The impinging signals are directionally combined to provide as much as 8.45 dB gain compared to the single antenna reception case. The only requirement for this system to be operational is that the position of the mobile unit be known so that the array's main lobe can always be pointing at it. The algorithm developed in Section 4.1 will be tested once again, this time in the real fading environment, and it will be seen if its apparent robustness still holds. Before that, the position of the transmitter will be determined using a very exhaustive searching algorithm. Its computational complexity would make its real time implementation prohibitive, but it can be used in this context by applying it to the recorded data. The search algorithm is based on a similar principle as Equation (3.29).

Let us define:

f_s = sampling frequency

$\Delta\theta$ = desired angle resolution in degrees

T = averaging period, approximately equal to 40 wavelengths, as discussed in Section 4.1

The array scans 360 ° in steps of $\Delta\theta$, resulting in M observation angles, with $M = 360/\Delta\theta$. This process is repeated for every sample up to N samples, with $N = f_s T$, and a M×N matrix is formed whose columns are observation angles and whose rows are observation instants. The columns are then averaged to obtain an estimate of the average signal power received at every observation angle during the interval T. The process is coarsely illustrated in Figure 5.11. The algorithm then selects the position of maximum received power by comparing the terms P_{iN} , i=1..M.

	$-180°$	$-180°+\Delta\theta$	$-180°+2\Delta\theta$	. . . .	$180°-2\Delta\theta$	$180°-\Delta\theta$	$180°$
t_o	p_{11}	p_{21}	p_{31}	. .	p_{M-21}	p_{M-11}	p_{M1}
$t_o + 1/f_s$	p_{12}			. . .			
$t_o + 2/f_s$	p_{13}			. . .			
⋮	⋮	⋮	⋮	. . .	⋮	⋮	⋮
$t_o + T$	p_{1N}	p_{2N}	p_{3N}	. . .			p_{MN}
Average	P_{1N}	P_{2N}	P_{3N}	. . .			P_{MN}

Figure 5.11 Location Retrieval Matrix

The whole process is periodically repeated every T seconds and a vector of transmitter locations is formed. The result for a 110 second period of time, with T=1 second and 0.1° angle resolution, is illustrated in Figure 5.12.

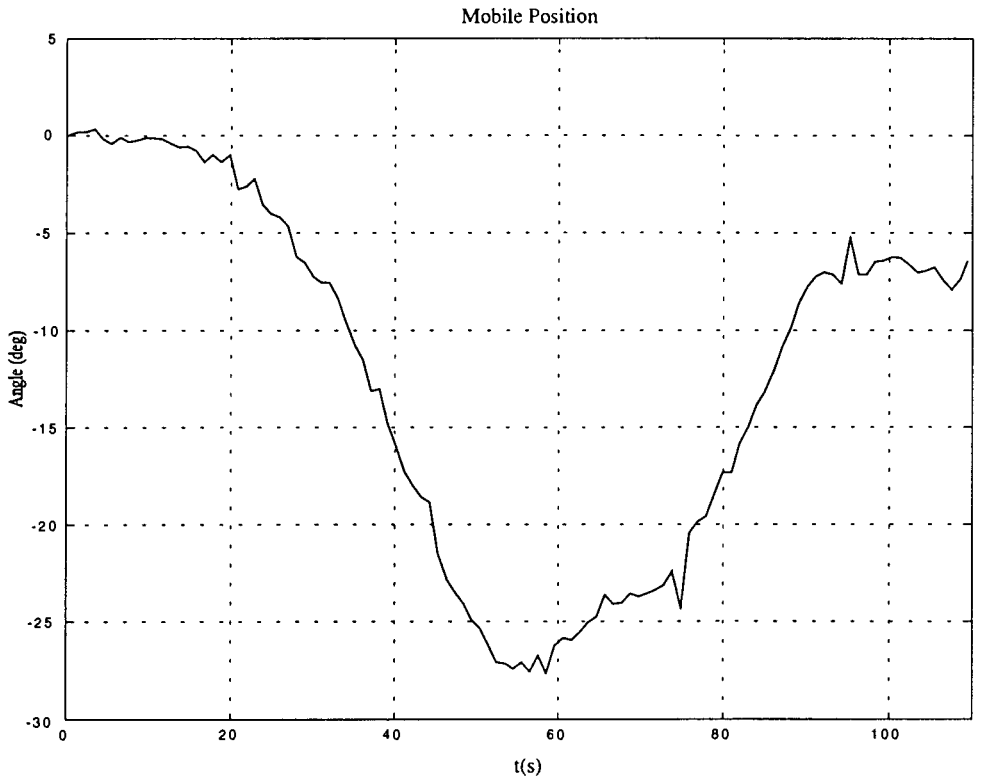

Figure 5.12 Mobile Retrieved Position

The mobile unit is shown to have started its motion at boresight, traveling East, and reached as far as 27 ° from its original position. According to Figure 5.12 the car must have been at location 1 (Figure 5.3) when the stationary tests were performed.

Finally the algorithm was tested with the parameters $\Delta\beta=14°$ and T=1 second for the period of time under consideration. The result is surprisingly accurate, as Figure 5.13 shows, especially taking into account the difference in algorithm complexity.

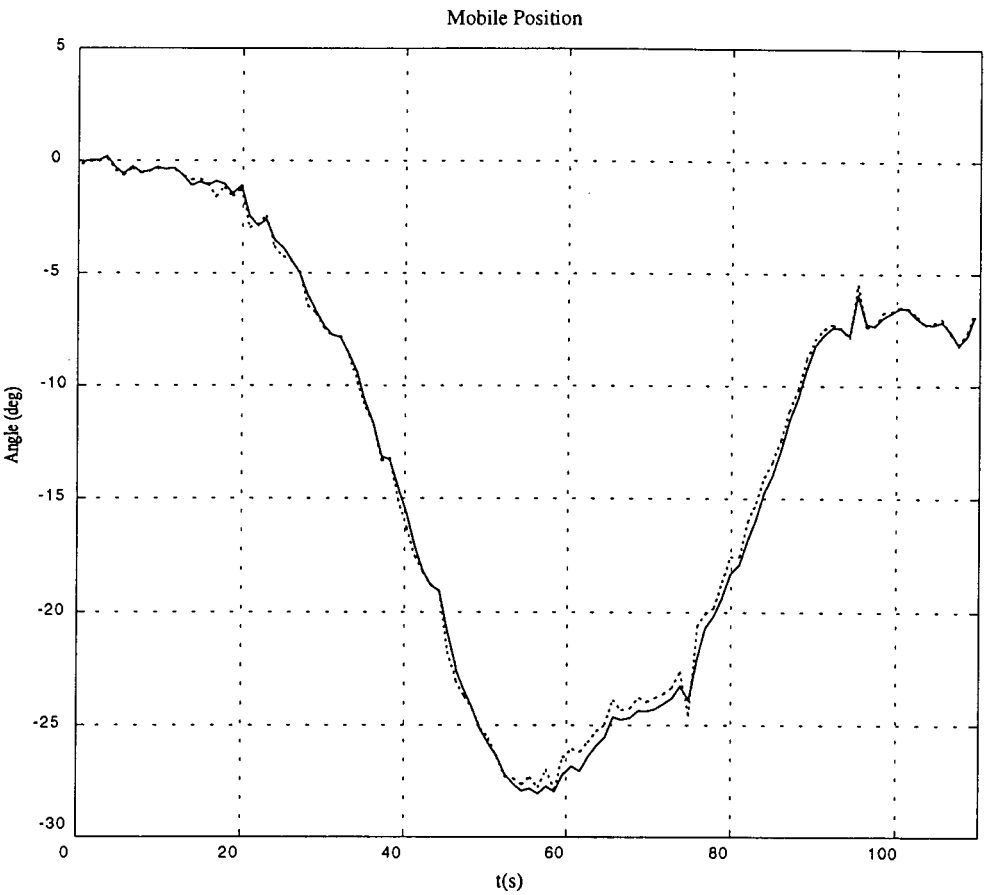

Figure 5.13 Tracking Algorithm Performance

5.2.2 Angle Diversity

It has been shown in Section 5.2.1 that the tracking module in Figure 4.11 can be successfully implemented with very little complexity. This section attempts to recreate the diversity results obtained in Section 4.2.

In this case the vehicle location is retrieved by the tracking algorithm, rather than being externally fed to it. The C-beam will be pointing at the vehicle at all times, while the R-beam is, again, shifted by θ degrees. The signals are analyzed as in Section 4.2 and, rather than presenting the results in a numerical fashion, they will be directly plotted in the format used in Figure 4.10. The main discrepancy from the predicted behaviour was found to be the unexpected dependence of both the correlation coefficients ρ_{12} and the average powers ratio P_2/P_1 (Table 4.1) with time for relatively large angle separations. One possible explanation could be the difference in shadowing suffered by the two received signals as large obstacles in the main path are somewhat avoided in the diversity branch. That would also account for additional local differences in the average power, which are overlooked in the model by not taking the log-normal fading into consideration. In addition, the presence of local scatterers near the base station could add up to that effect, even though their existence has not been entirely demonstrated. As previously stated, this effect is only noticeable for fairly large angular separations, in the range $\theta \geq 10°$.

The results presented in this Section are based on average values for both the correlation coefficients and the average power ratio over a 110 second window. Keeping the previous discussion in mind, they can be assumed to be accurate and general for $\theta \leq 10°$. Outside that range, they should be seen as an average performance that is very much location dependent. Figure 5.14 illustrates the level that the envelope of the combined signal is greater than, with probability 99.9%, as a function of the separation angle of the diversity branches θ.

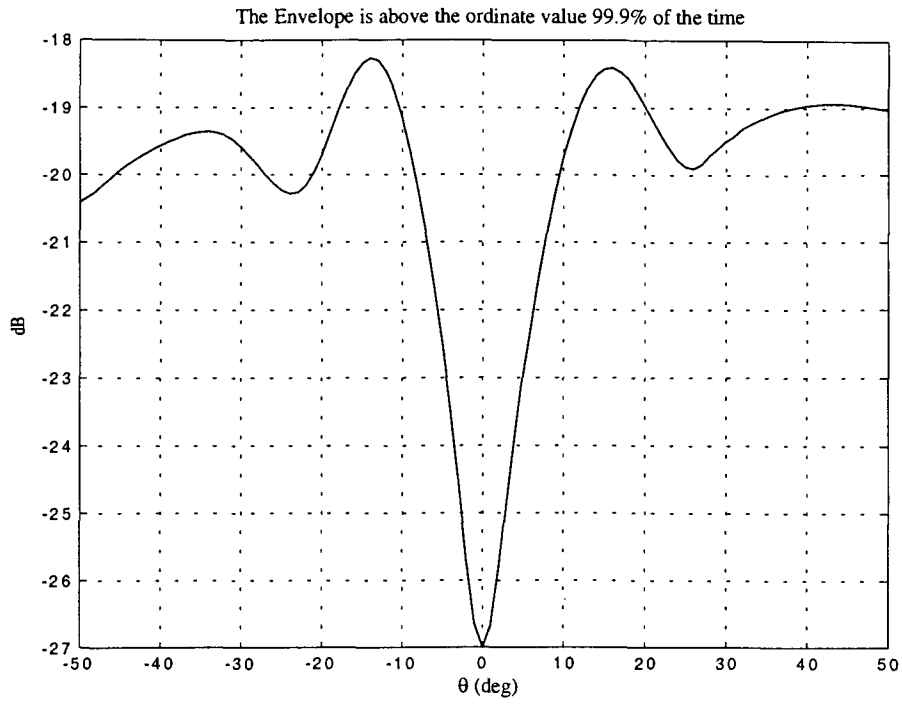

Figure 5.14 Measured Envelope Improvement

At first sight there are a number of interesting properties that can be singled out:

- Angle diversity is actually achieved.
- The overall behaviour is remarkably close to the predicted one; a fast rising towards the optimal point followed by some progressive, oscillating decay.
- Almost a 10 dB improvement at the optimal point, which is indeed very close to 14°.
- Uneven behaviour about 0°, mainly due to differences in correlation coefficients. One fairly reasonable explanation is that the real world is not made up of perfect circles. The particular geography surrounding the test area is held responsible, particularly for large values of the angle θ. Also note that the vehicle position was assumed to be that given by the tracking module. By inspection of Figure 5.13 it can be seen that for the second part of the run, from t=50s to t=90s, the retrieved position angle is always slightly smaller (more negative) than the real one. The signal received by the C-beam would remain virtually unaffected, since the error is always less than 1°, but it could significantly modify the ratio P_2/P_3 for some values of θ. Since the position of the

transmitter was decided based upon this ratio, the relationship $P_2=P_3$ should still hold for $\theta=14°$. Closer inspection of Figure 5.14 reveals that the difference between ordinates for $\theta=14°$ and $\theta=-14°$ is only 0.2 dB, which can be entirely attributed to different correlation coefficients.

Figure 5.15 shows a close-up of the obtained curve in relation to the simulated ones for the different values of the parameter D/r obtained in Section 4.2.

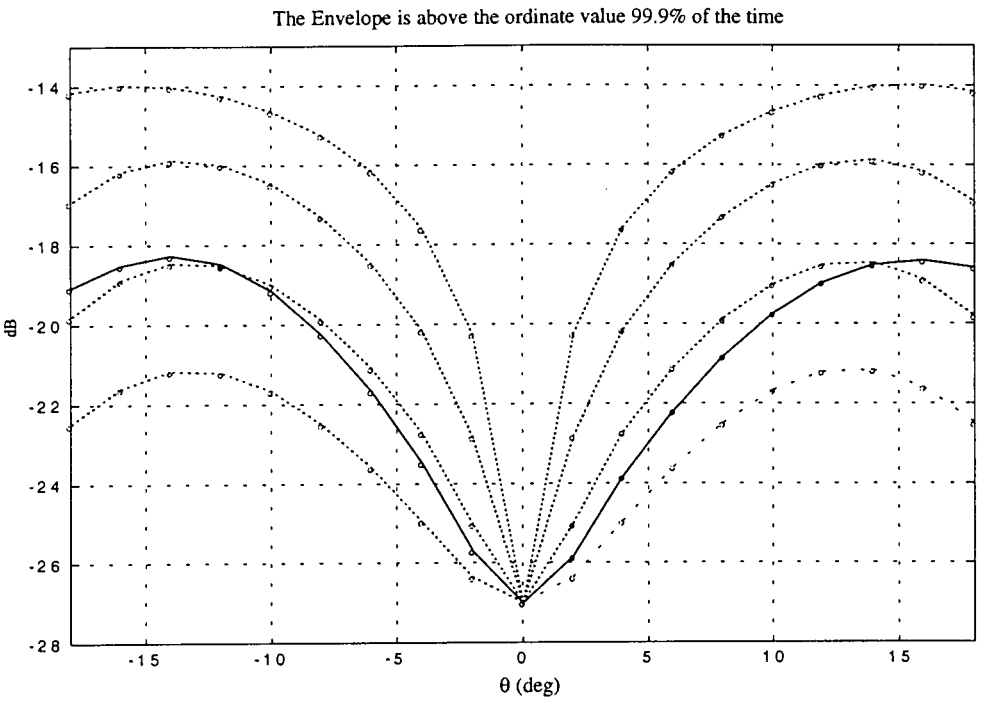

Figure 5.15 Measured vs. Theoretical Improvement

The curve corresponding to negative values of θ seems to agree very closely with the simulated curve for D/r=20, whereas for positive angles and $\theta \leq 10°$ the match would almost be exact for a D/r ratio of 23. As a compromise, the ratio is taken to be D/r=22. For an average distance D=1.2 Km, the radius of scatterers turns out to be r=55m which would translate into a delay spread of 13 ns for the test area.

5.3 π/4-QDPSK Data Test

The final test consisted of transmitting a digitally modulated signal over a 10 kbit/s mobile channel. At this transmission rate, the assumption of frequency nonselective fading seems to be appropriate, according to the estimated delay spread from the previous section. It would only mean 0.0065 % of the symbol period, and therefore can be totally neglected. As in Section 4.3, the improvement achieved by the use of the base station antenna system will be the focus of the present discussion. QDPSK was chosen as the signaling scheme since the receiver does not require an estimate of the channel phase and it performs only 3 dB worse than coherent QPSK.

5.3.1 π/4-QDPSK Modulator

The assembly code for the π/4-QDPSK modulator was specifically written for this project and implemented on a TMS320C25 DSP processor from Texas Instruments. It uses the same set of parameters used in the simulations of Section 4.3. A sequence of 4096 predefined symbols is constantly transmitted. The last 8 incoming symbols form a code word that maps to a lookup table, an area in memory where the precomputed samples for the given sequence are stored. There are 5 possible values for each of the channels, which would translate into 5^8 combinations for the code word. This number was greatly reduced by noting that not all the combinations are allowed. Let us take the I channel as an example. At any given time it can take any of the values {-1,0,+1} or $\{-\sqrt{2}/2, +\sqrt{2}/2\}$. If the value is taken from the first subset, in the next symbol period it will correspond to the second subset and viceversa. Hence, two tables can be formed, each one of length $2^4 3^4$. The codeword will then alternately point at the two tables. The modulator outputs 16 bit samples to the DACs at 20khz, resulting in 4 samples per symbol. The total memory space occupied is 20,736 bytes as opposed to 3,125,000, a reduction factor of 93%. The overall process is illustrated in Figure 5.16. In this case the

codeword for the I channel is taken to be $\left[-\frac{\sqrt{2}}{2}, 0, \frac{\sqrt{2}}{2}, 0, \frac{\sqrt{2}}{2}, 0, -\frac{\sqrt{2}}{2}, 0\right]$, and will point at four consecutive memory locations where the samples that correspond to the drawn circles have been previously stored. For the next symbol, the codeword will be left shifted one position and four more samples will be output.

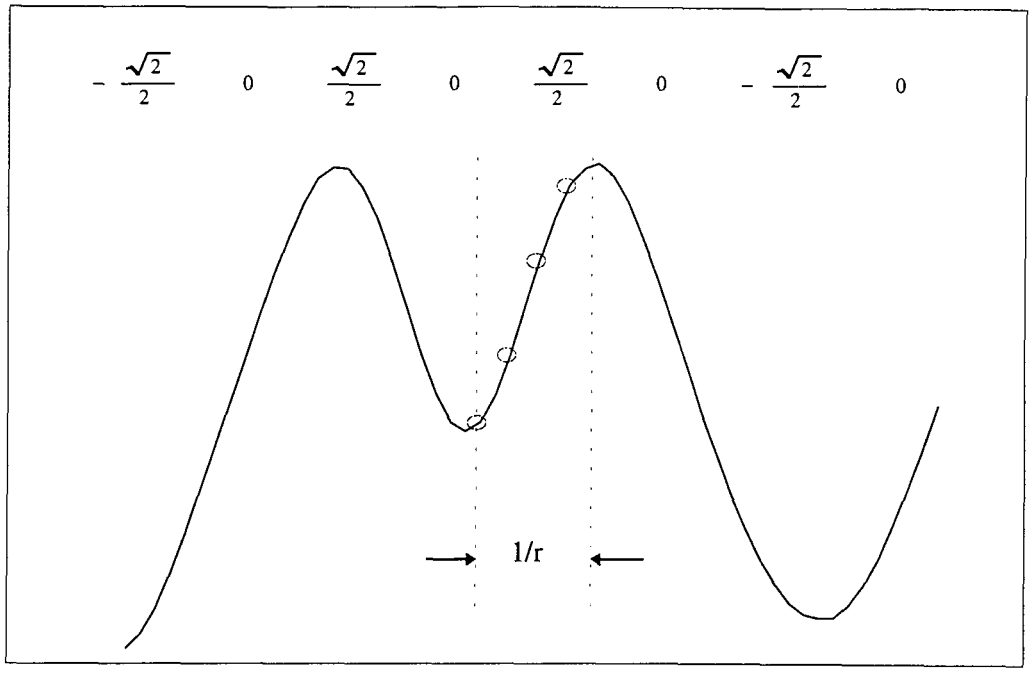

Figure 5.16 DSP Waveform Generation

In addition, the modulator was enhanced with some existing routines that provide a means of compensating for QUAD MOD imperfections at runtime.

5.3.2 Test Results

The vehicle started its motion, again, from location 1, the calibration site. Initially, 6 seconds of data, recorded while the vehicle was stationary, are analyzed. The first postprocessing stage implements the bank of seven equalizers obtained from the 8 tone test. Seven adjustable amplifiers follow, with a flat response over the frequency band. Their purpose is to compensate for amplitude mismatches between channels that could have been induced when readjusting the recording levels in the tape recorder. At this point, the seven signals were individually demodulated to get a base line of the receiver performance. The signals were passed through a matched filter, resampled and differentially decoded. A plot of the received constellation for one of the channels can be seen in Figure 5.17.

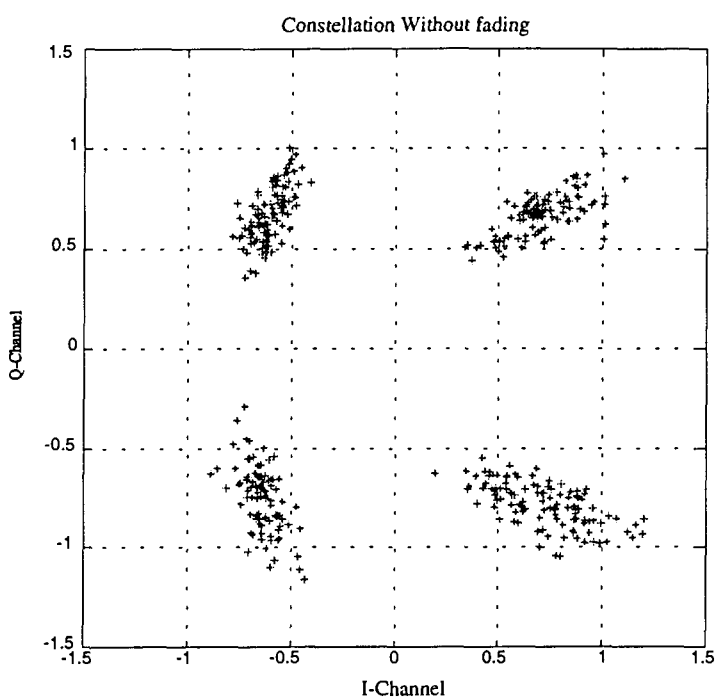

Figure 5.17 Decoded Constellation Without Fading

Although all 30,000 symbols were correctly demodulated, an unexpected and somewhat bizarre effect becomes evident. The cloud of data samples around the decision

points are oval-shaped and seem to follow a very deterministic pattern. After a great deal of unsuccessful attempts to compensate for this effect it was decided that, since the purpose of the test was to determine the performance of the antenna array system, this could be achieved by comparing it to the single antenna reception case. The presence of the forementioned slant is probably due to internal hardware and has nothing to do with the environmental parameters. Its possible causes sould be investigated with greater detail if the tests are to be repeated in the future. For now, rather than taking the results presented in this section as absolute, they should be seen as a proof of concept. The bit error rate figures will most likely be higher than they should be, but still more than representative for comparative purposes.

Next, the data recorded with the vehicle in motion were analyzed. Again, the seven channels were individually demodulated. Figure 5.18 shows the result for one of the channels. As in Figure 4.16, the scale is logarithmic.

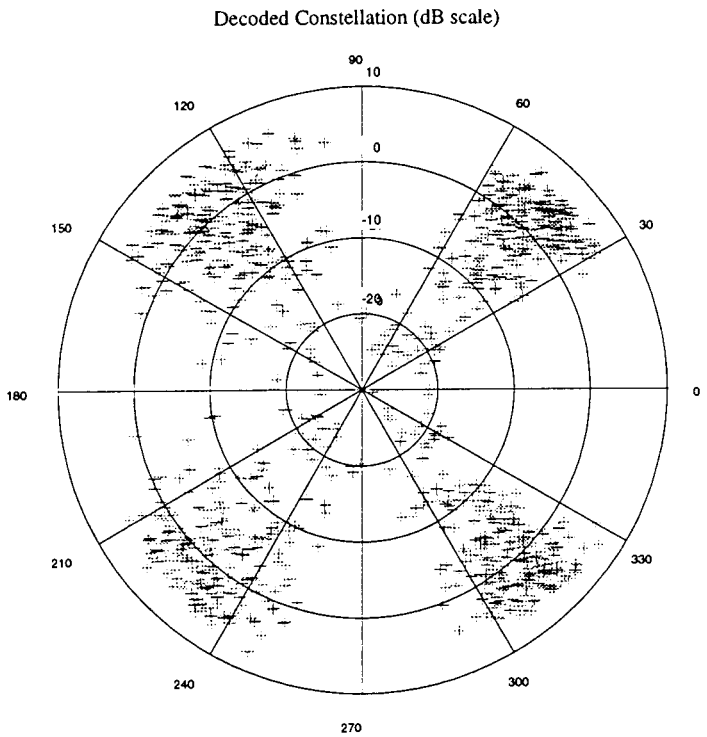

Figure 5.18 Decoded Constellation Without Diversity

The BER for this particular case, computed out of 65,514 samples was $4.197 \cdot 10^{-3}$. The BER turned out to be slightly different from one channel to another, but they all were in the range $4.197 \cdot 10^{-3}$ to $3.94 \cdot 10^{-3}$. The result is quite consistent with Figure 4.15, since it is estimated that the Eb/No on each receiver is around 23 dB.

Finally, the complete system described in Section 4.3 was tested. The value chosen for $\Delta\beta$ was of 14°. An additional decision was also made based on the output of the C-beam alone, as would have been done in a system that, using the same antenna array, did not provide angle diversity. The BER in the first case was found to be $3.65 \cdot 10^{-4}$. As for the second case, $9 \cdot 10^{-4}$ was the result, in full agreement with Figure 4.15. For an N element antenna array, the SNR can be written as:

$$SNR = \frac{P_{Signal}}{P_{Noise}} = \frac{N^2 P_{S1element}}{N P_{N1element}} = N \cdot SNR_{1element} \tag{5.4}$$

Hence, in this case the SNR of the combined signal is 8.45 dB higher than that of one single antenna element, that is around 31.5 dB. Table 2 summarizes the BER measurements performed so far.

Type of System	*BER*
1 receiver	$4 \cdot 10^{-3}$
7 element antenna array	$9 \cdot 10^{-4}$
7 element antenna array with diversity	$3.65 \cdot 10^{-4}$

Table 2 BER of the Different Systems

Figure 5.19 shows the constellation of the combined signal for the optimal diversity case. Not all 65,514 samples are displayed, only a small subset where the combining of the diversity signals works particularly well. It is unlikely that any errors were made on this particular subset of samples, although some of them can be seen to fall

dangerously close to the decision boundary. As a comparison, the same subset was plotted in Figure 5.18 for one of the antenna elements.

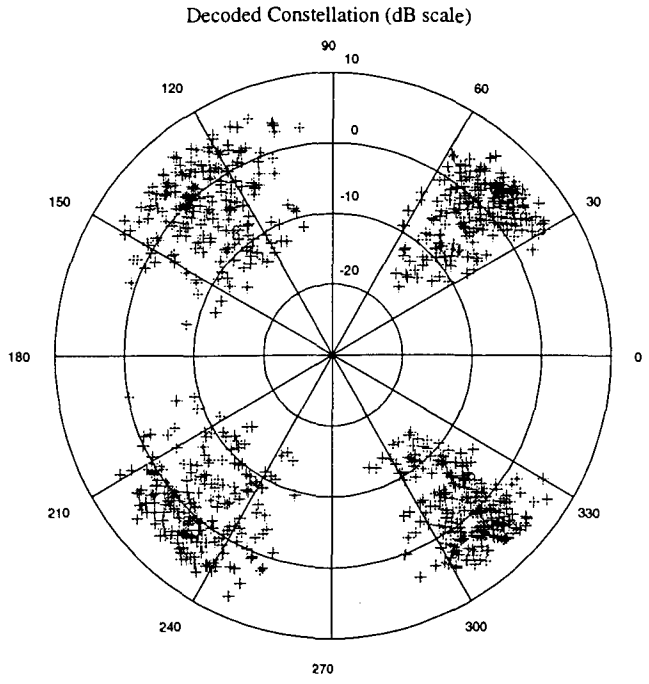

Figure 5.19 Decoded Constellation With Diversity

The test was then repeated for a wide range of values of the phase shift $\Delta\beta$ on the R-beam, to ensure that 14° gives, indeed, the maximum improvement. Figure 5.20 shows the evolution of the BER with the phase shift $\Delta\beta$. As it turns out, the maximum improvement of $3.2 \cdot 10^{-4}$ can be achieved with $\Delta\beta$=12° instead.

By comparing these numbers with the simulated curves of Figure 4.15 it becomes evident that the improvement was expected to be significantly higher. The BER for an Eb/No of 31.5 dB should have been close to 10^{-5}, more than one decade better. However, Figure 4.15 was obtained assuming a D/r ratio of 10. According to the estimate of Section 5.2, the D/r ratio should be close to 22. Once again a simulation was performed using the new value for D/r, and the resulting BER was compared to the previous ones. The newly

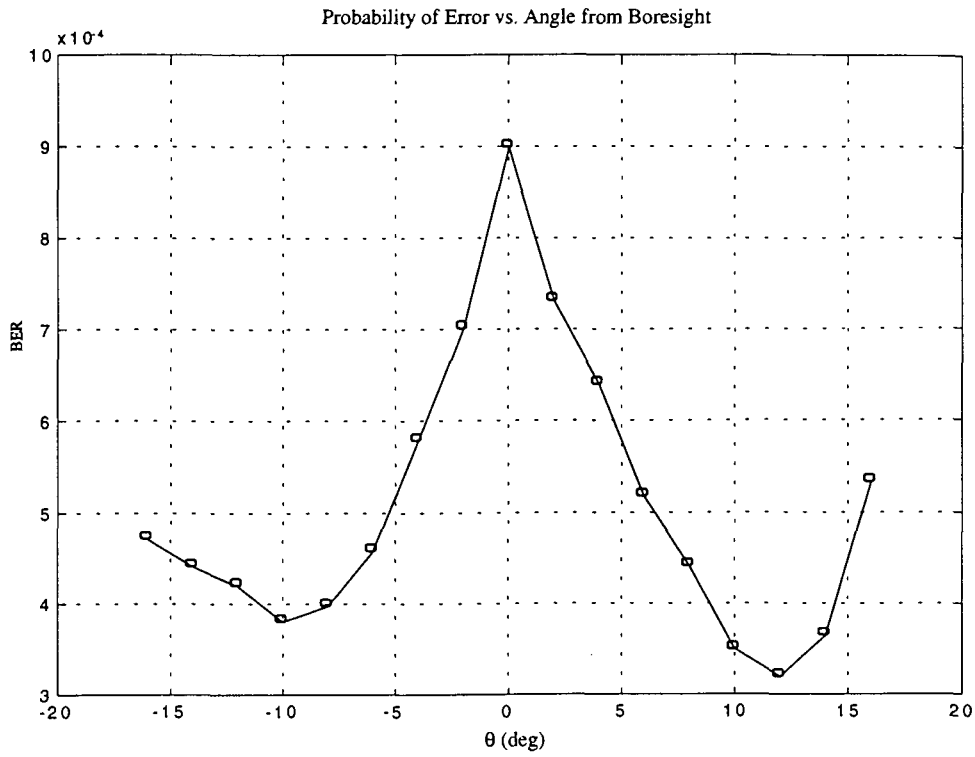

Figure 5.20 BER vs. Phase Shift, θ

obtained curve is plotted in Figure 5.21. As expected, the BER that corresponds to 31.5 dB is higher than in previous simulations, and even though it is not exactly $3.2 \cdot 10^{-4}$, it is fairly close, around $1.8 \cdot 10^{-4}$. In any case, the purpose of this section has been accomplished by proving that the improvement in the quality of the fading envelope through the use of the antenna array system translates into an effective decrease of the BER.

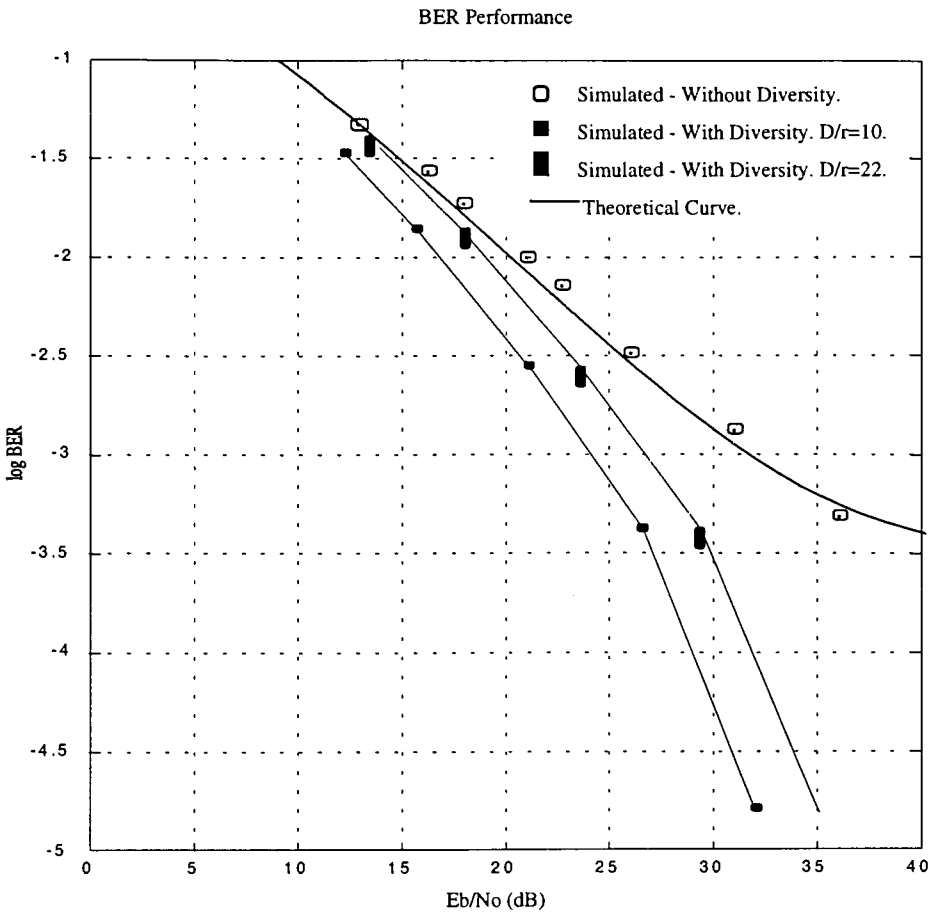

Figure 5.21 Simulated BER for D/r=22

6. CONCLUSIONS

A spatial channel simulator model was developed that recreates the multipath fading conditions that a base station phased array antenna encounters when receiving from a mobile unit. Analytical expressions were derived for the signal received by the individual array elements, as well as for the combined output. It was shown that, with the proper choice of parameters, the deviation from theoretical fading statistics was minimal. In addition, the signals across the array front were found to be very strongly correlated, as was the initial assumption, for reasonable values of the distance between mobile unit and base station. As a result, the antenna array was able to form and steer directional beams without appreciable distortion to its space factor.

The model was then used to investigate some of the potential features that the antenna array system can provide, namely mobile user tracking and angle diversity. A tracking algorithm was devised that retrieves the new position of the mobile at regular intervals with great accuracy. After numerous trials, the variance of the error incurred when retrieving the angular location was found to be $\pm 0.05°$, with the maximum error ever recorded being $+0.5°$.

Angle diversity was attained by generating one diversity beam, offset by a fixed angle from the main beam. A trade-off between relative received power and degree of decorrelation between signals received by the two beams resulted in an optimal value for the angle offset. It was found that a value anywhere between 13° and 15° was adequate for a wide variety of scenarios. The maximum achievable improvement was found to be dependent on the incoming wave beamwidth or D/r ratio, as defined in Section 4.1. As an example, for a beamwidth of 5.7° (D/r=10), the probability that the envelope drops 20 dB below its mean can be decreased from 0.5% to less than 0.02%. Angle diversity was then tested on a simulated $\frac{\pi}{4}-$QDPSK digital communications system. The results for what

was considered to be a typical set of parameters showed that the reduction of SNR necessary to achieve a BER of 1e-3 is close to 8 dB. In addition, the irreducible BER typical of DPSK was largely exceeded.

Finally, all the previous results were contrasted with those obtained from data recorded during field measurements. The tracking algorithm performed exceptionally well and, in general, so did the angle diversity modules. This fact was remarkably significant, because it also proved that the developed spatial channel simulator is a very valuable tool for system design and development. As far as the digital QDPSK test goes, the improvement in BER was not as spectacular as predicted. The data were strangely corrupted at some point during the recording process and the results had to be taken as a proof of concept, rather than definite.

In terms of further work, the spatial channel simulator model should be extended to include path loss, log-normal fading and, possibly, frequency selective fading. With the mere addition of path loss, co-channel interference could be simulated by introducing other mobile units transmitting in the same channel, each of them with its own ring of scatterers. Also, the effect of local scatterers near the base station must be studied, since in this case the correlation between adjacent elements can be severely degraded.

BIBLIOGRAPHY

[1] Shawn P. Stapleton and G.S. Quon, "*A Cellular Base Station Phased Array Antenna System*", 43rd IEEE Vehicular Technology Conference, pp. 1789-1792, Jun. 1993.

[2] W.C. Jakes, *Microwave Mobile Communications*, Wiley-Interscience, New York, 1974.

[3] W.Y.C. Lee, *Mobile Communications Engineering*, McGraw-Hill, New York, 1982.

[4] W.C.Y. Lee, "*Effects on Correlation Between Two Mobile Radio Base Station Antennas*". IEEE Transactions on Communications, COM-21, No. 11, pp. 1214-1224, Nov. 1973.

[5] W.L. Stutzman, G.A. Thiele, *Antenna Theory and Design*, Wiley-Interscience, New York, 1981.

[6] J. Proakis, *Digital Communications*, McGraw-Hill, New york, 1983.

[7] Fumiyuki Adachi, "*Postdetection Optimal Diversity Combiner for DPSK with Differential Detection*", IEEE Transactions on vehicular Technology, Vol. 42, No. 3, pp. 326-336, Aug. 1993.

[8] G. A. Arredondo, W. H. Chriss, E. H. Walker, "*A Multipath Fading Simulator for Mobile Radio*", IEEE Transactions on vehicular Technology, Vol. VT-22, No. 4, Nov. 1973.

[9] R. Ball, "*A Real Time Fading Simulator for Mobile Radio*", The Radio and Electronic Engineer, Vol. 52, No. 10, pp. 475-478, Oct. 1982.

[10] Faramaz Davarian, "*Hardware Simulator Assists Mobile Satellite Experiment*", IEEE 35th Vehicular Technology Conference, pp. 1-8, May 1985.

[11] S.P. Stapleton, Xavier Carbo and Trent O. Mckeen, "*Spatial Channel Simulator for Phased Arrays*", IEEE 44th Vehicular Technology Conference, pp. 1789-1792, Jun. 1994.